Schweizerische Eidgenossenschaft
Confédération suisse
Confederazione Svizzera
Confederaziun svizra

Federal Department of the Environment, Transport, Energy and Communications DETEC

Swiss Federal Office of Energy SFOE
Energy Research and Cleantech

Final report dated 20.12.2019

SwissTrolley plus

A battery-assisted trolley bus

Source: © Carrosserie HESS AG 2019

Date: 20.12.2019

Location: Bern

Subsidiser:
Swiss Federal Office of Energy SFOE
Energy Research and Cleantech Section
CH-3003 Bern
www.bfe.admin.ch

Subsidy recipients:
ETH Zurich
Institute for Dynamic Systems and Control (IDSC)
ML K 32.3
Sonneggstrasse 3
8092 Zürich
Schweiz
http://www.idsc.ethz.ch

Bern University of Applied Sciences
Department Engineering and Information Technology (BFH-TI)
BFH Energy Storage Research Centre
Aarbergstrasse 5
CH-2560 Nidau
www.bfh.ch/energy

Authors:
Mr. Andreas Ritter, ETH Zurich, anritter@idsc.mavt.ethz.ch
Mr. Fabio Widmer, ETH Zurich, fawidmer@idsc.mavt.ethz.ch
Prof. Christopher Onder, ETH Zurich, onder@idsc.mavt.ethz.ch
Dr. Alejandro Santis, Bern University of Applied Sciences, alejandro.santis@bfh.ch
Mr. Timan Schneider, Bern University of Applied Sciences, timan.schneider@bfh.ch
Mr. Ludovic Lauber, Bern University of Applied Sciences, ludovic.lauber@bfh.ch
Dr. Priscilla Caliandro, Bern University of Applied Sciences, priscilla.caliandro@bfh.ch
Prof. Andrea Vezzini, Bern University of Applied Sciences, andrea.vezzini@bfh.ch
and
Mr. Martin Widmer, Carrosserie HESS AG, martin.widmer@hess-ag.ch

SFOE project coordinators:
Men Wirz, men.wirz@bfe.admin.ch

SFOE contract number: SI/501321-01

Zusammenfassung

Dieser Bericht stellt die Ergebnisse der Forschungs- und Entwicklungsaktivitäten im Rahmen des Projekts "SwissTrolley plus" vor. Während das Hauptziel dieses Projekts darin besteht, die Technologie eines batteriegestützten Trolleybusses zu entwerfen und seinen Betrieb im öffentlichen Verkehrssystem Zürichs zu demonstrieren, befasst sich dieser Bericht mit der Entwicklung einer geeigneten Energiemanagementstrategie für den Hybridantrieb und einem Modell für die Batterielebensdauer, das die Alterung der Batterie quantitativ erfassen kann.

Der Einsatz von Batterien als Energiespeicher in Trolleybussen ermöglicht einerseits eine hohe Flexibilität bei der Nutzung der Fahrzeuge und andererseits eine deutlich bessere Energieeffizienz. In diesem Projekt wurde gezeigt, dass der Energieverbrauch im Vergleich zu herkömmlichen Trolleybussen ohne Traktionsbatterien um bis zu 15% auf ca. 2 kWh/km reduziert werden kann. Darüber hinaus basieren die entwickelten Regelstrategien auf der Theorie der optimalen Regelung und sind in der Lage, die sich wiederholenden Fahrmuster selbstständig zu erlernen und entsprechend zu nutzen. Dieser Ansatz ermöglicht es, Streckentrenner der Oberleitung zu erkennen und vorherzusagen und so Lichtbogenblitze zu vermeiden. Schliesslich zeigen „Software-in-the-Loop“-Simulationen, dass die Verwendung einer solchen vorausschauenden Regelstrategie es ermöglicht, sowohl die Batteriekapazität als auch die Anteil an Strecken mit Oberleitungen zu halbieren, ohne zusätzliche Energieeffizienzen im Vergleich zur bestmöglichen Strategie zu in Kauf nehmen zu müssen.

Um die Belastung der Batterie zu charakterisieren, beschreibt der Bericht die experimentell gemessene Abhängigkeit des Zustands der Batterie von verschiedenen Betriebsbedingungen. Insbesondere wurde bei den durchgeführten Experimenten beobachtet, dass C-Raten im Allgemeinen einen höheren Einfluss auf die Alterung haben als die Betriebstemperatur. Darüber hat das Zyklieren der Zellen mit geringer Entladetiefe und bei Spannungswerten weit weg der Grenzen nahezu keinen Einfluss. Diese Daten dienen der Erstellung eines Modells für den Gesundheitszustand der Batterie, das in der Lage ist, die Lebensdauer der Antriebsbatterie zu schätzen und dem Energiemanagement einen Hinweis auf den Bereich zu geben, in welchem die Batterie betrieben werden sollte um ihre Lebensdauer zu verlängern.

Résumé

Ce rapport présente les résultats des travaux de recherche et développement du projet «SwissTrolley plus». L'objectif global de ce projet est de concevoir la technologie d'un trolleybus assisté par batterie et de démontrer son fonctionnement dans le système de transport public de Zurich. Ce rapport traite du développement d'une stratégie de gestion de l'énergie appropriée pour le système de propulsion hybride et d'un modèle de durée de vie du système de batterie qui permet d’évaluer le vieillissement de la batterie.

L'utilisation de batteries comme accumulateurs d'énergie dans les trolleybus permet une grande flexibilité dans l'utilisation des véhicules d'une part et une efficacité énergétique nettement supérieure d'autre part. Dans ce projet, il a été démontré que la consommation d'énergie peut être réduite jusqu'à 15% à environ 2 kWh/km par rapport aux trolleybus conventionnels sans batteries de traction. De plus, les stratégies de contrôle développées sont basées sur la théorie du contrôle optimal et sont capables d'apprendre ainsi que d'exploiter les modèles de conduite répétitive de manière autonome. Cette approche permet de détecter et de prédire les commutateurs de fils aériens et d'éviter ainsi les arcs électriques. Enfin, les simulations « software-in-the-loop (SIL) » montrent que l'utilisation d'une telle stratégie de contrôle prédictif permet de réduire de moitié à la fois la capacité de la batterie et la couverture des lignes aériennes sans scarifier les économies d'énergie supplémentaires par rapport à la meilleure stratégie possible.

Afin de caractériser les contraintes exercées sur la batterie, le rapport illustre la dépendance expérimentalement mesurée de l'état de santé de la batterie (State of health, SOH) par rapport à diverses conditions de fonctionnement. En particulier, il a été observé au cours des expériences menées que les taux de charge et de décharge « C-rates » ont en général un impact plus élevé sur la dégradation que la température de fonctionnement. De plus, un cycle de charge-décharge des cellules avec de faibles valeurs de profondeur de décharge et à des niveaux de tension éloignés des limites n'entraîne pratiquement aucune dégradation. Ces données servent à créer un modèle de l'état de santé capable d'estimer la durée de vie de la batterie du trolleybus et de donner une indication à la gestion de l'énergie sur la plage dans laquelle la batterie doit être utilisée pour prolonger sa durée de vie.

Summary

This report presents the results of the research and development activities within the project «SwissTrolley plus». While the overall goal of this project is to design the technology of a battery-assisted trolley bus and demonstrate its operation in Zurich’s public transportation system, this report addresses the development of a suitable energy management strategy for the hybrid propulsion system and a battery system lifetime model which allows to quantity the aging of the battery.

Using batteries as energy storage devices in trolley buses enable great flexibility in the use of the vehicles on the one hand and a significantly better energy efficiency on the other. In this project it was shown that the energy consumption can be reduced by up to 15% to approx. 2 kWh/km compared to conventional trolley buses without traction batteries. Moreover, the developed control strategies are based on optimal control theory and are able learn and exploit the repetitive driving patterns autonomously. This approach allows to detect and predict wire switches of the overhead wires and thereby prevent arc flashes. Finally, software-in-the-loop simulations show that using such a predictive control strategy allows to halve both the battery capacity and the coverage of overhead lines without scarifying additional energy efficiencies compared to the best possible strategy.

In order to characterize the stress on the battery, the report illustrates the experimentally measured dependency of the battery state of health on various operating conditions. In particular, it has been observed during the conducted experiments that C-rates have in general a higher impact on the degradation than the operating temperature. Additionally, cycling the cells with low depth of discharge values and at voltage levels away from the limits results in almost no degradation. This data serves to create a state of health model which is able to estimate the lifetime of the trolley bus battery and giving indication to the energy management on the range in which the battery should be operated to extend its lifetime.

Main findings

- The developed software framework allows to run several energy management strategies in parallel which learn and exploit the repetitive driving patterns autonomously.
- The predictive control strategy can prevent arc flashes and allows to halve both the battery capacity and the coverage of overhead lines without causing additional energy efficiencies compared to the best possible strategy.
- To optimize a battery system for a real use, experimental mapping of the performances at different operating conditions is necessary, especially when the system is subjected to different ambient temperatures and high C-rate are expected as the mobility applications.
- The higher investment costs of the LTO/NMC battery cells compared to G-NMC cells (as well as slightly lower energy density of these cell) is economic valuable if durability at almost constant performances is expected.

Contents

Abbreviations

BEV	Battery electric vehicle
ECMS	Equivalent consumption minimization strategy
EMS	Energy management system
HVAC	Heating, cooling and air-conditioning
LTO	Lithium titanate oxide
MPC	Model predictive control
NMC	Lithium nickel manganese cobalt oxide
SLRM	Self-learning road map
SOC	State of charge
SOE	State of energy
SOH	State of health
VCU	Vehicle control unit

1 Introduction

1.1 Background information and current situation

In the framework of the SwissTrolley plus project, Carrosserie HESS AG and other project partners are developing an innovative trolleybus. Industrial partners are the Zurich Transport Authority, academic partners are the ETH Zurich and the BFH. The novelty of this trolleybus is its drive system, consisting of a traction battery and an electric motor, which replace the diesel auxiliary unit and the fuel tank of conventional trolleybuses. In addition, the heating and cooling systems for the passenger compartment have been completely redeveloped. Among other things, infrared radiant heaters, heat pumps and the latest generation of electric heating systems are used. The combination of these devices allows great energy savings, since the efficiencies are higher than those of the devices used in conventional trolleybuses. The high-performance traction battery, consisting of lithium cells with lithium titanate anode and nickel-manganese-cobalt cathode (LTO/NMC cells), offers an extended lifetime.

1.2 Purpose of the project

Within the project «SwissTrolley plus», Carrosserie HESS AG is developing a new type of trolley bus together with the industrial partner Verkehrsbetriebe Zürich (VBZ) and the research partners ETH Zurich and Bern University of Applied Sciences (BFH). The novelty of this trolley bus is its propulsion system which includes a traction battery that replaces the auxiliary power unit of the conventional trolley bus. As a result, the whole DC circuit of the vehicle is on battery voltage, with a DC-DC converter offering galvanic separation from the overhead wire voltage. With respect to regulations considering insulation requirements and other safety measures, the «SwissTrolley plus» prototype vehicle can thus be considered a battery electric vehicle (BEV) with recharging capabilities from the overhead wire network. This in turn offers advantages over the line voltage-based vehicles such as trains, trams, and standard trolley buses with respect to cost and energy efficiency of the traction components. The propulsion system is compliant with two different norms: The trolley bus norm EN50502 and the electrical vehicle norm ECE R100.

The high-power traction battery offers several other advantages: (a) The battery can store the braking energy gained by recuperation and thus reduce the total energy consumption of the vehicle. (b) The battery-assisted trolley bus is able to drive on routes without any catenary lines, which drastically reduces infrastructure installation and maintenance costs. (c) By using the battery as an electric buffer, the energy management system of the vehicle will be able to reduce peak loads on the electric grid, which is desirable by the electricity supplier of the trolley bus network.

1.3 Objectives

The goal of the project is to develop the EMS algorithms and a SOH model, necessary to the operation of the battery-assisted trolley bus.

In particular, control algorithms for managing the electric energy that is available to the battery-assisted trolley bus such that the bus can be operated reliably and energy efficiently. The derived approach must ensure maneuverability at all times. This requirement is particularly crucial in sections of the bus route where no catenary lines are available, i.e., the propulsion system is exclusively running on battery power. The energy management system has therefore to guarantee a sufficient state of charge of the battery before the bus enters the wire-free section.

Similar to conventional hybrid-electric vehicles, the battery-assisted propulsion system allows to reduce the total energy demand of the trolley bus by managing the state of charge of the battery appropriately.

Initial simulations published in [1] show that the battery can help to reduce the electric energy demand by up to 15% due to regenerative braking. However, too high charge and discharge currents harm the battery considerably and thus shorten its lifespan. Therefore, the energy management strategy should be able to reduce high power peaks in order to ensure a sufficient battery lifespan. To achieve this result, BFH-TI oversaw experimentally characterized the battery in a wide range of operating conditions. The developed tools guarantee a desired minimum battery lifespan and define the most suitable operation regions of the battery to maximize the battery life.

The first tool to be developed is composed of experimentally estimated factors that affect the battery lifespan. Such factors, so-called severity factors, will be implemented into the energy management strategies developed by ETH Zurich, able to find an optimal trade-off between maximizing the battery lifetime and minimizing the energy consumption. These severity factors provide information about the negative effects of operating conditions on the battery lifespan. As a result, the energy management can make decisions on how to use the battery power conservatively while achieving an overall energy efficient operation at the same time.

The second tool is an off-line battery life model for the specific battery cell of the «SwissTrolley plus» bus. At present, the battery cell under consideration is NMC/LTO. The life model can be parametrized to define the aging or the state of health (SOH) of the battery cell. This model can support the design phase of new trolley buses with respect to the battery sizing. In addition, a desired minimum battery lifespan shall be guaranteed for the trolley buses operating on different routes or in different cities. Later, this model may be adopted to other cell technologies using reconfigurable parameters.

Today, the lifespan of trolley buses exceeds the lifespan of batteries by a factor greater than two. Therefore, the outcome of BFH-TI's experimental and numerical work will serve to help enhance the economic feasibility of battery-assisted trolley buses.

2 Energy management system

The goal of every energy management system (EMS) of a road vehicle with a hybrid propulsion system is to distribute the demanded power request among the available power sources and energy storage systems. In the case of the «SwissTrolley plus» prototype two components are available, i.e., the overhead wires as power source and the LTO battery as energy storage. As a result, the power request can either be fulfilled by drawing current from the overhead wires via the DC-DC converter and the collectors, by drawing current from the equipped battery, or by using a combination of the power supplies of both devices. Moreover, the system obviously also allows to draw more current from the grid than required in order to charge the battery. The hybrid propulsion system thus offers a so-called degree of freedom for which the EMS provides a usage strategy. This strategy might be based on a fixed set of specified rules, or derived from mathematical descriptions of the problem with a specific target criteria in mind. Even though the former approach can lead to suitable solutions, only the latter approach allows to formulate a strategy which explicitly achieves a defined optimization criterion. Therefore, the development of our EMS strategy is based on an optimization problem that aims for the lowest possible overall energy consumption from the feed points of the electric grid.

To achieve this goal, the EMS decides in each instance in time how the given power request should be distributed ideally. The challenge of this task is mainly that the individual decisions can obviously only take into account the information that is available up to the respective point in time. However, the collective sum of these individual decisions should still meet the overall objective. Therefore, we typically have to include feedback control loops in order to obtain a robust strategy. Furthermore, such strategies may also use predictive information that allows to estimate the future power request and thereby provide strategies with better performance. Within the project «SwissTrolley plus» several strategies based on the formulation of an optimization problem have been exploited. This report presents two of them and an additional interfering controller that handles breaks of the overhead lines. All three strategies are successfully implemented and extensively tested. The first strategy includes only very little information about the system and is thus rather simple. The second strategy is more complex and considers predictive data. In practice, the software runs both strategies in parallel such that the simpler strategy can serve as a fallback strategy if the more complex strategy fails. The interfering controller learns the locations of the line breaks and overrides the output of the other strategies in these regions.

2.1 Procedures and methodology

The specific task of the energy management system (EMS) of the «SwissTrolley plus» is to provide suggestions on how much power the DC-DC converter should draw from the grid at each point in time. These suggestions are calculated on a separate EMS computer and transmitted to the vehicle control unit (VCU), which in turn forwards them to the respective hardware components of the propulsion

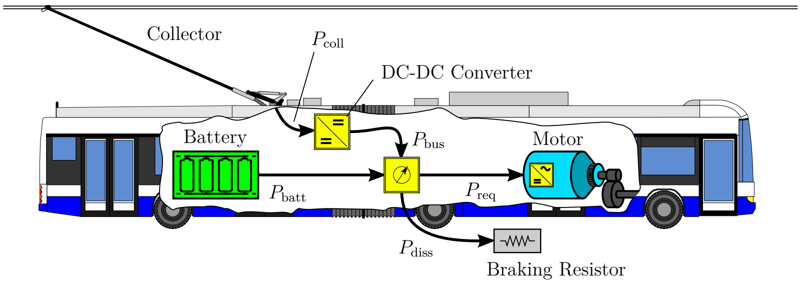

Figure 1: Schematic illustration of the propulsion system of the «SwissTrolley plus» prototype.

system. A schematic representation of the propulsion system of the «SwissTrolley plus» prototype is shown in Figure 1, where the battery power is indicated with P_{batt}. The electric power coming from the overhead wires is indicated with P_{coll}.

The power request of the vehicle is indicated with P_{req}. This quantity sums up the demand of the electric motors in order to fulfill the driver's speed request and the power demand of all auxiliary devices such as hydraulic pumps, lights, heating, cooling and air-conditioning systems (HVAC), etc.

Out of the auxiliary devices the HVAC systems typically are by far the largest energy consumers. Moreover, the HVAC systems of trolley buses consume about the same amount of energy than the traction system, as illustrated in Figure 2. Accordingly, the HVAC systems should be considered in the derivation of an energy management strategy. Which in turn means that the involved components must have appropriate interfaces so that they can be controlled and validated thermodynamic models of these components and the vehicle chassis are necessary. For reasons of time, we have therefore initially focused on the traction system only. However, the goal has always been to pursue generic control strategies that can later be extended to thermodynamic considerations.

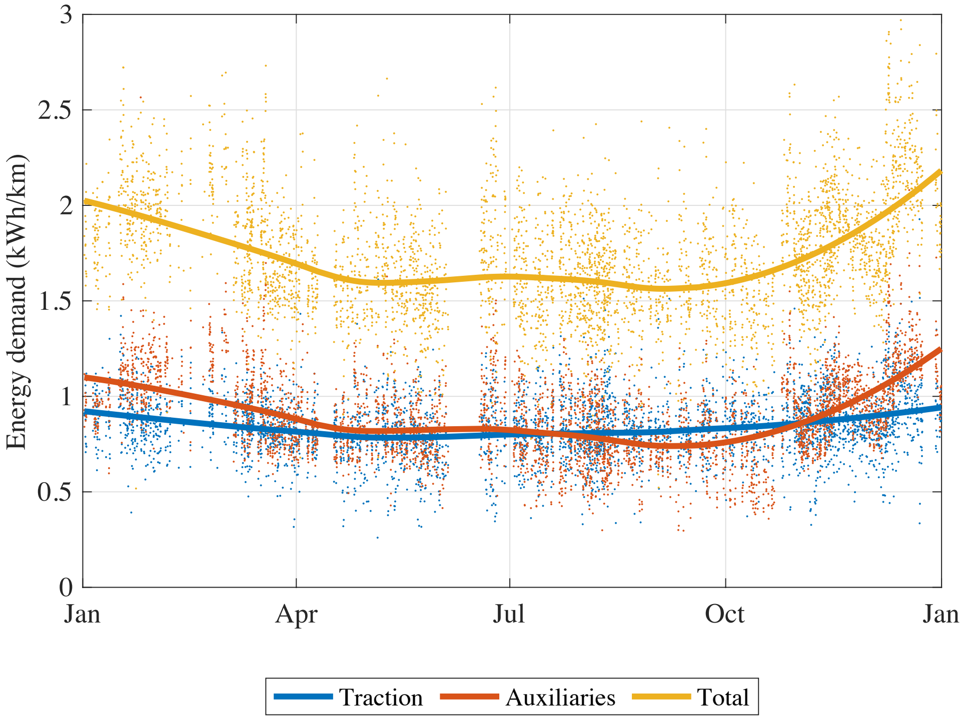

Figure 2: Energy demand over one year. The represented data was recorded in 2018 and 2019. The temperature profile in these two years was very similar. It varied in average between 5°C and 25°C, where the lowest average value was in January and the highest value was in July. In between the average temperature increased and decreased almost linearly, see Figure 74.

As there is no relevant energy storage in the electric components except of the battery, the following power balance must always hold,

$$P_{batt} + P_{bus} = P_{req} + P_{diss}.$$

The variable P_{diss} indicates the dissipated power, which is converted to heat in the braking resistor. Of course, this energy waste is never desired and is thus only needed in case of a an unsuccessful energy management strategy.

The EMS of the «SwissTrolley plus» consists of several elements briefly depicted in the following. Successive sections 2.1.1 to 2.1.4 address these elements in more detail.

- First, a basic EMS is derived that ensures that the power balance mentioned above is exploited optimally by distributing the power request between the battery and the grid. This EMS gets along without any predictive information. The corresponding theory is known since 1956 and was formulated by the Russian mathematician Lev Pontryagin [2]. It was adapted to the EMS for the configuration of the «SwissTrolley plus» prototype in [3].
- In order to further exploit the driving mission of the vehicle, predictive data is required, e.g., an estimate of the upcoming velocity and altitude profile. For doing so, we first improve the quality of the raw GPS data by applying an extended Kalman Filter (EKF). The results of this pose estimator are then used to build a mathematical model of the road network. This construct is referred to as the self-learning road map (SLRM). It was first proposed in [4] and then improved in [5]. The final implementation is described in [6], which is yet to be published.
- Based on the predictive information we propose a method to avoid arc flashes at wire switches. This line break controller uses the prediction provided by the road map to anticipate upcoming wire switches or grid sector changes in the overhead wires, and influences the EMS suggestions when necessary. This controller as well as the previously mentioned elements are running on the «SwissTrolley plus» prototype since the spring of 2019.
- Finally, in a simulation study an EMS version based on model predictive control (MPC) has been derived. The corresponding results indicate that large grid-free sections of up to 50% of the total distance and batteries of almost only half of the current size are realizable without loss of energy efficiency. The corresponding theory and the results are covered in [7].

2.1.1 Adaptive equivalent consumption minimization strategy

As mentioned before, the task of the EMS is to distribute the power request among the battery and the overhead wires in each point in time while trying to minimize the overall energy consumption. It can be shown analytically that—under some weak assumptions—this problem can be split into a local and a global optimization problem. In the local optimization problem the instantaneous distribution of the power request is found. If we assume a sample frequency of 1Hz for instance, the EMS determines in each second how to use the battery and the DC-DC converter to fulfill the power request that is demanded in this second by consuming as little energy as possible. This calculation includes the power losses occurring in all components involved based on their operating points. The goal is thus to find the operating points that achieve the demanded power request with the lowest power losses. In order to account for the two power sources—the grid and the battery—the energy supplies of these sources is balanced using an "equivalence factor" s. This factor quantifies the value of 1 kWh of battery energy against 1 kWh of grid energy.

The derivation of this strategy goes back to the control theory of Pontryagin's maximum principle. Following the Hamiltonian of classical mechanics, it is proven that the necessary condition of the solution of an optimal control problem complies with the Minimization of the Hamiltonian function. Deriving the Hamiltonian for the minimization of the consumed grid energy (i.e., the energy fed into the grid by the feed point), we arrive at the basic equation for “equivalent consumption minimization strategy” (ECMS). In this case, minimizing the Hamiltonian and thus the consumed grid power corresponds to minimizing the “equivalent energy consumption”.

If the influence of the state of charge (SOC) on the battery parameters such as the internal resistance and the open-circuit voltage is neglected, the remaining global optimization problem mentioned above is reduced to finding the optimal constant value of the equivalence factor s (adjoint state).
However, the optimal value of the equivalence factor can only be determined, if the whole trip is known perfectly ahead of time. As this is not the case a different approach must be taken to determine the value of the equivalence factor. The proposed adaptive ECMS dynamically adjusts the equivalence factor based on the current SOC of the battery. If the SOC decreases, the value of the battery energy increases, and vice-versa. Accordingly, we use the current SOC value to adjust the equivalence factor s. This feedback loop is typically implemented using a standard PI controller. The entire process of calculating the optimal distribution of the power request and the adjustment of the equivalence factor runs in the bus at a rate of 10 Hz.

2.1.2 Pose estimator and self-learning road map

The pose estimator estimates the current position, orientation and velocity of the bus by combining the location estimates of the GNSS device and the odometry measurements provided via the RS-232 interface. Combining these two sources of measurements allows to obtain smoother trajectories of pose estimates at a much higher precision.

The pose estimator uses an extended Kalman filter (EKF) which starts with an initial guess of the state and then recursively performs a state update step via a process model and a measurement update step via a measurement correction. More details on Kalman filtering and optimal state estimation in general is provided in the excellent reference [8]. Application-oriented approaches similar to the one we use are given for instance in [9]–[13]. The process model equations and the measurement correction equations of the EKF as well as the specific definition of the state, input, and measurement variables are given in [6]. The equations are inspired by the student projects [14] and [15].

The self-learning road map is responsible for learning the environment of the vehicle. By continuously recording the pose estimates and inserting them into a directed graph, the algorithm is able to represent the roads of the transport network. Based on this description and the current location of the vehicle, the module predicts the upcoming driving conditions by traversing the graph and concatenating the respective data.

The following three main processes are involved, i.e.,

1. resampling of the stream of pose estimates to a equidistant representation,
2. constructing the directed graph to represent the road network, and
3. obtaining predictions based on that graph.

The resampling process is responsible for converting the pose estimates that arrives typically every second into the distance domain where the estimates should be sampled equidistantly. The map construction process takes the pose estimates and creates the directed graph that represents the road network. The prediction process travels along this directed graph starting at the current node and obtains data of the upcoming driving conditions as a function of distance.

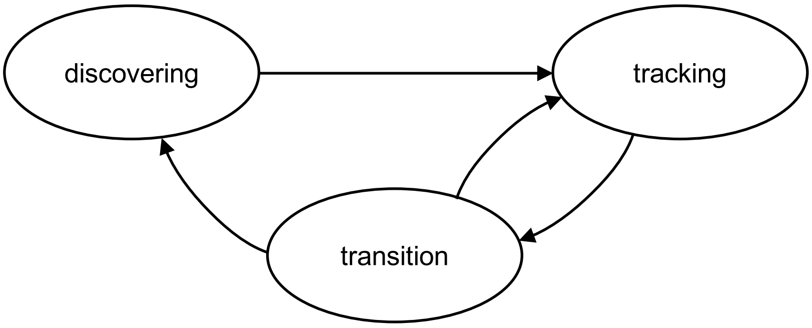

Figure 3: The three modes of the road map constructor.

For constructing the directed graph, several routines are required which are detailed in [6]. In essence, the algorithm consists of the following three modes, which are illustrated in Figure 3.

- The *discovering* mode is used whenever the vehicle is assumed to drive on a road that has not been mapped before.
- The *tracking* mode, on the other hand, is used whenever the vehicle is driving along a road that is already represented by the directed graph.
- The *transition* mode introduces an intermediate step when going from tracking mode to discovering mode. This approach is used to cope with pose estimates that are not sufficiently close enough to a known road but also not sufficiently far away from any known road. As long as this discrepancy is not clearly solvable, the construction procedure buffers the pose estimates temporarily and postpones the decision for whether going to discovering mode or tracking mode again.

The algorithm in this module bases on the student projects [4] and [5] and is described in detail in [6].

2.1.3 Line break controller

The trolley bus overhead wires are supplied by DC power at approximately 700 V. In contrast to trams and trains, trolley buses are isolated against the ground and therefore need two wires in order to be exposed to an electric potential difference. As a result, crossings and junctions of trolley bus routes involve wire switches that guide the trolley shoes in the desired directions. These switches are isolated and thus cause sudden drops in the measured voltage when passing them. Consequently, moving through such an isolated section while demanding electric power from the overhead wires can cause arc flashes, which harm the wire switches and the trolley shoes.

The goal of controlling the line breaks is to avoid the undesired arc flashes by automatically reducing the power input from the grid during the isolated sections. Given that the trolley bus is supplemented with an electric battery, we can interrupt the power input completely and switch to battery mode.

2.1.4 Model predictive control

As the name suggest, the strategy involves predictive information and uses a model to derive the control inputs. More specifically, this strategy uses an estimate of the upcoming velocity and altitude profiles to calculate the expected power request. Based on these values an optimal strategy for the entire prediction horizon is determined. For both the calculation of the expected power demand and the optimal EMS strategy a model of the vehicle is required, thus the name model predictive control (MPC). Furthermore, in MPC the optimal control problem is typically solved recursively and only the first part of the obtained solution is applied. This approach ensures stability and allows to deal with imperfect predictions. Besides the inclusion of predictive information, the main advantage of such a control strategy is that it can include non-linear behavior and discrete variables, which are typically hard to tackle with conventional control algorithms that are derived from the classic control theory.

The goal of having a controller based on MPC is to provide a systematic approach that allows to incorporate various optimization criteria and operation limits simultaneously while still offering an optimal solution. Once this framework is established, additional constraints and certain preferences for specific operation points are easy to integrate. Furthermore, compared to the adaptive ECMS, grid-free sectors and altitude profiles are explicitly respected, which leads to improvements in energy efficiency.

The required predictive information is provided by the self-learning road map which contains data recordings from previous runs on the same road and thus allows to infer repetitive driving patterns. Under the assumption that the current trip is similar to the previous trips, MPC uses a model of the vehicle and the provided upcoming driving scenario to derive the best possible control strategy. This strategy is then applied until a new prediction is available and the corresponding optimal strategy can be derived.

In the proposed implementation, the optimal control problem is formulated as a non-linear program (NLP). The result of the optimization is the optimal power split between the power drawn from the grid and the power drawn from the battery. In addition, the resulting optimal SOC trajectory is available.

Using this optimal SOC trajectory we can solve a simpler optimization problem similar to the one applied in section 2.1.1. Based on the optimal control theory we can find an optimal constant equivalence factor in order to follow the optimal state-of-charge trajectory. This equivalence factor is then used to calculate the instantaneous optimal power split that is transmitted to the VCU.

The motivation for the described cascaded control is that the first part which involves the complete optimization problem is typically much more costly and time-consuming to solve. Consequently, providing instantaneous suggestions to the VCU would be impossible. On the other hand, this fast adaption is only necessary due to the deviations of the real future and the predicted future. If the prediction was perfect, the optimal control strategy obtained in the first part could be applied without compunction.

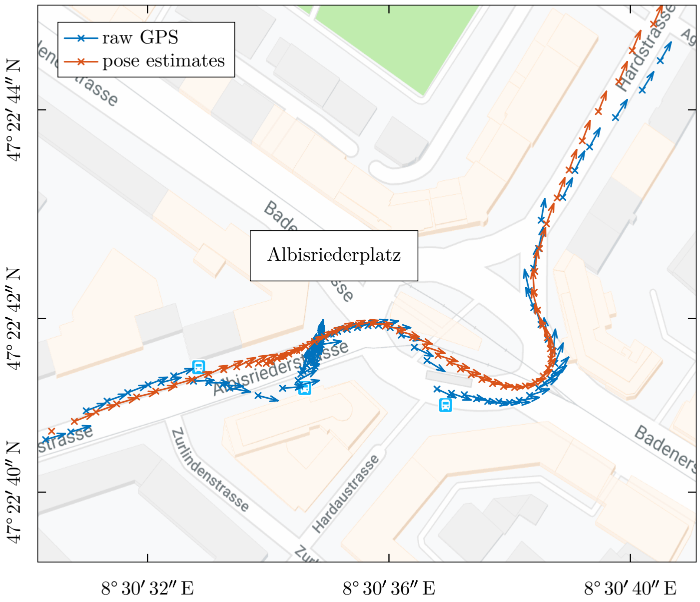

Figure 4: Measured GPS data in blue and result of the pose estimation filter in red. The raw data was recorded on 18.03.2019 between 21:16 and 22:03. The depicted results are obtained with the software version v1.12.1.

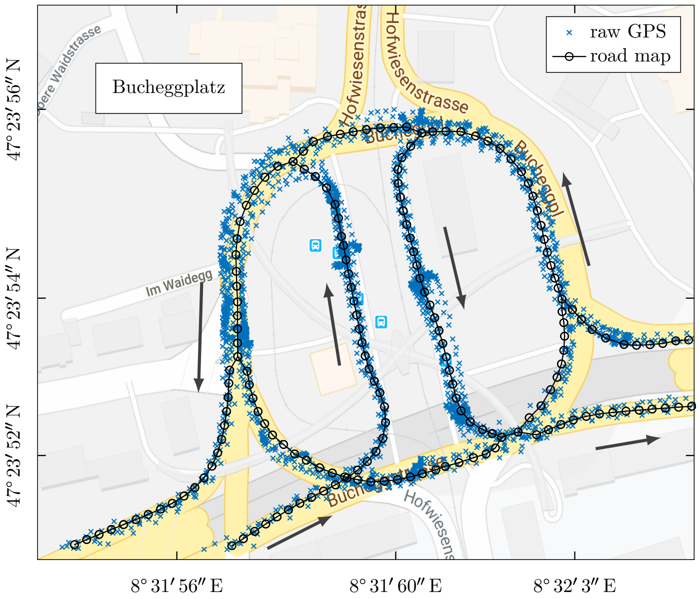

Figure 5: Visualization of the road map as directed graph in black. The directions of the edges are omitted in this representation for clarity. Instead, the dark gray arrows indicate the general direction of travel that is respected in the edge directions. The raw GPS data is shown in blue. The data used to create this road map was recorded on 03.12.2018 between 06:29 and 15:54, and thus represents nine runs.

2.2 Results and discussion

This section covers the results obtained until mid of May, 2019. First, the achieved performance of the pose estimator and the road map constructor are illustrated in two examples. Then, the implemented EMS algorithms, the adaptive ECMS and the line break controller are discussed based on data recordings of the online system from 24.05.2019 between 11:50 and 12:50. Ensuing, we present an analysis of the field campaign conducted by Carrosserie HESS AG and Verkerhsbetriebe Zürich (VBZ) between 17.03.2019 and 25.03.2019. This section primarily addresses the backup EMS of HESS and the adaptive ECMS. The comparison to the standard trolley bus is only shortly elaborated. A more detail study is presented in the annual/final P&D&L report of HESS and VBZ. Finally, the findings of the MPC strategy for the predictive EMS are presented.

2.2.1 Pose estimator and self-learning road map

Figure 4 shows a typical run on Zurich's trolley bus route 33 around Albisriederplatz. The pose estimation filter is clearly able to improve the noisy GPS signal especially at bus stops and around sharp curves, where the wheel speed recordings allow to obtain a more precise description of the vehicle's motion.

One of the most complicated crossings in Zurich is probably around Bucheggplatz. Here, multiple roads connect in a large roundabout of three lanes. Various tram routes cross the roundabout through the center. An additional one has its end loop on part of the roundabout. Finally, five different bus routes cross at Bucheggplatz where all bus stops are in the center of the roundabout. Therefore, data recorded around Bucheggplatz has proven to be very useful to validate the proper working of the road map algorithm. The corresponding result of the road map construction is shown in Figure 5.

The data contained in the road map nodes is for example illustrated in Figure 6. Each colored data point is associated to one specific node of the road map. The respective values are color-coded. All results, including the map excerpt of Figure 5 are obtained with the software version v1.12.1.

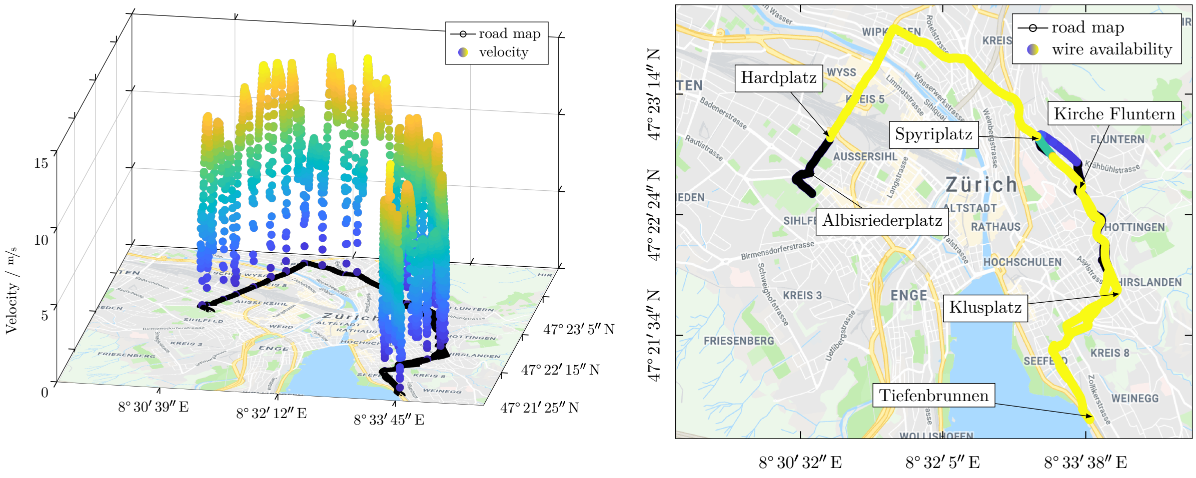

Figure 6: Data stored in the road map. The velocity data points shown on the left are averaged values over several runs on the same route. The top speed is typically between 10 m/s and 15 m/s. The probability of wire availability is shown on the right. Between bus stops Hardplatz and Spyriplatz, and Klusplatz and Bahnhof Tiefenbrunnen the data clearly indicates that wire is available. On the remaining parts of the driven route, either no wire is available (around Albisriederplatz) or the signal is not so clear (around Fluntern). The latter situation may occur when the bus driver does not always connect to the grid. Moreover, the direction of travel may also be relevant for the wire availability, which yields to values around zero and around one at similar geographical locations. Such situations are hard to see in this illustration.

2.2.2 Adaptive ECMS and line break controller

The adaptive ECMS has been running on the vehicle since very early versions of the software. However, the results shown here are all obtained with the software version v1.12.1.

The analyzed scenario covers 60 minutes of a run on bus route 33 in Zurich on 24.05.2019 between 11:50 and 12:50. The recorded GPS trajectory within this period is shown in Figure 7. Figure 8 shows the corresponding recorded velocity and altitude measurements of the GPS sensor. The operation of the energy management is summarized in Figure 9. In the top graph the battery discharging power is depicted. The measurement data mostly aligns very precisely with the suggestions of the EMS. Only in sections, where the bit 0x08 of the EMS status is active— shown in the fourth graph—the signals diverge slightly. In these sections, most notably from around 12:10 to around 12:25, the upper SOC limit of the EMS handler of 85% is violated, i.e., P_{bus} is not allowed to be above its optimal value $P^{\star}_{\text{bus}}$, which is the limited value. See Figure 1 and Figure 10 for the meaning of P_{bus} and the SOC and SOE trajectories, respectively.

Figure 7: Recorded GPS trajectory on 24.05.2019 between 11:50 and 12:50. The recorded run starts around Kirche Fluntern and ends in the region of Klusplatz, as indicated with the asterisk and square symbols, respectively.

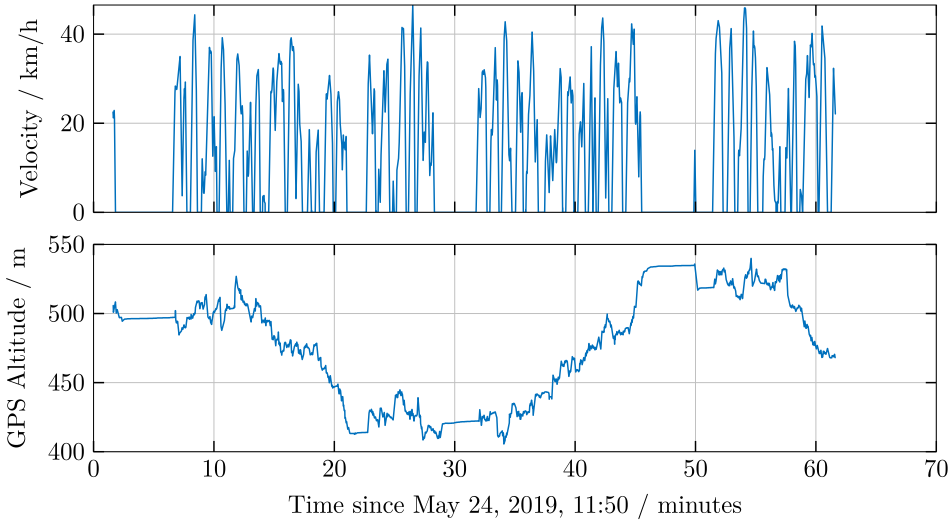

Figure 8: Velocity derived from the shaft speed and altitude measurements of the GPS sensor.

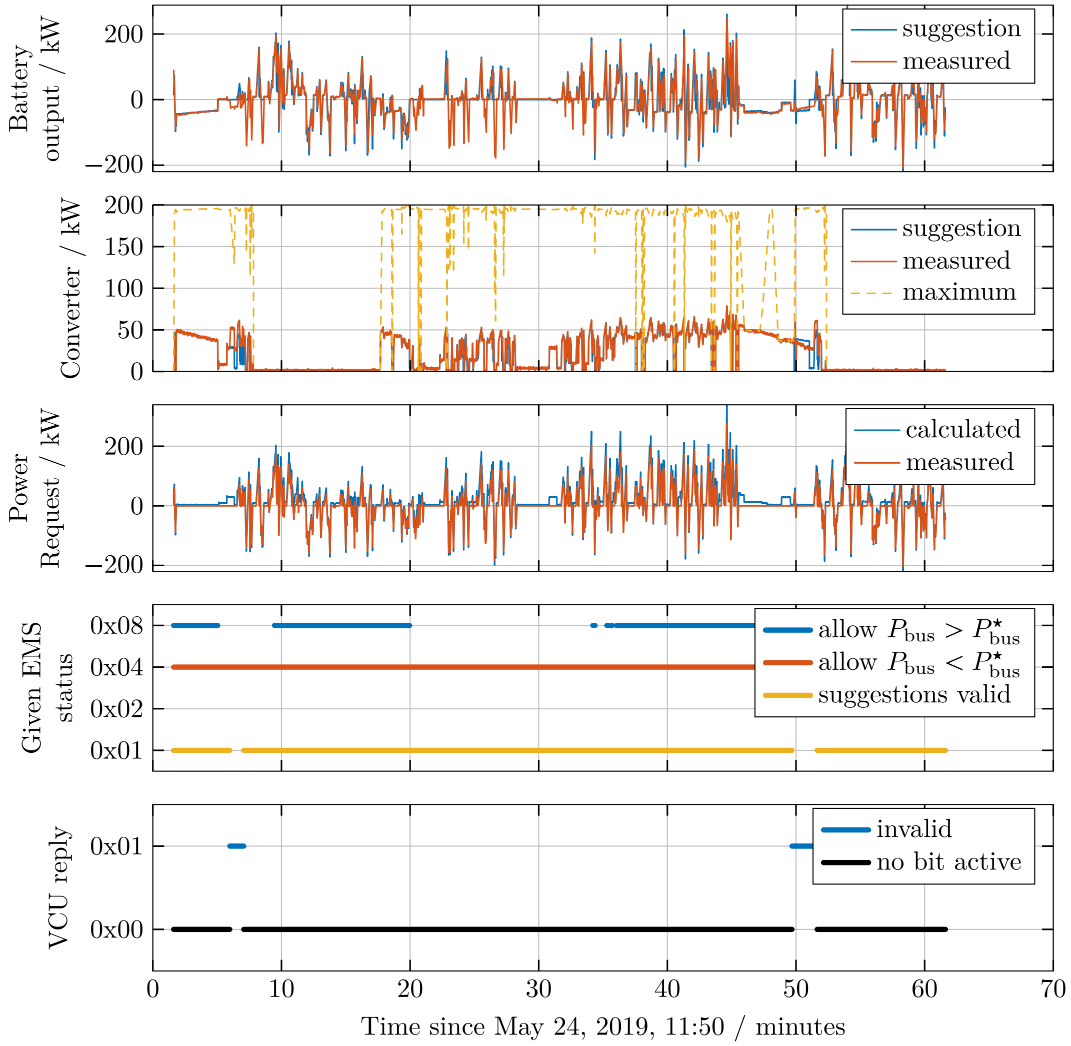

Figure 9: Measurement data and control signals related to the energy management. The shown data was recorded on 24.05.2019 between 11:50 and 12:50. The VCU reply bit 0x01 refers to the “invalidity” bit in the provided suggestion. Consequently, VCU switches automatically to the backup EMS and ignores the suggestions.

The SOC limit is respected as part of the supervisory control in the SOC limiter. Compared to the target SOE value of 80% the SOC limit of 85% is too restrictive. Luckily, the VCU ignores the suggestion to dissipate excess power in the braking resistor and still charges the battery, which is of course reasonable as the "real" battery SOC limit is much higher. The upper limit in the EMS handler will thus be increased in future software versions after v1.12.1.

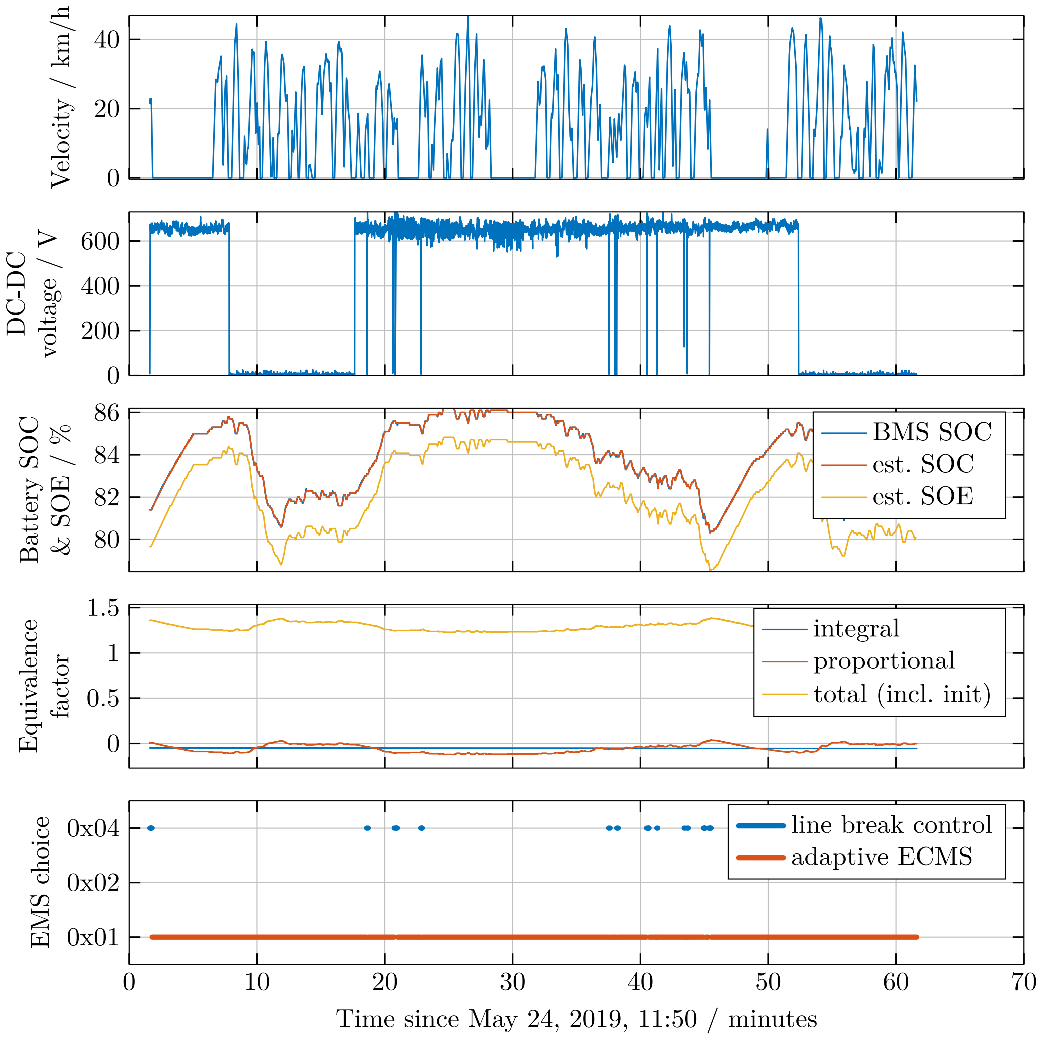

Figure 10: Data related to the EMS suggestions provided by the supervisory control with a focus on the adaptive ECMS and the line break control. Except from some short instances indicated with the blue dots in the lowest graph, the EMS handler forwards the suggestions provided by the adaptive ECMS module.

As shown in Figure 10, the EMS handler occasionally switches from the adaptive ECMS strategy to the line-break control. The drops of the DC-DC voltage measurements (suggesting actual line breaks) depicted in the second graph match nicely with the instances where the line break control is used. This section analyzes the results of this control in more detail. All results are obtained with the software version v1.12.1.

Figure 11 shows the road map on 24.05.2019 at 11:58. The dots in cyan show the nodes of the map that refer to a line break probability greater than 25%. Hence, at least in every fourth trip on the same route there was indeed a line break detected at the same location. The asterisks in red show the equivalent time-based data of at the corresponding GPS locations. The two data sources match well in most locations where the vehicle was driving in the analyzed time frame. Compare the road map to the driven trajectory shown in Figure 7.

The result of the line break control is shown in Figure 12. Compared to the previous figures this figure shows only a short excerpt of the data recordings.

Figure 11: The road map as present on 24.05.2019 at 11:58. The colored nodes indicate the line breaks that were mapped in previous runs. The red asterisks show the measured line breaks on 24.05.2019 between 11:50 and 12:50. Note that the vehicle was not driving on the entire road map during this time period.

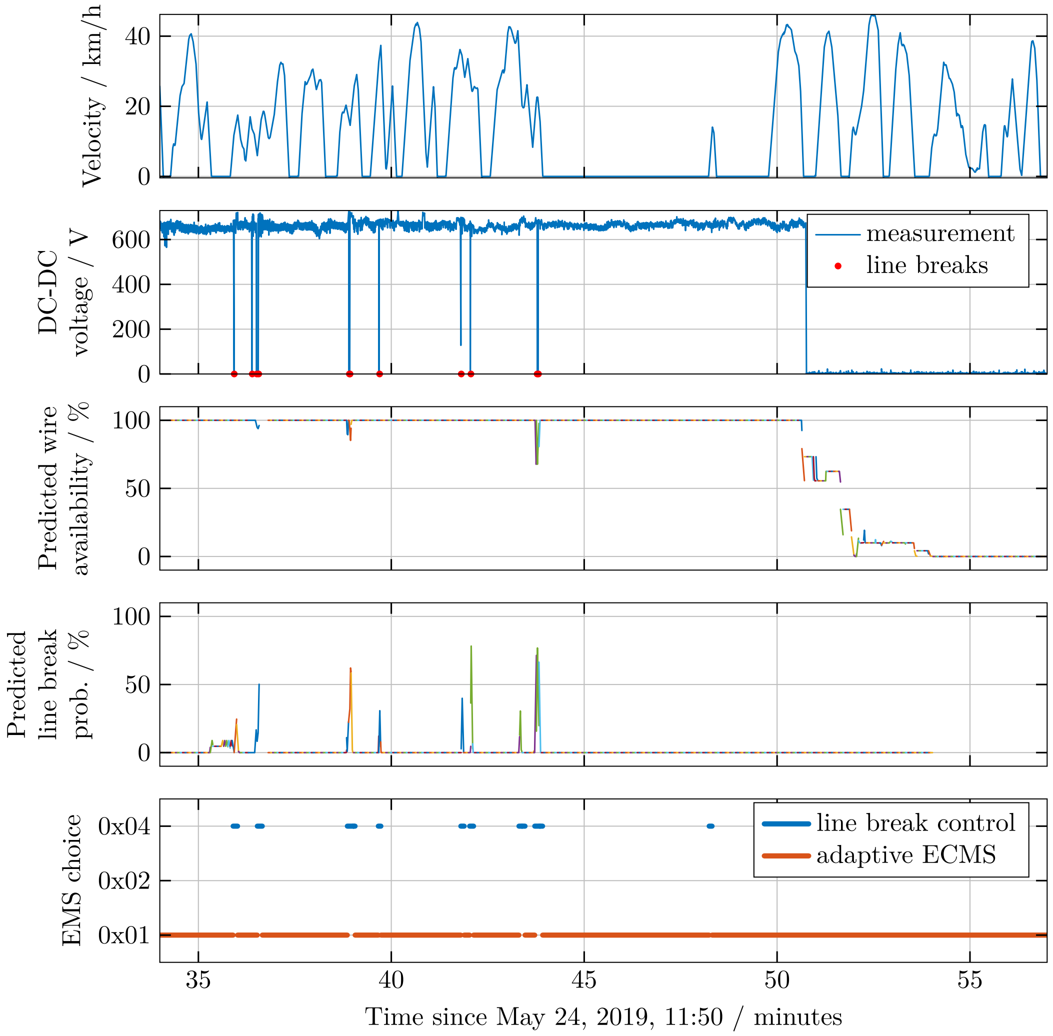

Figure 12: Excerpt of the time-based signals related to the line-break control strategy. The two uppermost graphs and the graph on the bottom once more depict the velocity profile, the DC-DC voltage, and the EMS choice for a reference. The third and the fourth graphs depict the predicted data published by the SLRM.

Based on the settings of the software version v1.12.1, the SLRM publishes new prediction messages every three seconds with a prediction horizon of 60 meters. Each prediction is indicated with a different color in Figure 12. As we can clearly see, the probability of the wire availability corresponds to the DC-DC voltage. The probability is around one where the voltage is around 650 V and drops to zero where the voltage is low. The transition between 51–52 min represents two specific features of the chosen prediction mechanism. On the one hand, the location estimates at which the collectors are disconnected from the grid and pulled down are not always equal. As a result, the stored data in the nearby nodes is partly ambiguous. On the other hand, in order to visualize data, it is converted from the distance domain to the time domain via the expected velocity profile. This conversion, however, is fraught with uncertainty and thus introduces an additional ambiguity. The reason for the low probability around 10% between 52–54 min may be due to merging procedures of the road map building process or caused by a real situation where the bus driver once continued driving with connected collectors for two minutes.

The predicted line break probability captures most of the actually occurring line breaks detected in this run, which are indicated with the red dots in the second graph. Correspondingly, the EMS handler switches from adaptive ECMS mode to line break control mode as shown in the graph at the bottom. In order to visualize this mechanism in more detail, Figure 13 depicts an even shorter time frame. Both line breaks are in this case predicted accurately and controlled as expected. In the first instance, the line break control is active for approximately 12 seconds. In the second instance, the line break control is active for approximately 4 seconds. This difference is mostly due to the difference in speed: The vehicle travels about twice as fast in the second instance compared to the first one. The detection of the line breaks by the Grid Estimation module as shown as red dots in the second graph lags slightly behind the actual measurement. The reason for this time delay is that the line breaks are only detected every second. Accordingly, such delays of up to one second are to be expected.

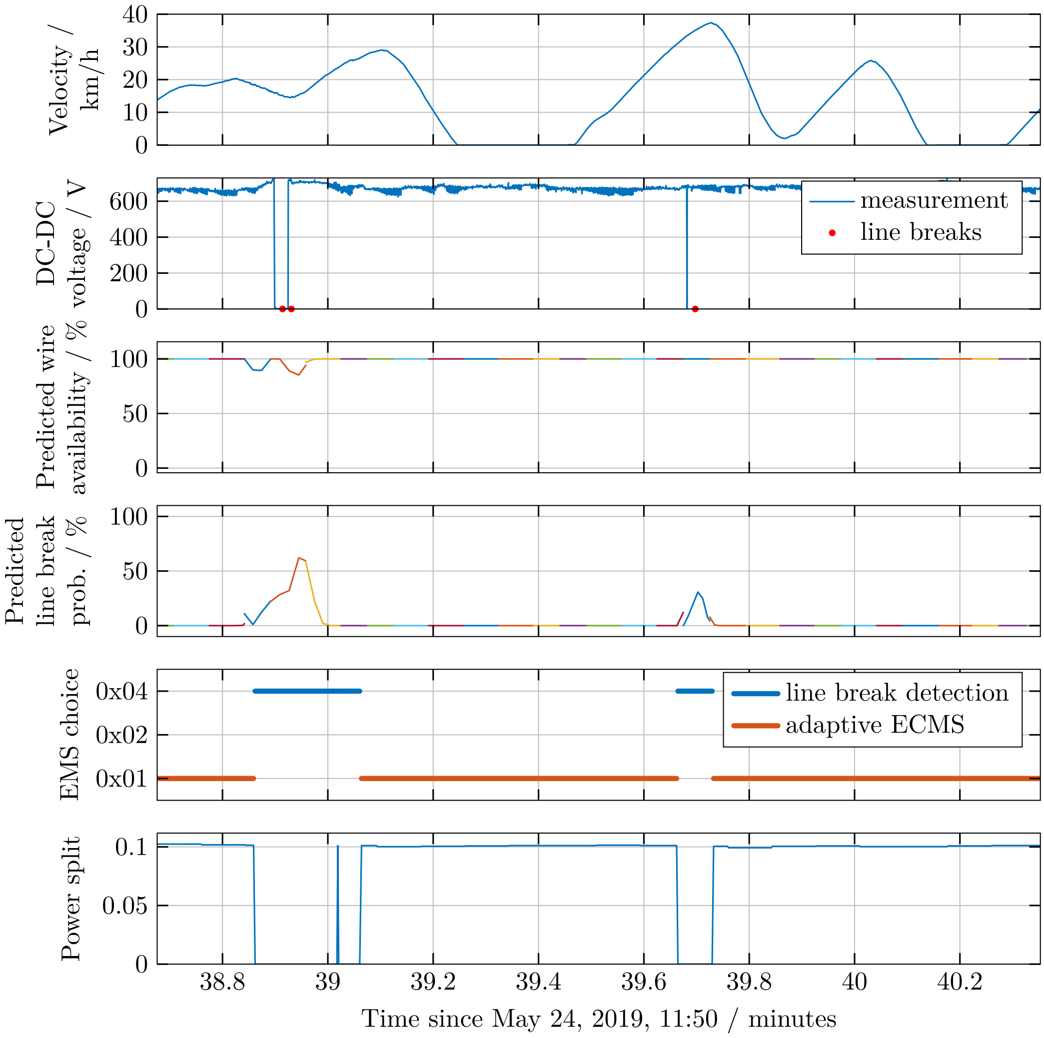

Figure 13: Detailed view of Figure 12 between around 12:28 and 12:30. The individual line break predictions clearly indicate the line breaks. In order to visualize the data, the predictions are converted from the distance domain to the time domain. Moreover, the predicted data is only shown for the duration until the next prediction message is available. In reality, each prediction covers a much longer time duration, which would, however, confuse the representation here.

2.2.3 Field campaign

As part of the overall project «SwissTrolley plus» a field study has been conducted, where a comparable trolley bus of an older generation was driving the same bus route at the same time than the «SwissTrolley plus» demonstrator vehicle during a period of three weeks.

The goal of this field campaign is to evaluate the performance of the «SwissTrolley plus» bus by comparing its energy consumption to the one of standard trolley buses. As the «SwissTrolley plus» can run with both the backup EMS implemented on the vehicle control unit (VCU) and the supervisory control software described in this text, the field campaign was set up to cover both versions, too. This section focuses mainly on the comparison between the backup EMS and the supervisory control software. As the behaviors of both EMS strategies are very similar in different periods of the year, the following analysis is assumed to be representative for the comparison in general.

More details on the comparison to the standard trolley bus is given in the annual/final P&D&L report of HESS and VBZ.

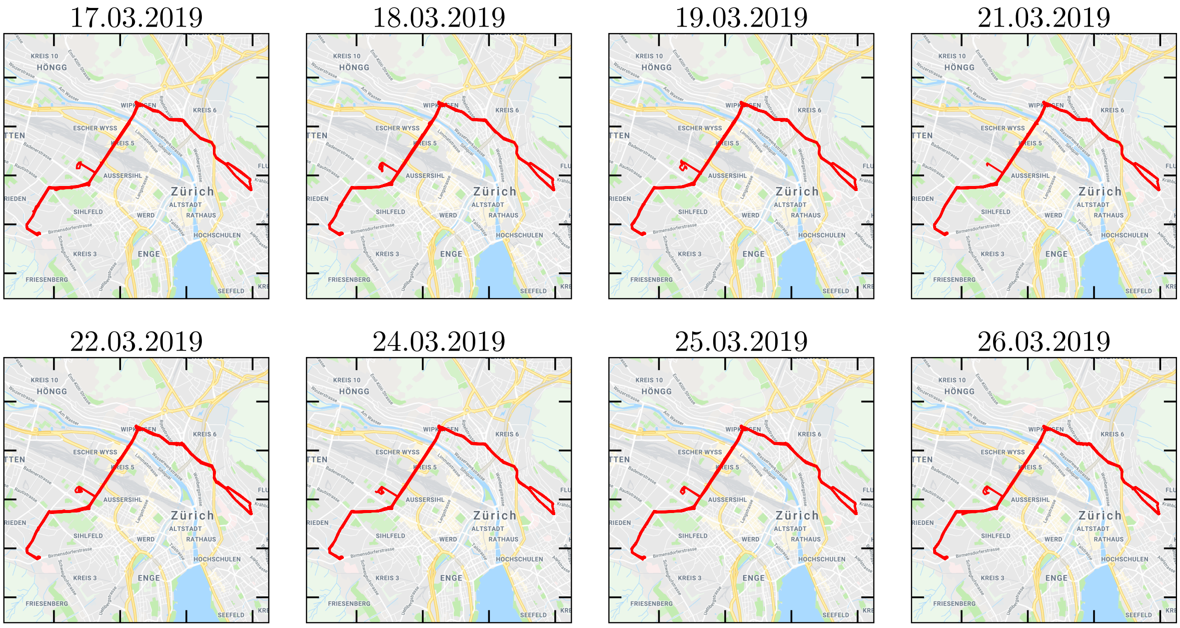
17.03.2019 18.03.2019 19.03.2019 21.03.2019

22.03.2019 24.03.2019 25.03.2019 26.03.2019

Figure 14: Geographic representation of the driven routes during the field campaign. As indicated via the shown GPS trajectory the «SwissTrolley plus» prototype vehicle was always driving the same bus route, i.e., route 33.

The field campaign was conducted during about three weeks from which eight days are similar enough to be used for the comparison analysis. The GPS trajectories that were recorded during these days are shown in Figure 14. Key numbers related to the entire period between 17.03.2019 and 26.03.2019 are depicted in Table 1. Two out of ten days are declared as invalid and marked accordingly. On both days, the vehicle was serving another bus route, hence the measurement data would not be directly comparable. The active EMS alternated between the HESS backup control of the VCU and the adaptive ECMS of the supervisory control software. On the valid days, the vehicle was driving between 17.8 h and 19.8 h and covered daily distances between 267.3 km and 306.9 km. The last column depicts the average ambient temperature. The software version of the adaptive ECMS that was running was v1.11.2, where its target SOE was set to 70%.

Date	Active EMS	Duration	Distance	Ambient temp.
17.03.2019	HESS backup	17.8 h	267.3 km	8.1 °C
18.03.2019	Adaptive ECMS	17.8 h	283.6 km	3.2 °C
19.03.2019	HESS backup	17.9 h	283.5 km	2.9 °C
20.03.2019	Adaptive ECMS	*invalid due to route changes*		
21.03.2019	HESS backup	17.0 h	270.3 km	5.8 °C
22.03.2019	Adaptive ECMS	19.7 h	306.9 km	8.5 °C
23.03.2019	HESS backup	*invalid due to route changes*		
24.03.2019	Adaptive ECMS	19.8 h	299.6 km	10.6 °C
25.03.2019	HESS backup	18.0 h	283.5 km	6.9 °C
26.03.2019	Adaptive ECMS	17.9 h	283.6 km	4.0 °C

Table 1: Dates and important metrics of the field campaign. The Adaptive ECMS was running on software version v1.11.2, where the target SOE was set to 70%. The measurement data of 20.03.2019 and 23.03.2019 is not respected in the analysis as the vehicle was driving on other bus routes than route 33. On all other dates the vehicle was driving very similarly, as indicated by the depicted metrics and the GPS trajectories of Figure 14.

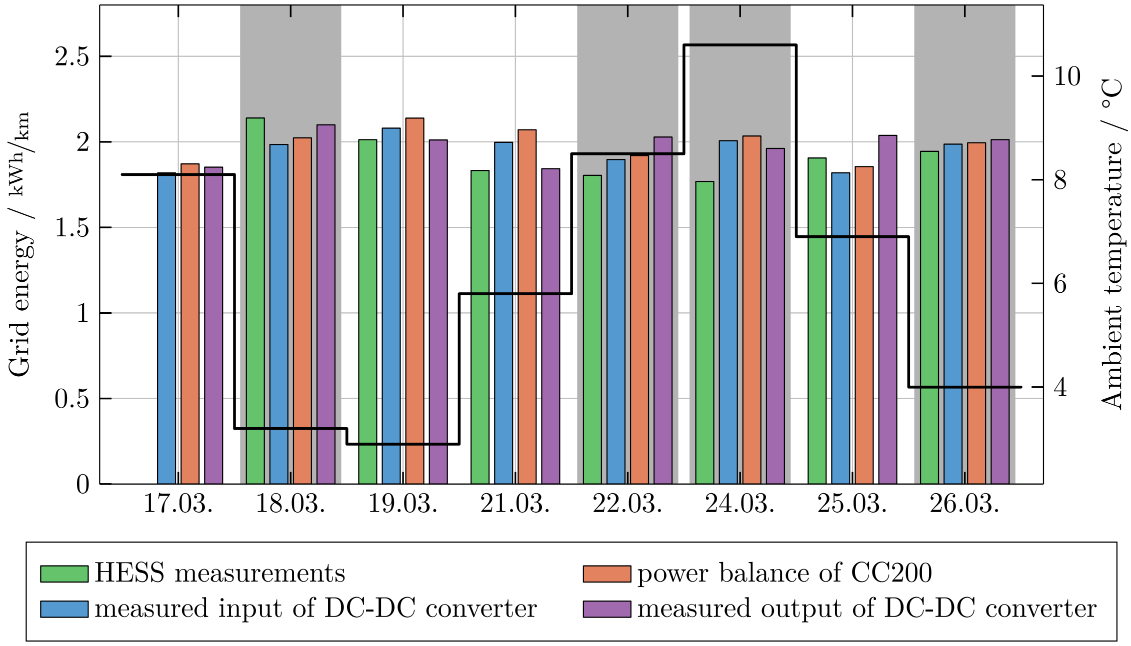

Figure 15: Energy consumption of the «SwissTrolley plus» prototype measured or estimated at the grid. The HESS measurement data of the first day is missing. The gray bars mark the days where the adaptive ECMS was active. The black line shows the average ambient temperature.

The energy consumption during the field campaign is shown in Figure 15. Unfortunately, the various listed measurement methods do not precisely agree on the energy consumption. The data by HESS indicated in green is recorded with measurement equipment that was specifically installed for the field campaign. It is mainly used to compare energy consumption to the standard trolley bus as described in the following section. The measured input of the DC-DC converter is calculated by multiplying the measured voltage and current at the grid side of the DC-DC converter. The power balance values refer to the sum of products of the traction inverter voltage and the current, and the battery voltage and current to the battery, which is then converted to grid energy via a Willans model of the DC-DC converter. Finally, the measured output of the DC-DC converter is given by the product of the current and voltage of the converter at the bus side, also converted to grid energy via the Willans model.

The adaptive ECMS maximizes the system's efficiency by splitting the instantaneous power demand among the traction battery and the electric grid in the best possible way. As the overhead grid is considered a part of the system, the adaptive ECMS aims to minimize the power fed into the grid as opposed to the power consumed by the bus. Thus, losses occurring within the grid are also minimized.

The backup EMS implemented on the VCU uses a heuristic strategy backed with look-up tables for the desired battery and converter currents as a function of the battery SOC. In essence, the backup EMS aims to recharge the battery more the lower its SOC is. Only above 95% the reference of the battery operation is actively set to discharge mode. As a result, the battery SOC is expected to be rather high, without having a specific target value.

The two histograms of Figure 16 show the relative duration the battery remained in a particular operating point. On the left, the distribution by the battery SOC is shown. On the right, the breakdown by the battery charging current is shown, where positive values indicate charging currents. From the distribution by the SOC we can clearly see that the backup EMS keeps the battery in general at higher SOC values,

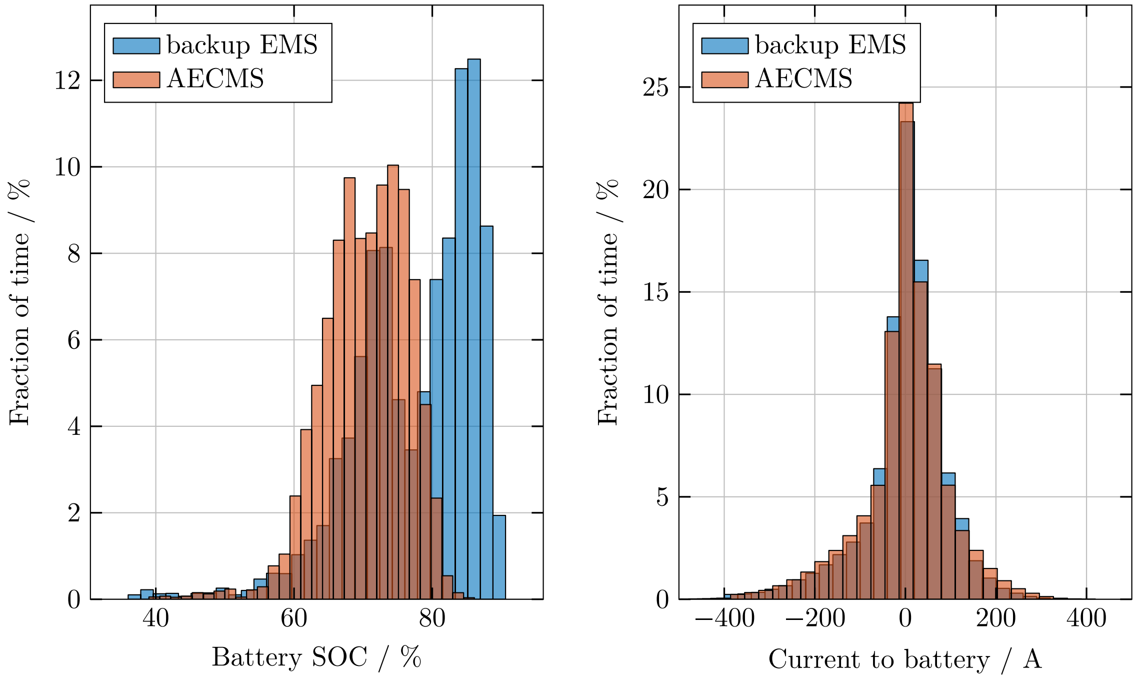

Figure 16: Histograms of the battery operation points. On the left, the fraction of time in which the battery is operated in certain SOC ranges is indicated. On the right, the distribution by the battery charging current is shown.

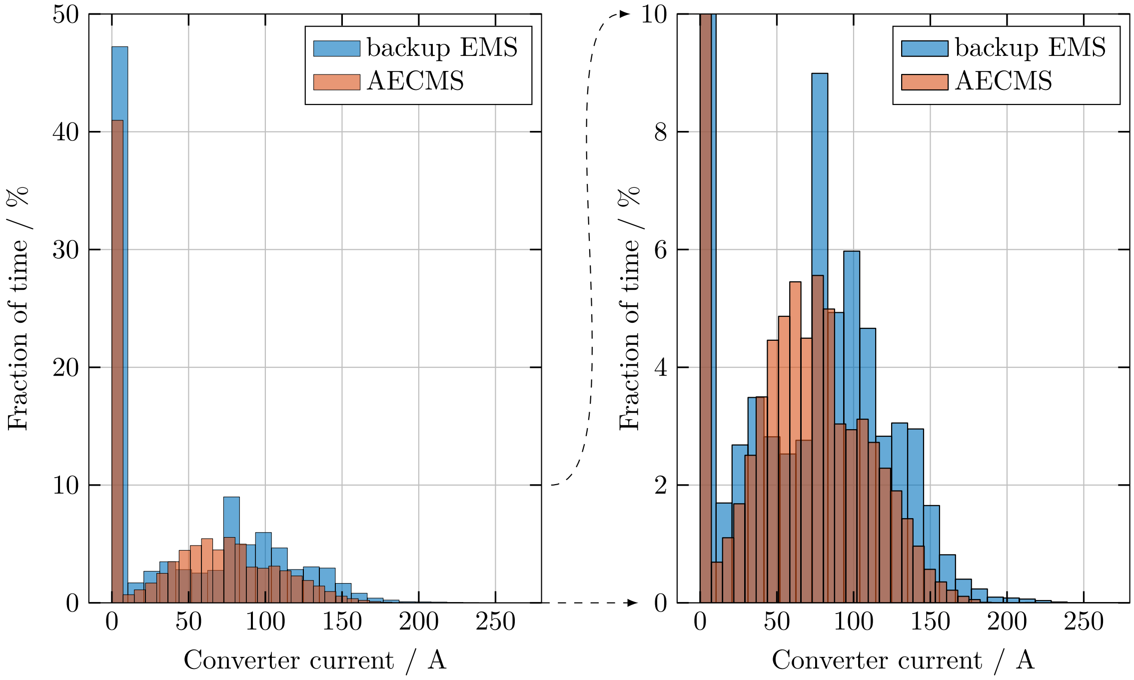

Figure 17: Histograms of the converter current. The right graph shows the same data as the left graph, but with a detailed view on the fraction of time between 0–10%.

particularly often around 85%. The adaptive ECMS on the other hand clearly aims for an SOC around the target value of 70%. The distribution of the battery current is very similar for both EMS types.

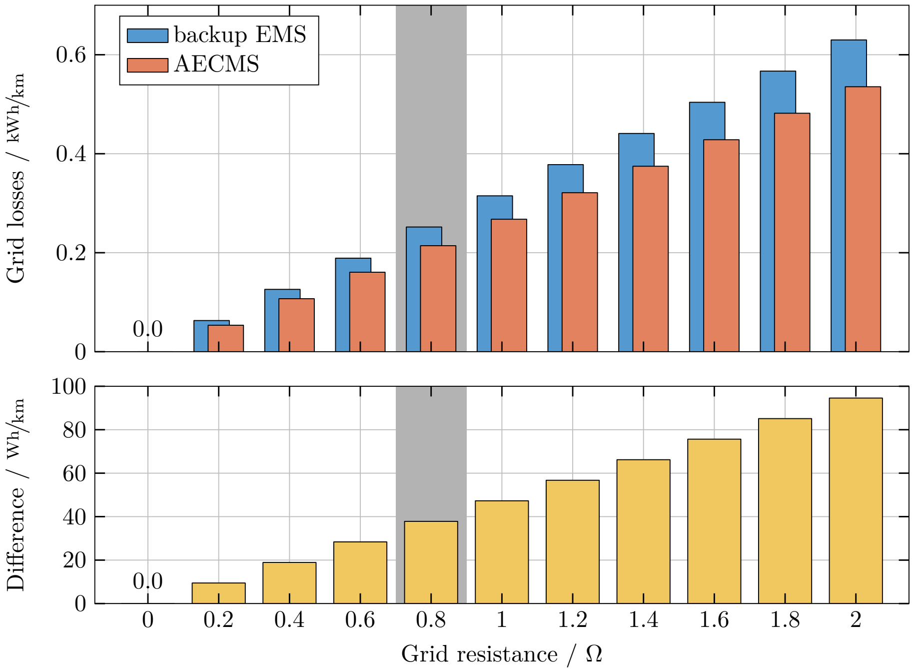

Figure 18: Grid losses in energy per distance as a function of the grid resistance. The backup EMS causes greater grid losses since the current drawn from the grid is typically greater too, as indicated in Figure 17. The lower graph shows the difference in values between the backup EMS and the adaptive ECMS and thus shows the estimated improvements with the adaptive ECMS. The gray bars mark the currently used grid resistance value for the adaptive ECMS.

However, the distribution of the DC/DC converter current shown in Figure 17 differs notably for the two EMS types. The backup EMS draws current from the grid much more often at higher values than the adaptive ECMS. On the other hand, the adaptive ECMS prefers charging at lower currents around 60 A. This observation indicates that the adaptive ECMS not only aims to reduce the power drawn from the grid but the electric power fed into the grid by the electricity supplier. Hence, it respects the grid resistance.

Unfortunately, there is no mature method available yet to determine the electric resistance of the grid. We can only assume based on a simple electric schematic that the resistance is dependent on the distance between the vehicle and the feed point that delivers the electric power. But as we do not have an online algorithm that identifies these locations the resistance is currently assumed to be constant at 0.8 Ω.

Motivated by Figure 17 and the goal of the adaptive ECMS to reduce the grid energy at the feed points, the assumed grid losses are analyzed in more detail. Based on the simple equation $P_{\text{loss}} = I^2 \cdot R$ we can calculate the power loss of the grid due to the consumed current I and the assumed constant resistance R. Figure 18 shows the results of this calculation converted to units of energy per distance. The grid resistance is thereby varied in the range of 0–2 Ω. The value used in the adaptive ECMS is marked with the gray bar.

As expected, the adaptive ECMS is able to significantly reduce grid losses. However, the achieved improvements are quite small compared to typical energy requests depicted for example in Figure 15, e.g., 40 Wh/km is only about 2% of the average energy request of approximately 2 kWh/km.

One reason for the gain being not larger is probably the SOE target value of the adaptive ECMS. With only 70%, this value is significantly lower than the typical values achieved by the backup EMS, leading to a lower system voltage and thus lower ohmic efficiency. The benefits of the adaptive ECMS compared to the backup EMS are thus expected to become bigger when the target SOE is increased.

Figure 19: Manipulated trolley bus route 33 with an additional grid-free sector from Schiffbau to Triemli and back. Orange parts of the route represent grid-free sectors, while blue parts represent section with available overhead grid.

2.2.4 Predictive EMS using MPC

A predictive EMS can reduce the grid losses discussed in the previous section even more. Compared to the adaptive ECMS, a strategy that has perfect knowledge of the future could potentially exploit the entire driving missing and draw energy from the grid whenever the losses are expected to be small.

Since the ohmic losses during the transmission of energy via the overhead line increase quadratically with the current consumed, the optimum control naturally attempts to reduce power peaks. An explicitly formulated prevention of peak loads is therefore not necessary as we will see below and in particular in Figure 21. Assuming that the ohmic resistance of the overhead wires is constant, the optimal strategy results in more or less constant current values such that high power peaks are prevented but still enough energy is drawn.

A detailed view on such a strategy is depicted in Figure 20. It shows that the non-causal solution is able to keep the converter power at very steady loads around 50–60 kW. In contrast to that, the adaptive

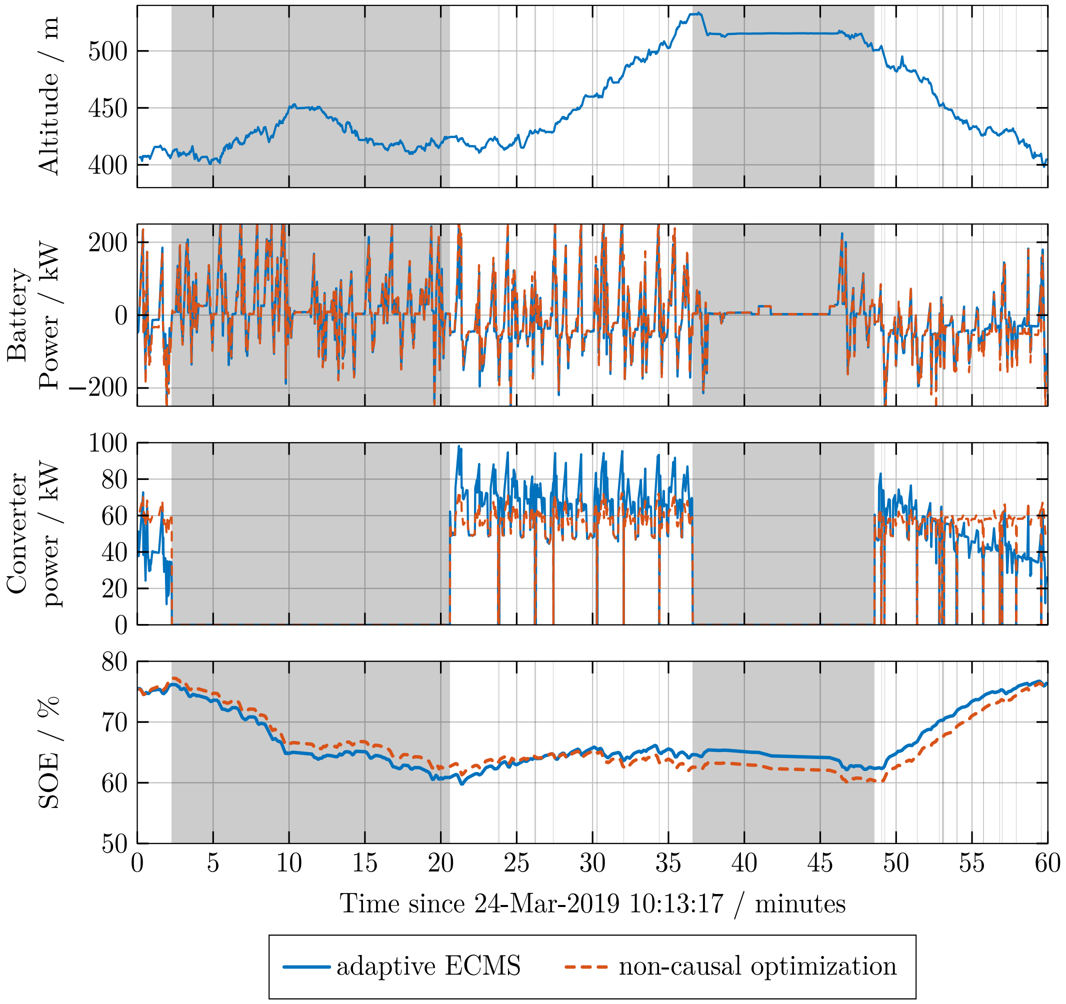

Figure 20: Comparison of a non-causal solution with the adaptive ECMS. The top graph shows the altitude profile. The second and third graphs show the battery discharging power and the converter power, respectively. The lowest graph shows the battery SOE. The gray regions indicate the grid-free sections or the line breaks.

ECMS is influenced by the current SOE values: When the current SOE value is low, e.g., at about 20 min after the long grid-free section, the converter power is typically higher. When the current SOE value is high, e.g., after the long downhill section at the end of the shown data, the opposite can be observed.

In order to demonstrate the benefits of MPC compared to the backup EMS we design a more demanding scenario. First, the grid-free section around Hardbrücke and Albisriederplatz is extended to a cover the complete part south west of the bus stop Schiffbau. The resulting section is 8.5 km long and covers 52% of the total round trip distance. A geographic map thereof is depicted in Figure 19. Second, the battery capacity is reduced from 80 Ah, which refers to the 60 kWh of the current «SwissTrolley plus» prototype, to 50 Ah. The voltage, the inner resistance, and the weight are assumed to remain constant.

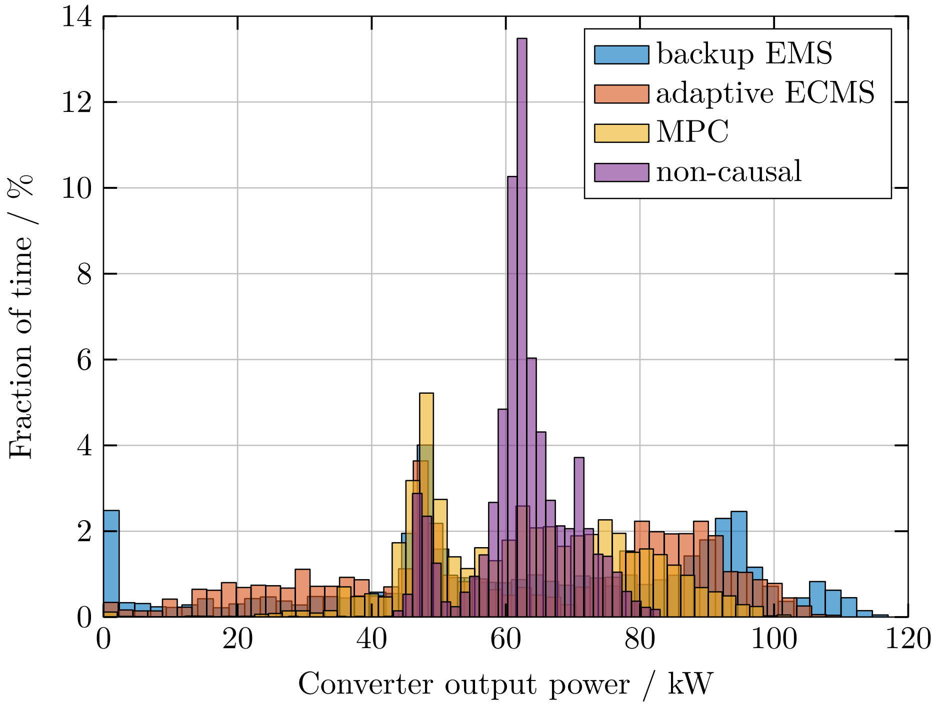

Figure 21: Histogram of the positive converter output power of the non-causal solution and the three present online strategies. The peak around 50 kW is due to the speed-dependent power limitation of the DC-DC converter.

The resulting distribution of the converter power is depicted in Figure 21. We can clearly see that all energy management strategies that respect the losses of the power transmission via the overhead wires, i.e., the adaptive ECMS, the MPC, and the non-causal optimization, reduce the power peaks in order to be more energy efficient. In contrast, the backup EMS remains idle for some time and generally spends less time at medium power outputs. In order to still be able to provide the missing energy, the converter is operated at higher power peaks.

From within the strategies that consider the grid losses, we see that MPC can reduce these peaks even further. Here, the forward-looking nature of the strategy makes it possible to charge the battery more gently after a grid-free section without having to fear that the next grid-free section is imminent and the battery charge is not sufficient to pass it. Ideally, with perfect knowledge of the future, the strategy would operate the DC-DC converter as indicated by the non-causal solution. In the given scenario, this means that the converter runs at approx. 60 kW most of the time. The other peak of the distribution around 50 kW is due to the speed-limited operation of the converter which prevents the collector shoes from being welded to the overhead wires.

By reducing the storage capacity of the battery, the non-predictive EMS strategies typically recharge the battery after the grid-free sectors even faster, i.e., with higher current. Consequently, these strategies yield higher energy losses in the grid and in the battery. The corresponding energy savings are depicted in Figure 22. We can see that for smaller battery capacities the difference to the non-causal solution generally increase for the non-predictive strategies. Only the predictive MPC is able to keep the additional energy consumption at around 4%. The slight decrease towards smaller capacities is most likely due to numerical issues or imperfect predictions.

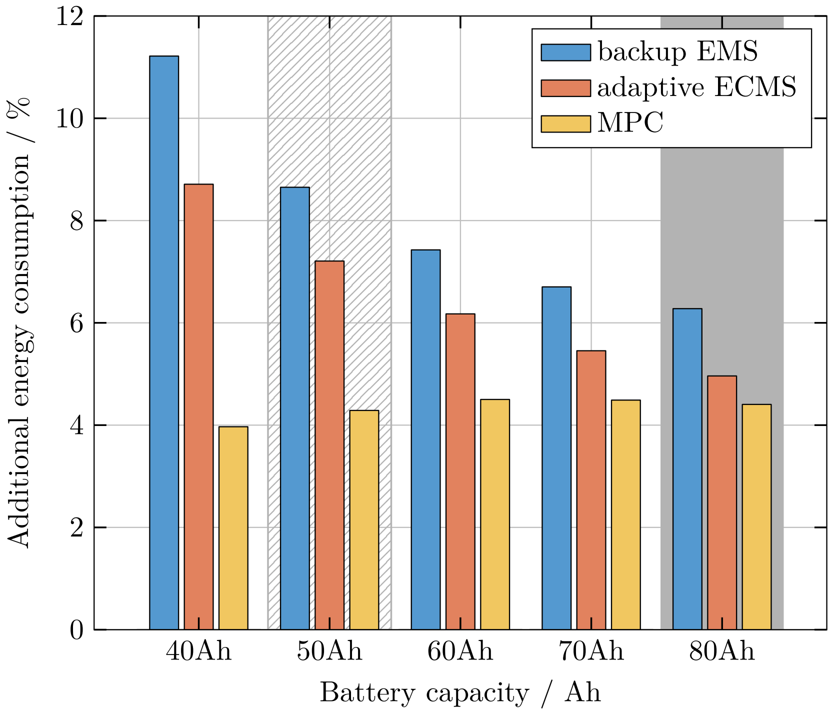

Figure 22: Additional energy consumption at the grid’s feed points, compared to the non-causal solution. In order to account for SOC trajectories that are not charge sustaining, specific non-causal solutions are calculated for each online algorithm. Thereby, the final SOC of the non-causal solution is set to the final SOC that resulted via the corresponding online strategy. Moreover, all strategies are evaluated on four battery sizes ranging from 40 Ah to 80 Ah. The gray area indicates the size of the battery that is present on the «SwissTrolley plus» prototype. The striped area indicates the battery size that is used for the comparison presented in Figure 21.

3 Battery experimental characterization and SOH model

The work at BFH-TI aims at developing tools that define the most suitable operating window of the battery that guarantees maximum battery lifespan. To develop such tools, we have been continuously characterizing and testing several battery cells under different testing conditions. The experiments are designed to gather data for characterizing the battery behavior over time. This data will allow to quantify the aging effects in terms of different factors such as charging and discharging capacity de-crease, impedance growth, internal resistance increase, energy and power dissipation, etc. The output of the extensive experimental campaign is a SOH model able to estimate the battery remaining life (until SOH 80%) based on specific operating conditions and driving profile. The model could also be used in the design phase, to size the battery system according its utilization.

3.1 Procedures and methodology

3.1.1 Experimental research and methods

The experimental research is divided into two experimental phases. In Phase 1, a combination of several parameters, which reflect the real battery usage of the trolley bus, is used to age the cells. Here, the goal is to identify a combined effect of different parameters on the cell performance over time. In Phase 2, the effect of a single testing condition or single parameters on cell aging is investigated by testing cell performance over time. Consequently, the goal of Phase 2 is to isolate the influence of each testing parameter on the cell performance over time to determine the distinct influence of each parameter on the battery lifespan.

The most significant results of Phase 1 were already presented in the Annual Report from 31.01.2017 It was found out that LTO batteries present reproducible and stable behavior over different samples, the low internal resistance if compared to LFP or NMC-G cells makes calendar and cycling aging slower. Moreover, LTO batteries presents high and stable performances over a wide range of temperatures (-5 to 45°C). This final report shows the concept of and results obtained in Phase 2.

Two types of tests were conducted. In the first one, cells are fully charged and discharged, resulting in a depth-of-discharge (DoD) equal to 100%. In the second one, cells are partially charged and discharged, hence DoD is always less than 100%. The first group of tests was done to investigate the dependency of aging on C-rate and temperature, whereas the second group was done to investigate the effect of DoD and voltage levels on aging. The test regimes for the first and second types of tests are depicted in Figure 23 and Figure 24, respectively. Both regimes are composed of aging cycles and reference or diagnostic cycles that are repeated periodically. Aging cycles are done under the corresponding testing conditions listed in Table 2 and Table 3 (*tested with the first batch of cells from the battery manufacturer, all other parameters are tested using the second batch of cells provided by the same manufacturer). Reference or diagnostic measurements follow the same test conditions and thus allow a direct comparison between all cells with respect to capacity and AC- and DC-resistance variation during aging. A detailed description of all steps is depicted in the appendix.

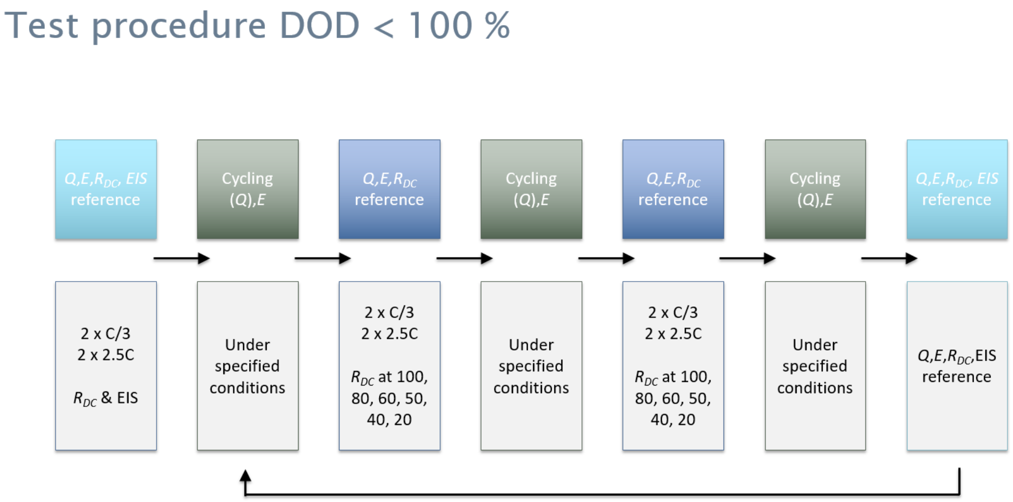

Figure 23: Test regime for DoD = 100%

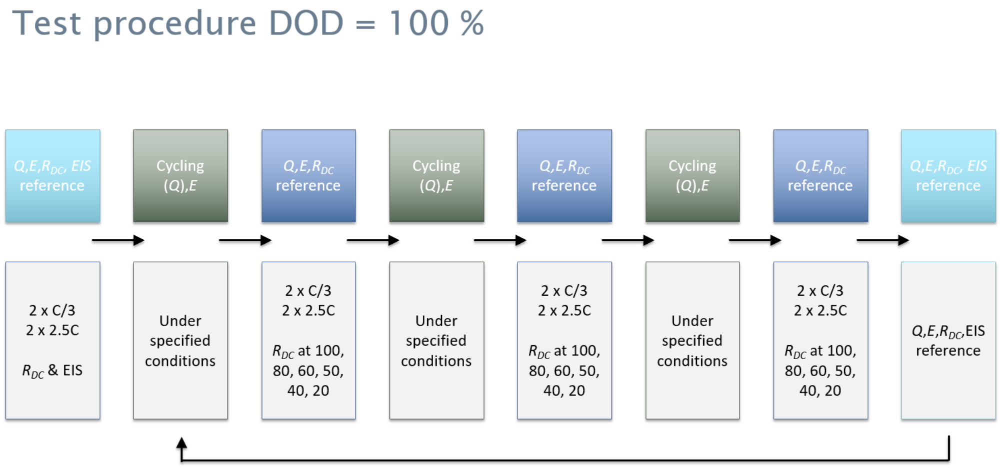

Figure 24: Test regime for DoD < 100%

All cycling measurements were realized in temperature chambers (ESPEC ARU1100, Vötsch VT4004, ESPEC LU114, CTS DE-54-QS) under controlled temperature conditions. The temperature changes were set to a rate of approximately 1°C per minute. After the target temperature was reached, the cells were kept under open circuit voltage conditions for a period of 240 minutes to guarantee constant temperature conditions prior to experiments. The temperature was monitored at one or two points on the cells using highly accurate Pt100 sensors. All temperature readings at zero load conditions, i.e., prior to each cycling step, were within ±0.1°C of the set chamber temperature.

In the following text, figures, and tables, C stands for the charge or discharge rate and is calculated using following formula:

$$\text{C-rate} = \frac{I}{Q_n},$$

where C-rate has the physical unit C or h^{-1}, current I is in units of A (ampere) or mA and the nominal charge capacity Q_n is in units of Ah or mAh. The changes in the DC-resistance (R_{DC}) of the cells were monitored using the same cell testing equipment (PEC ACT0550 and PEC SBT10050). In these measurements, cells undergo four different DC-testing regimes (see Figure 26 to Figure 29). For DC-testing method 1 (DC-1), the lab equipment's DC-measurement standard, the cells were discharged during 50 ms discharge with 2 C and allowed to rest during 50 ms. The DC resistance was calculated automatically by the tester by following $R = \Delta U / \Delta I$, where ΔI was 40 A and the resulting ΔU (= U2 - U1) is the difference between the voltage after the 50 ms discharge (U1) and the voltage after the 50 ms rest time after the discharge. The DC-testing method 2 (DC-2) stems from the Norm EN 61960 and is composed of a 5 s discharge at 2 C followed by a 5 s charge at 1 C. U1 and U2 for ΔU were taken at the end of the 5 s discharge at 2 C and immediately at the start of the 1 C charge, respectively. Thus, ΔI equals 3 C or 60 A. DC-testing method 2 (DC-2) is a modified method from a review publication on DC-testing methods and is composed of a 5 s discharge at 2 C followed by a 5 s charge at 1 C. U1 and U2 for ΔU are taken at the end of the 5 s discharge at 2 C and immediately at the start of the 1 C charge, respectively. Thus, ΔI equals 3 C or 60 A. DC-testing method 3 (DC-3) stems from the Norm EN 61960 is a modified method from a review publication[1] on DC-testing methods and followed a regime consisting of a 10 s, 0.2 C discharge prior to a one-second, 1 C discharge equaling ΔI = 20 A. U1 and U2 were taken at the end of the 10 s and 1 s discharging currents, respectively (

Figure 30). The impedance or frequency dependent resistance of the cells was measured periodically using an electrochemical impedance spectrometer (EIS) from Gamry (Gamry 3000). For all EIS tests, the cells were held at a specific state of charge (SoC) for approximately 30 minutes before testing. The EIS tests were performed galvanostatically (an AC current was used as probing signal to generate a response potential) by applying I_{rms} = 100 mA from 10 mHz to 5 kHz. During these measurements, the doors of the temperature chambers were kept open, as a result, the cells were exposed to a room temperature of 24.5 ±1 °C.

The coulombic efficiency (CE) method was performed on three cells at 0.05 C and with a DoD of 100% at temperatures -5 °C, 25 °C and 45 °C. The charge and discharge were done at constant current only. No pause was used after the charge or discharge and vice versa. CE-measurements were performed for 30 to 33 days.

Table 2: Test matrix for the aging dependency on C-rate; 8 cells undergo tests with a DoD = 100%. *cells from batch 1, all others from batch 2

---

[1] Schweiger et al. "Comparison of Several Methods for Determining the Internal Resistance of Lithium Ion Cells", Sensors 2010, 10(6), 5604-5625

Parameter of interest	Chamber set temperature / °C	SoC range / %	C-rate / h^{-1}
C-rate	- 5	0 – 100	1
	10		1
			2.5
	25		1*
			2.5*
			5*
	45		1
			2.5

Table 3: Test matrix for the aging dependency on DoD and SoC range; 13 cells undergo tests with DoD < 100%. *cells from batch 1, all others from batch 2

Parameter of interest	Chamber set temperature / °C	SoC range / %	DoD range / %	C-rate / h^{-1}
DOD- and SoC-range (DOD = 80, 65, 25, 20 and 10%)	25	10 – 90*	80	2.5
		10 – 20	10	
		80 – 90	10	
		55 – 80*	25	
		20 – 45*	25	
		45 – 55	10	
		20 – 85	65	
		60 – 85	25	
		60 – 80	20	
		50 – 70	20	
		40 – 60	20	
		30 – 50	20	
		20 – 40	20	

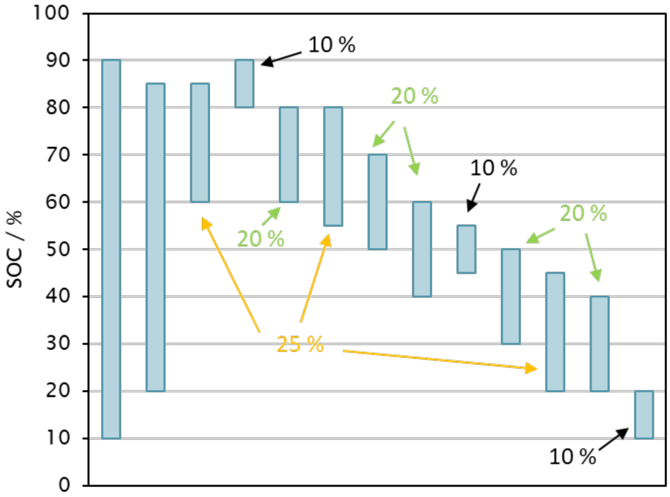

Figure 25: SoC ranges investigated in this study. The inserted values represent the resulting depth of discharge or DoD.

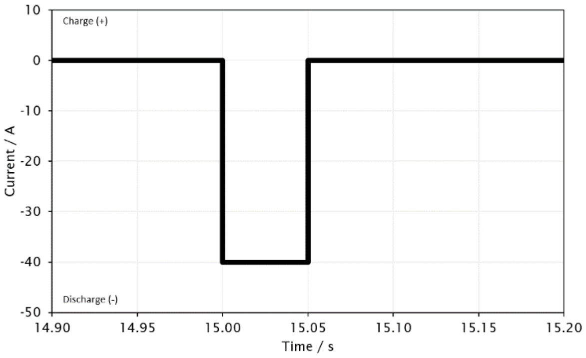

Figure 26: DC-1, current pulses

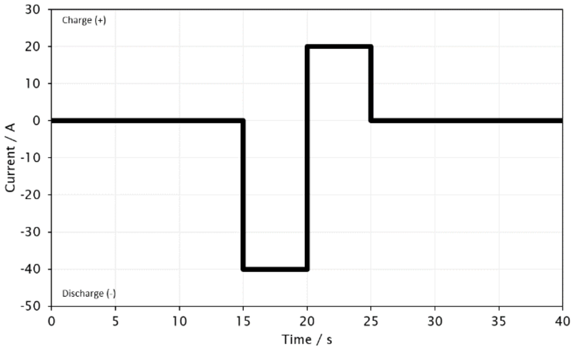

Figure 27: DC-2, current pulses

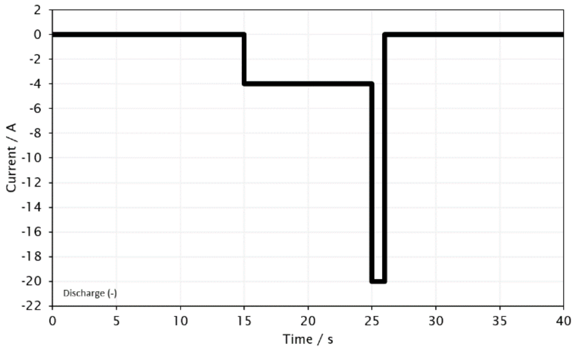

Figure 28: DC-3, current pulses

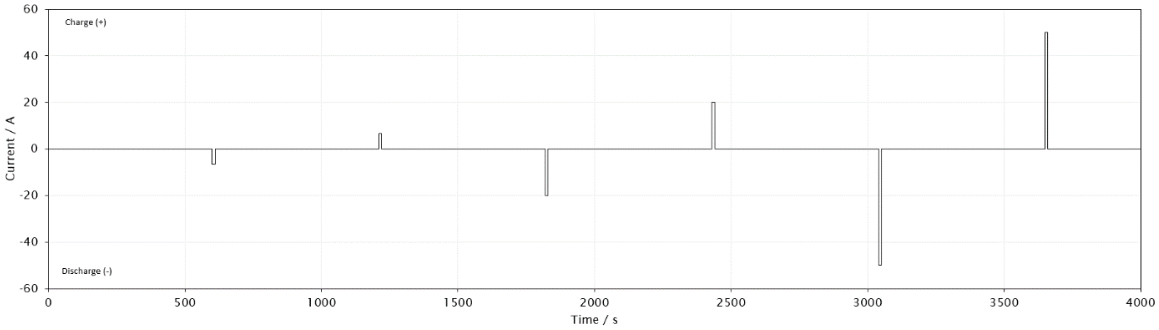

Figure 29: DC-4, current pulses

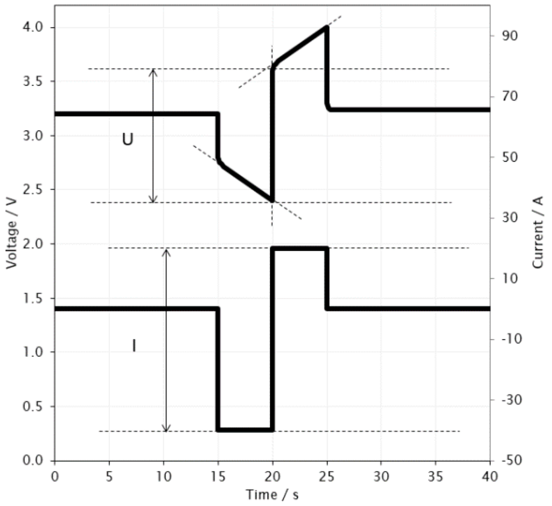

Figure 30: Linear extrapolation of voltage responses for the identification of U1 and U2 for DC-2

For all cycling experiments with DoD = 100%, the cells were charged and discharged using a constant current-constant voltage (CC-CV) charging and a constant current (CC) discharging method. The cut-off current of the CV phase during charging was set to 0.03 C. The cut-off charging and discharging voltages were set as per the manufacturer’s specifications (U_{up} = 2.75 V, U_{down} = 1.50 V). A rest time of 30 minutes was used between charging and discharging and vice versa.

For all cycling experiments with DoD < 100%, the cells were charged and discharged using 2.5 C and the CC method. There was no rest time between charging and discharging and vice versa. Here, the amount of charge moved was defined by the reference measurement's resulting Q and the respective DoD.

Coulombic efficiency (CE) measurements were performed using a charge and discharge C-rate of 0.05 C or 1 A using at - 5 °C, 25 °C and 45 °C. Once cell was cycled at each temperature.
Charging and discharging of the cells was performed using a highly accurate cell testing equipment (PEC, ACT0550 and SBT10050).

3.1.1.1 Understanding the cell behaviour

The voltage curve for discharge and charge is depicted in Figure 31. The curve, measured at 0.05 C to simulate OCV conditions, shows a hysteresis between charge and discharge voltages, which results from the different diffusion and charge transfer mechanisms taking place during charge and discharge.[2] Since LTO has flat charge and discharge voltage curves between states of charge between 95% and 5%, the decay in voltage during discharge, for most of the SoC spectrum (except SoC range 95–5%), reflects the response in potential of the NMC electrode only. The same holds true for the charge step.

The voltage curves also show a region where the voltage values are almost flat, called the "phase transition region" (see SoC range 70%–60%). While the phase transition is found between SoC 70% and 60% for the OCV curve, it can appear at higher or lower SoC ranges, depending on the outside temperature, self-heating and current rates chosen for the tests or during operation. The flat section of the voltage curve could also disappear depending on the same usage parameters.

The phase transitions during Li-ion insertion/extraction are highly relevant to the thermodynamics and kinetics of Li-ion batteries. These regions exhibit constant physical properties despite varying chemical composition. For example, during charge, the NMC electrode has (almost) the same voltage values even though its chemical composition varies due to increasing delithiation. During discharge, the voltage also remains approximately constant despite the increasing lithiation.

---

[2] Hou et al. « Li-Ion batteries: Phase transition », Chinese Physics B, Vol. 25, No. 1 (2016), https://www.researchgate.net/publication/291389406_Li-ion_batteries_Phase_transition

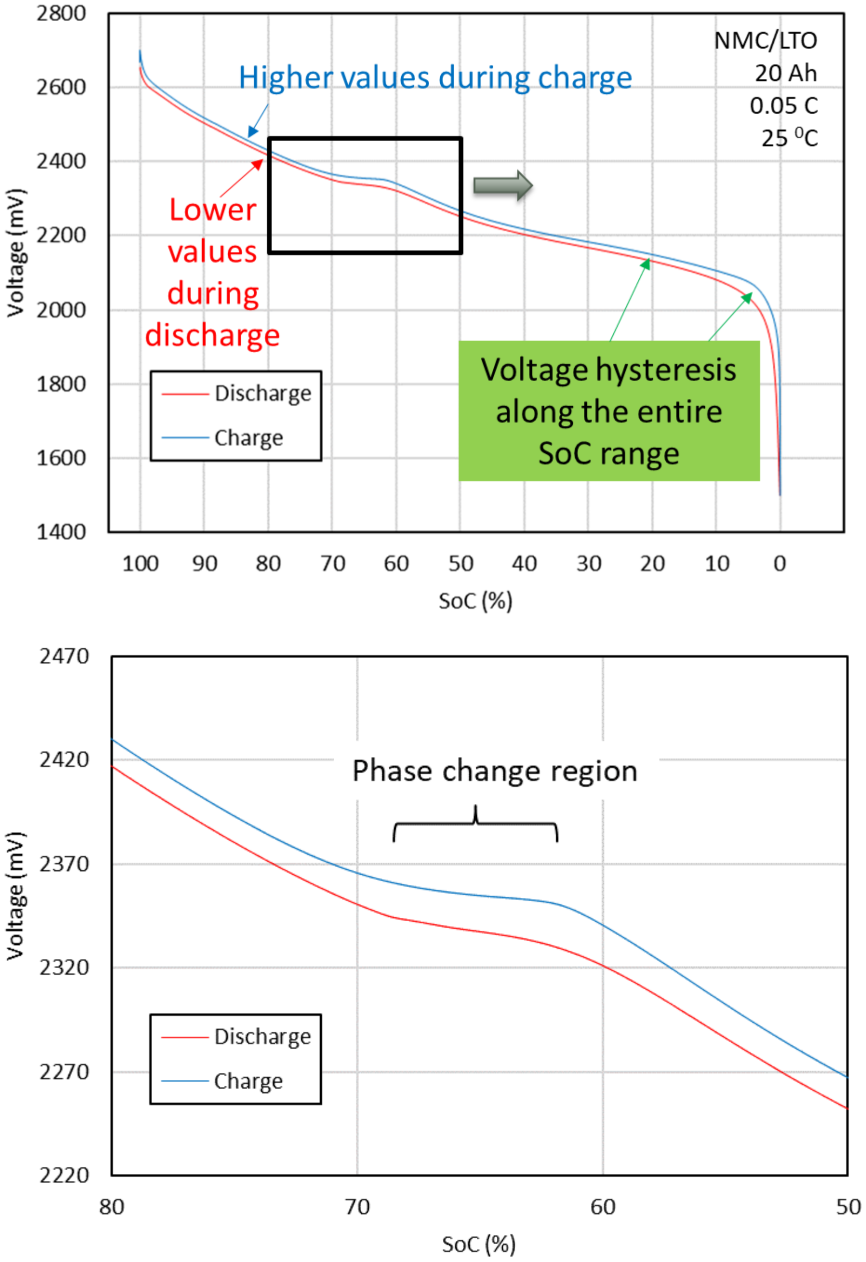

Figure 31: Phase change region: different chemical composition of electrode materials (varying Li-ion concentration in both electrodes), while maintaining almost same physical properties (potential)

The charge and discharge steps are accompanied by different, in theory opposite, thermodynamic processes. Figure 32 shows the charge and discharge of the batteries and the resulting voltage and thermal response from tests performed at C/3 and 2.5 C.

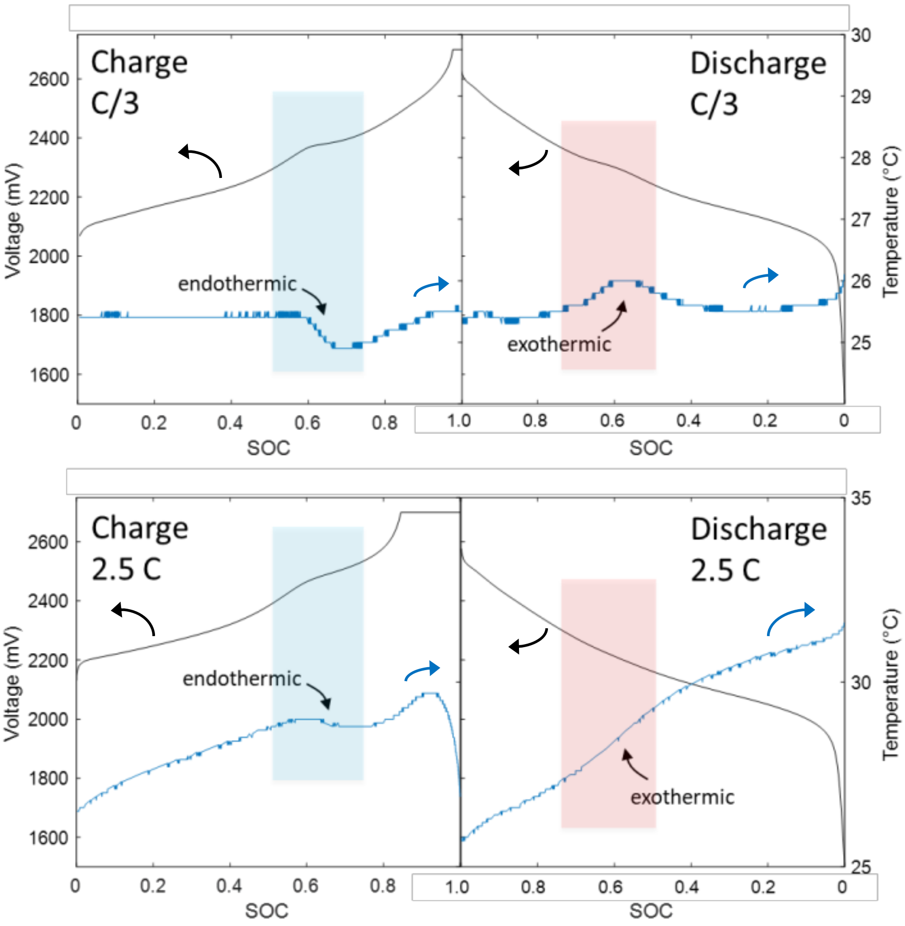

Figure 32: Charge and discharge voltage curves and resulting thermal behavior at C/3 and 2.5 C. These curves were recorded during the diagnostic cycles.

For the lower C-rate, the charge shows a clear endothermic thermal response while the discharge results in the opposite, exothermic thermal response. The thermal behavior variation on the surface of the cell occurs in the phase transition region described earlier in this report. For the higher C-rate, the endothermic behavior for the charge is less dominant. This is a result of the exothermic processes such as Joule’s heating caused by the higher C-rate. Still, the temperature drop during charge is still visible because of the endothermic nature of the charge. The discharge step is clearly exothermic.

3.1.2 Life Model and capacity degradation results

The goal of the life model is to predict the reachable number of charge/discharge cycles for the battery cells until the SOH drops below a certain level of for example 0.8 at given C-Rates, temperatures and DODs. These values are then used to calculate the number of drive cycles or roundtrips of the bus for a given SOC vs. time profile for a given route of the VBZ grid.

The starting point of the life model is the lab measurements, which show the normalized discharge energy vs. the number of cycles.

Figure 33 shows the normalized discharge energy for the different combinations of C-Rates and temperatures, which were used during the lab measurements.

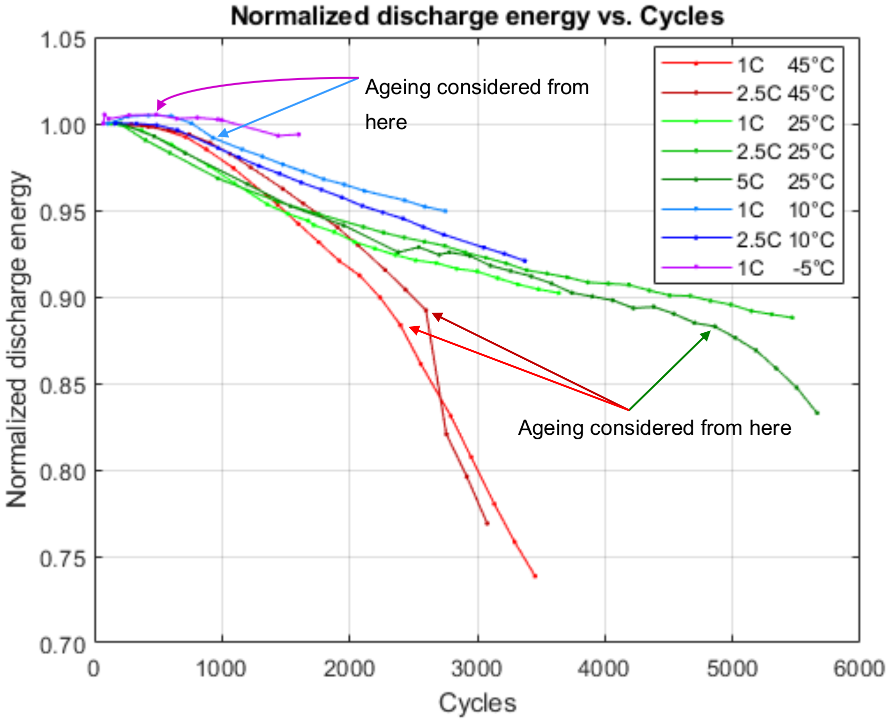

Figure 33. Normalized discharge Energy after a given number of cycles

The starting points, from where the ageing effects are considered, are marked with arrows for the different conditions. This approach serves two purposes. The first is that the ageing is accelerated beyond the knee point, which lies at around 88% SOH. This knee point can be well seen on the two curves at 45°C and on the one at 5C, 25°C. Beyond this point, the ageing accelerates drastically. Since this knee point is always above 80% SOH, which is usually the highest SOH where the battery is considered as not healthy enough for its purpose anymore. Therefore, only the ageing beyond the knee point is considered, where applicable. The second purpose is that especially at the lower temperature conditions, the SOH increases for approximately the first 500 cycles. Hence, the ageing is considered from the point where its effects look quite constant and steady. The affected curves are the one at -5°C and the one at 1C, 10°C. For the other curves, the ageing is considered to start from the beginning.

The following figures (Figure 34, Figure 35 and Figure 36) also show the normalized discharge energy for the DODs of less than 100%. Note that the x-axis no longer shows the number of cycles but the number of equivalent full cycles (EFC).

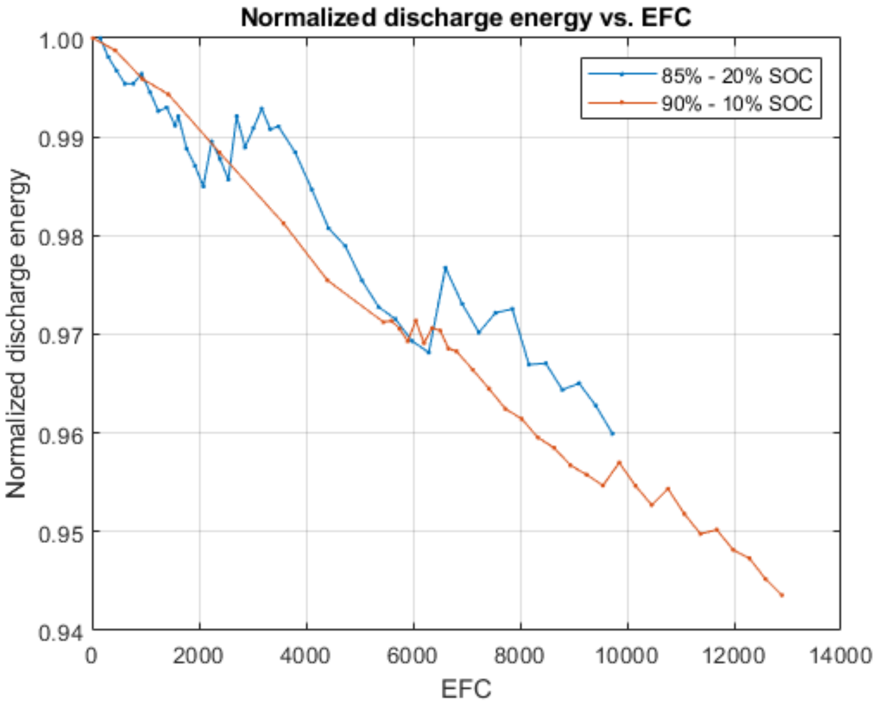

Figure 34. Normalized discharge energy for the 80% DOD and the 65% DOD cell

Both curves of 90% - 10% SOC and 85% - 20% SOC clearly show ageing effects. Hence, both curves are used for the life model. However, both curves seem to age similarly. Later in this document, Figure 40 shows the difference between the ageing effects clearer. The reason for the energy increases seen at around 2000 EFC and at around 6000 EFC of the 85% - 20% SOC curve could not be clearly explained. The same behavior is also seen in the following figures for the 20% DOD curves and for the 10% DOD curves. This artefact appears at 6000 EFC for almost every curve. Maybe the climate chamber has been opened or the cycling process underwent a longer unintended break and the cells were able to recover a bit.

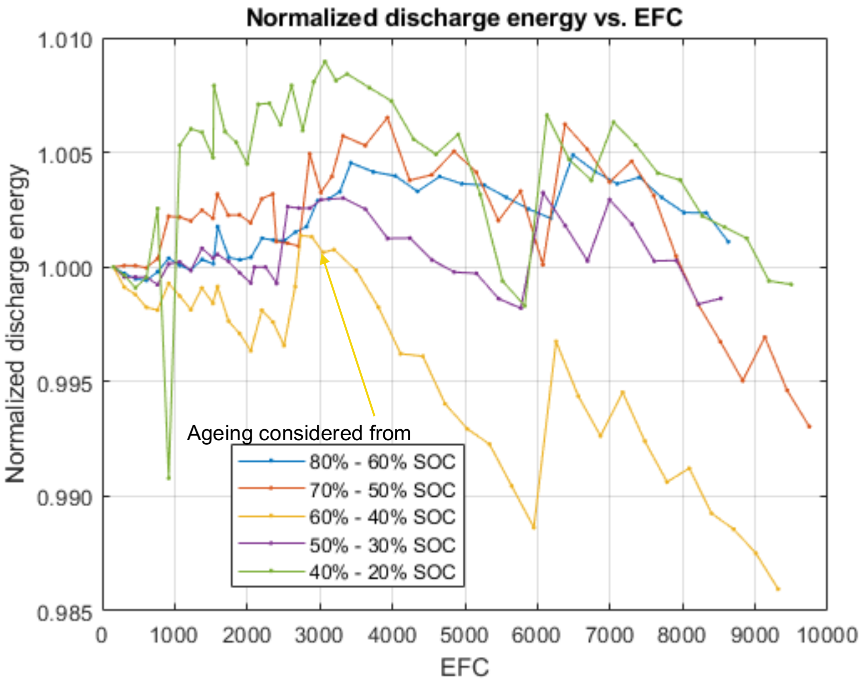

Figure 35. Normalized discharge energy for the 20% DOD cells

Only the curve of 60%– 40% SOC of Figure 35 was used for the life model, since its average SOC is 50%. It also shows the clearest discharge energy degradation, which also might just be a coincidence from the manufacturing process. Also, if one of the other curves was used, the number of reachable cycles in the final model would be excessively higher, which would then yield unrealistic results.

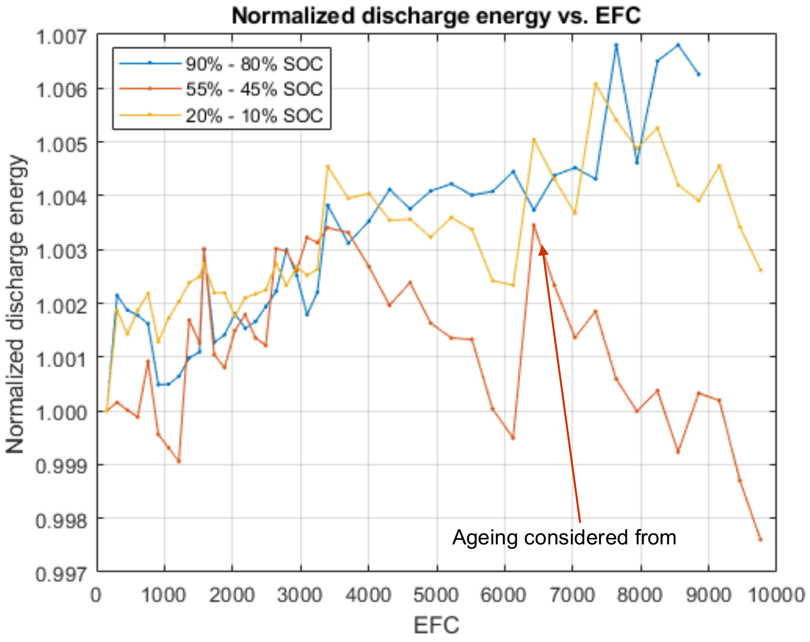

Figure 36. Normalized discharge energy for the 10% DOD cells

From Figure 36 only the curve of 55%– 45% SOC was used for the life model since it is the only one which shows a somewhat clear degradation of the discharge energy and since its average SOC is 50%.

3.1.2.1 Statistical derivation of the Life Model

The derivation of the Life Model contains statistical and stochastic means. The main assumption is that the SOH reduction per charge/discharge cycle does not always have the same (deterministic) effect but follows a certain probability density function with a mean value and a variance. In the following, X denotes the random variable which describes the SOH reduction per charge/discharge cycle. The expected value of X is denoted as m, the variance as σ^2.

$$m = E(X)$$
$$\sigma^2 = Var(X)$$

The exact probability density function of X is not known a priory and the parameters m and σ^2 have to be estimated from the lab measurements. The total SOH reduction after n cycles is denoted R_n and can be expressed as a sum as follows, where X_i is the SOH reduction of the i-th charge/discharge cycle.

$$R_n = \sum_{i=1}^{n} X_i$$

Since there are (far) more than 30 charge/discharge cycles between two reference measurements, R_n follows a gaussian probability density function with expected value $n \cdot m$ and variance $n \cdot \sigma^2$. This conclusion emerges from the central limit theorem, which states that a sum of independent and identically distributed random variables converges to the normal distribution. For n larger than 30, this approximation holds quite well.

Let Y_n be another random variable defined as

$Y_n = \frac{R_n}{n}$,

Where Y_n is a normally distributed random variable with expected value m and variance $\frac{\sigma^2}{n}$. is the variable Y_n can be gained from the lab measurements. It describes the mean SOH reduction per charge/discharge cycle between two reference measurements. The expected values of Y_n and X are the same. The variance of Y_n has to be calculated via the sample variance. Then, the variance of X can be calculated. The sample variance of Y_n can be calculated as follows, where N is the total number of available reference measurements:

$$\hat{V}_Y = \frac{1}{N-1} \sum_{n=1}^{N} (Y_n - m)^2$$

Since $\hat{V}_Y$ itself is also a random variable, it can be characterized by an expected value and a variance. In the following, the expected value is of interest, since it allows the calculation of σ^2. In the following equation the linearity property of the expected value and the fact that $Var(Y_n) = E((Y_n - m)^2) = \frac{\sigma^2}{n}$ was used.

$$E(V_Y) = E\left(\frac{1}{N-1} \sum_{n=1}^{N} (Y_n - m)^2\right) = \frac{1}{N-1} \sum_{n=1}^{N} E((Y_n - m)^2) = \frac{1}{N-1} \sum_{n=1}^{N} \frac{\sigma^2}{n} = \frac{\sigma^2}{N-1} \sum_{n=1}^{N} \frac{1}{n}$$

From this equation the variance of X, that is σ^2, can be calculated:

$$\sigma^2 = \frac{\hat{V}_Y \cdot (N-1)}{\sum_{n=1}^{N} \frac{1}{n}}$$

Now, both $E(X)$ and $Var(X)$ have been determined. The next step is the estimation of the number of charge/discharge cycles that can be reached until a minimal SOH of e.g. 0.8 is reached.

To achieve this estimation, the inverse gaussian distribution (also called inverse normal distribution or Wald distribution) comes into play. Descriptively explained, the normal distribution explains the distribution of a particle’s distance, which is subject to Brownian motion at a given time. The inverse gaussian distribution explains the distribution of the elapsed time for the particle to reach a given distance. Applied to our battery measurements, the normal distribution describes the SOH reduction for a given number of charge/discharge cycles and the inverse gaussian distribution describes the number of reachable cycles for a given minimal SOH.

The probability density function of the inverse gaussian distribution looks as follows:

$$IG(t;\mu,\lambda) = \sqrt{\frac{\lambda}{2\pi c^3}}\, e^{-\frac{\lambda(c-\mu)^2}{2\mu^2 c}}$$

Where μ is the expected value and λ is the shape parameter, which defines, together with μ, the shape of the curve and the variance. The variable t depicts the number of cycles for which the probability shall be calculated. μ and λ can be expressed by our estimated parameters m and σ^2. The following formulae apply:

$$\mu = \frac{1 - SOH_{min}}{m}$$

$$\lambda = \frac{(1 - SOH_{min})^2}{\sigma^2}$$

The following tables show the values for μ and λ for all the measurement series, which are used for the life model.

		Temperature			
	μ (SOH_{min} = 0.8)	-5°C	10°C	25°C	45°C
C-Rate	1.0 C	26'645	9'070	7'517	3'003
	2.5 C	-	7'757	10'466	2'936
	5.0 C	-	-	6'181	-

It can be clearly seen that a higher temperature leads to a lower expected value for the number of achievable cycles. The same also holds for higher C-Rates, whereas the effect is not as distinct as for the temperature. The only exception is the value at 2.5C, 25°C temperature. This value is clearly higher than its neighbors at the lower C-Rate and the lower temperature. It seems that the used cell is by chance stronger than the other cells, which might be due to production process uncertainties. It was decided to ignore this value for the further development of the life model.

	μ (SOH_{min} = 0.8)	Cycles	FCE
SOC Range	90-10	65'871	52'697
	85-20	85'513	55'583
	60-40	449'223	89'845
	55-45	1'220'540	122'054

It can be seen that a lower DOD increases the expected values drastically. This applies to the number of cycles, as well as to the FCE. Also note that the slight limitation of the SOC to 10%–90% increases the number of cycles by a factor of at least 6 compared to the full cycles from the previous table.

		Temperature			
	λ (SOH$_{min}$ = 0.8)	-5°C	10°C	25°C	45°C
C-Rate	1C	4'635'700	10'558'000	1'608'300	426'920
	2.5C	-	17'402'000	2'254'900	2'900
	5C	-	-	128'270	-

	λ (SOH$_{min}$ = 0.8)	Cycles	FCE
SOC Range	90-10	6'143'900	4'915'120
	85-20	1'836'600	1'193'790
	60-40	15'378'000	3'075'600
	55-45	187'810'000	18'781'000

The probability density function of the inverse gaussian distribution tells us at which probability a certain number of cycles t can be reached. This can be used to calculate the probability that a certain number of cycles can *at least* be reached, denoted as T. This probability is called reliability and is calculated in the following way:

$$\text{reliability} = \text{Prob}(t \geq T) = \int_{T}^{\infty} IG(t;\mu,\lambda)\,dt = \Phi\left(\sqrt{\frac{\lambda}{T}}\left(1-\frac{T}{\mu}\right)\right) - e^{\frac{2\lambda}{\mu}} * \Phi\left(-\sqrt{\frac{\lambda}{T}}\left(1+\frac{T}{\mu}\right)\right)$$

with

$$\Phi(\mathrm{t}) = \int_{-\infty}^{t} \frac{1}{\sqrt{2\pi}} e^{-\frac{x^2}{2}}\,dx = \frac{1}{2}\left(1+\operatorname{erf}\left(\frac{t}{\sqrt{2}}\right)\right)$$

being the cumulative distribution function of the standard normal distribution with expected value zero and variance one, which can also be expressed by the so-called error function $\operatorname{erf}(x)$.

The reliability function allows us now to calculate the number of cycles, which can at least be reached by a given probability. If the desired probability is set to e.g. 0.95, the calculated number of cycles T can at least be reached by a probability of 95%. The 95% values are given in the following tables.

		Temperature			
	T (95% value)	-5°C	10°C	25°C	45°C
C-Rate	1C	23'604	8'707	6'737	2'967
	2.5C	-	7'540	9'387	2'791
	5C	-	-	5'978	-

	T (95% value)	Cycles	FCE
SOC Range	90-10	55'561	44'449
	85-20	60'081	39'053
	60-40	343'933	68'787
	55-45	1'080'537	108'054

The following figures show the probability density functions for the full cycles at different temperatures and for the shallow cycles. The figures summarize the given tables and illustrate the data from the tables.

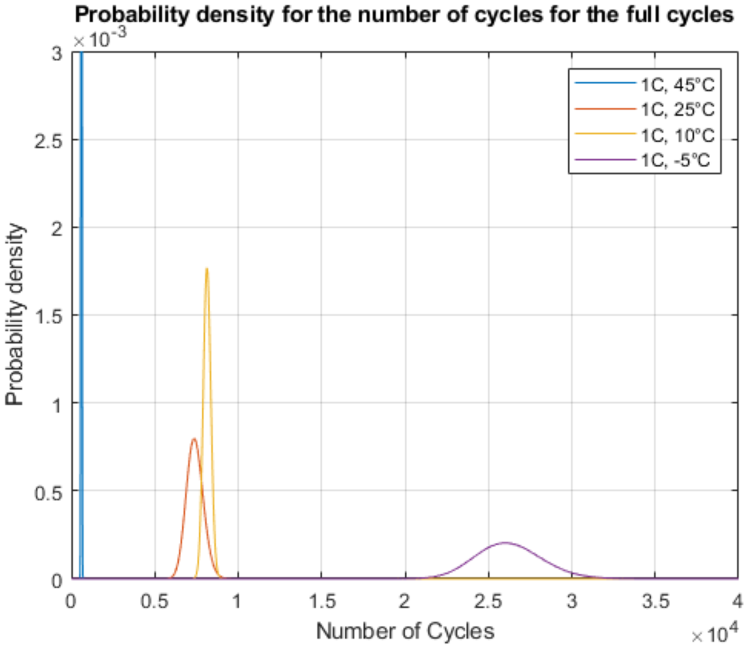

Figure 37. Probability density functions of the reachable number of cycles at different temperatures

Figure 37 clearly shows that lower temperatures lead to a higher number of cycles. It is also seen that the difference between 10°C and 25°C is not that big. However, cooler temperatures lead to much more cycles and hotter temperatures lead to much fewer cycles.

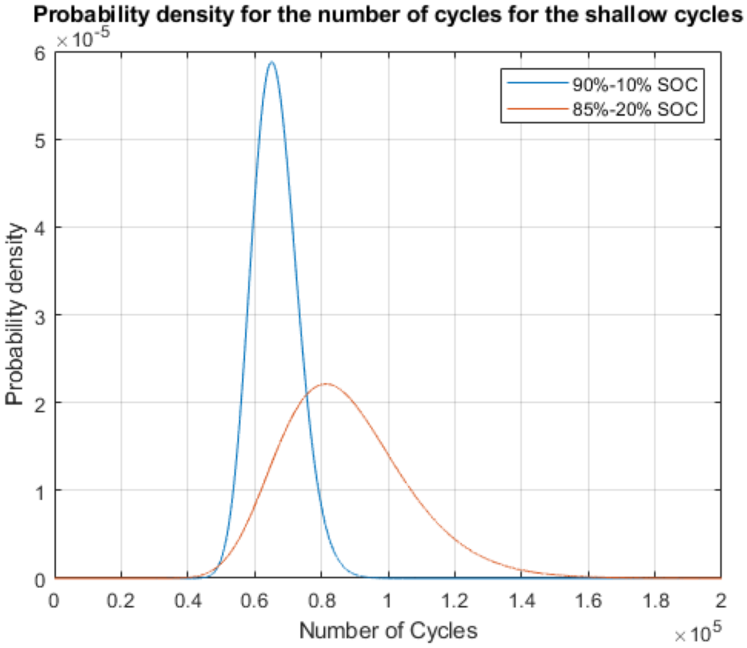

Figure 38. Probability density functions for the 80% DOD and the 65% DOD cells

Figure 38 shows the overlapping of the reachable number of cycles for any given reliability. It can be seen that the expected value (peak of the curve) of the 85%–20% SOC curve is higher than for the other curve, but the number of cycles for a reliability of 95% are almost the same for both curves.

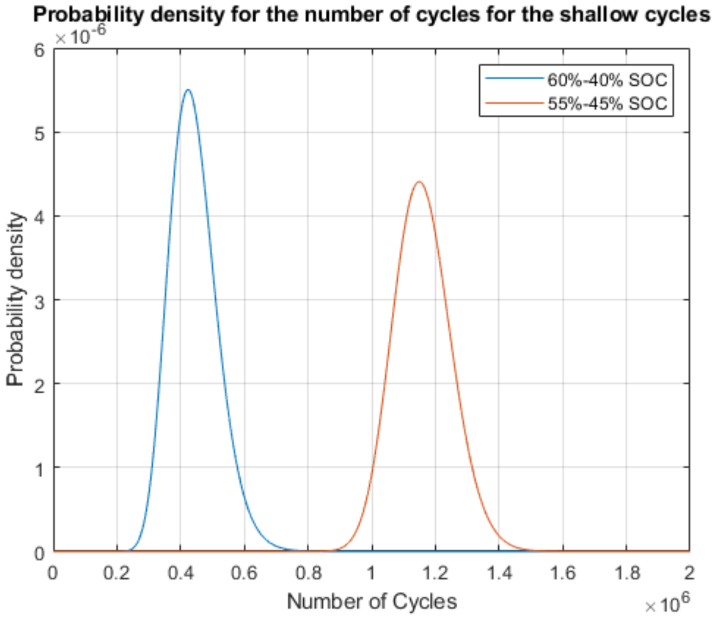

Figure 39. Probability density functions for the 20% DOD and the 10% DOD cells

The following figure shows a comparison of the reachable FEC for the different DODs, which were tested. For each DOD, the range for a reliability of 95% to 5% is shown.

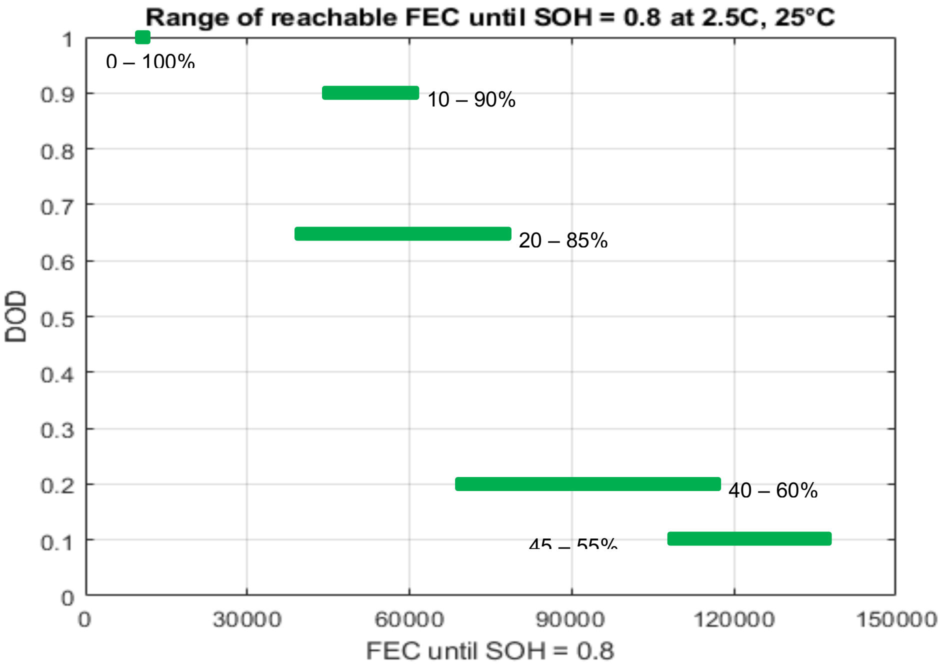

Figure 40. Range of the number of FEC for different DODs

Figure 40 shows the ranges of the achievable cycles. The green bars show the 5% to 95% ranges of the achievable number of FEC. As already seen beforehand in the figures and tables, a lower DOD leads to a higher number of FEC and the bar for the 20%– 85% SOC cell completely overlaps with the 10%– 90% SOC cell.

In the following, for the further development of the life model, only the 95% values (left end of the green bars in Figure 40) are used.

3.1.2.2 Dependency of the number of cycles from the DOD

The next step is to develop a model, which describes the number of cycles for different DODs, whereas the other environmental conditions (C-Rate and Temperature) do not change. The following figure shows the reachable number of cycles for the different DODs, all at 2.5C and 25°C ambient temperature as orange data points. The blue curve is fitted through the data points with the following rational function:

$$DOD = \frac{p}{Cycles + q}$$

In the fitting process, the values for p and q are determined such that the curve passes through the data points ideally in the sense of least square residuals.

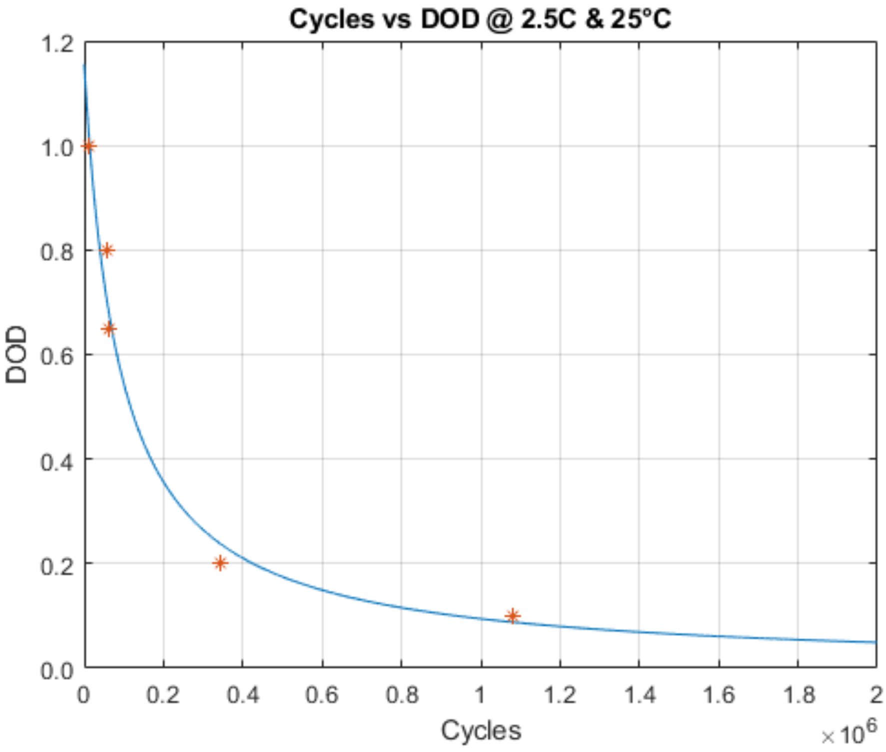

Figure 41. Dependency of the reachable number of cycles from the DOD

As seen, the curve fits very well through the data points. This kind of fitting is repeated for any other available combination of C-Rates and temperatures, for which useful data is available. Since the shallow cycle measurements were only conducted at 2.5C C-Rate and 25°C temperature, the reachable number of shallow cycles for other conditions have to be gained from the ones at 2.5C C-Rate and 25°C temperature. It is assumed that the ratio between the reachable number of full cycles and the number of shallow cycles for any other conditions is the same as for the reference conditions of 2.5C C-Rate and 25°C temperature.

$$\left(\frac{\text{number of full cycles}}{\text{number of shallow cycles}}\right)_{\text{any other condition}} = \left(\frac{\text{number of full cycles}}{\text{number of shallow cycles}}\right)_{2.5\text{C},25^\circ\text{C}}$$

With this assumption, artificial measurements for shallow cycles can be created to calculate the parameters p and q for any other conditions. So, p and q each become a function of the C-Rate and the temperature. For this curve at 2.5C C-Rate and 25°C temperature, p equals 102’950 and q equals 89’096.

This leads again to a fitting procedure where p and q have to be fitted from the available data points in the sense of least square residuals. The following figure shows the data points as blue dots and the three-dimensional surface through these points. As seen, p is always larger than q for all conditions.

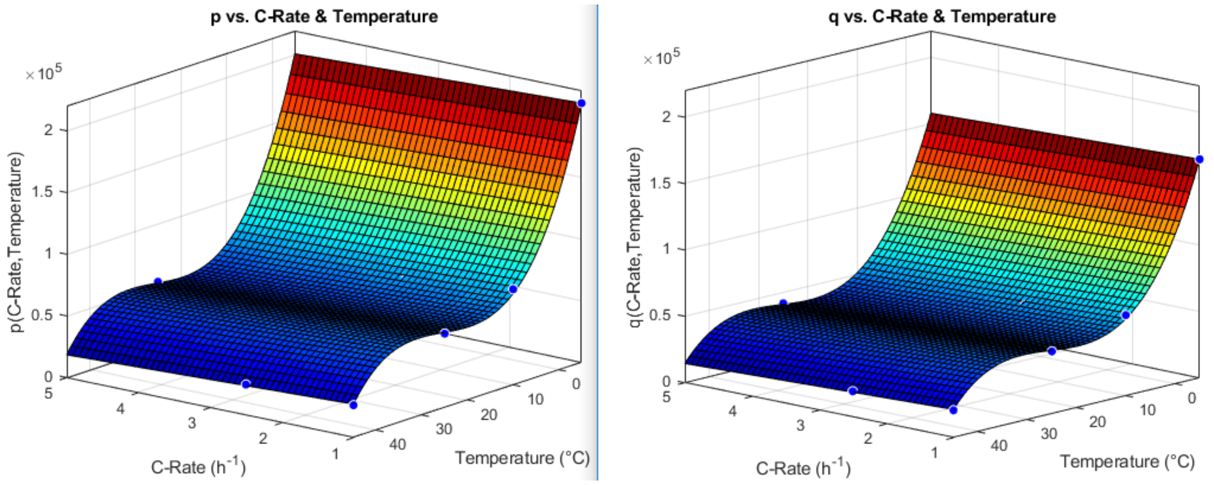

Figure 42. Fitted 3D curve for the parameters p and q

A well-fitting model was found in a polynomial model, where the C-Rate appears linearly and the temperature up to its third power.

$$\begin{cases} p(C\text{-}Rate, Temperature) = p_{00} + p_{10} * C\text{-}Rate + \sum_{n=1}^{3} p_{0n} * Temperature^{n} \\ q(C\text{-}Rate, Temperature) = q_{00} + q_{10} * C\text{-}Rate + \sum_{n=1}^{3} q_{0n} * Temperature^{n} \end{cases}$$

Now, the complete model for the reachable number of cycles as a function of the C-Rate, the temperature and the DOD and can be assembled from p and q.

$$\text{Cycles}(C\text{-}Rate, Temperature, DOD) = \frac{p(C\text{-}Rate, Temperature)}{DOD} - q(C\text{-}Rate, Temperature)$$

This model can also be used to calculate the equivalent full cycles.

$$EFC(C\text{-}Rate, Temperature, DOD) = Cycles * DOD = p(C\text{-}Rate, Temperature) - q(C\text{-}Rate, Temperature) * DOD$$

The following figure shows the number of reachable cycles with a fixed DOD of 1. As seen, the temperature dependence is much more of a decisive factor for the reachable number of cycles than the temperature.

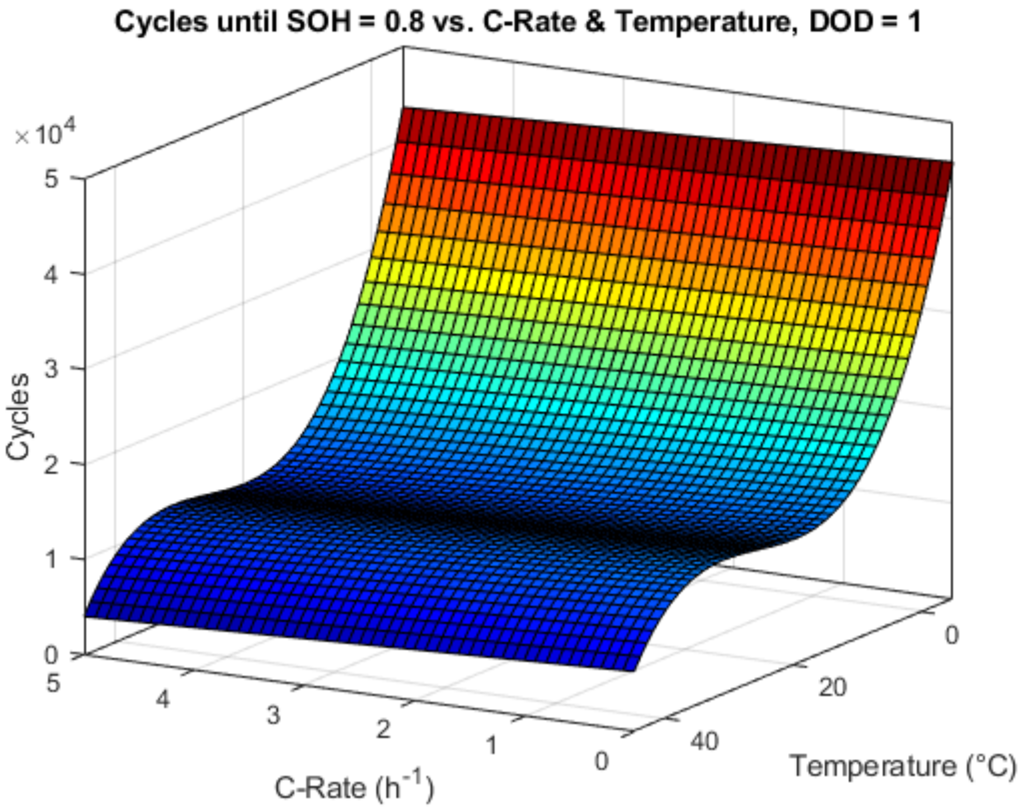

Figure 43. Final model for the number of cycles for given conditions

Other curves with the DOD as independent variable are available in the appendix of this report.

3.1.2.3 Other models; Energy throughput vs. C-Rate & Temperature, Exposure time vs. C-Rate & Temperature

As seen, the DOD vs. number of cycles follows a rational function $DOD = \frac{p}{Cycles+q}$.

DOD vs. Energy throughput and DOD vs. Exposure time both follow an exponential function:

$DOD = a_E * e^{b_E * \text{Energy throughput}}$ and $DOD = a_t * e^{b_t * \text{Exposure time}}$, respectively. This is shown in the following figure for the example of 2.5C, 25°C. the energy throughput is given in [kWh] and the exposure time in [h].

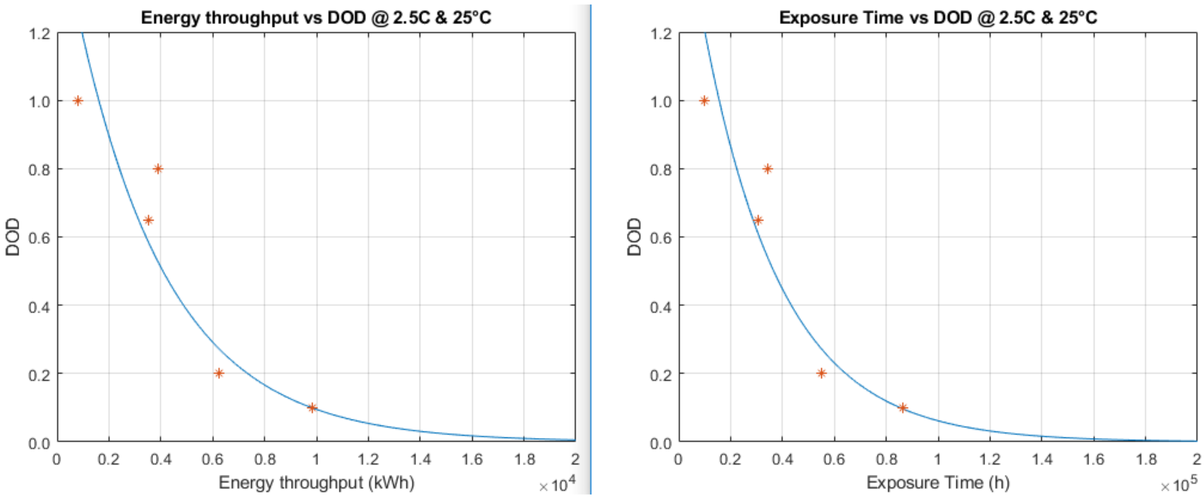

Figure 44. Reachable energy throughput (left) and exposure time (right) for different DODs

a_E and a_t are constant values and b_t and b_E depend on the C-Rate and the temperature, similarly to p and q from the previous chapter. a_E equals 1.738 and a_t equals 1.912. A good fit for b_E is a polynomial of first order in the C-Rate and of third order in the temperature, similar to the polynomials for p and q, is used. For b_t a full polynomial function with terms of up to first order in the C-Rate and of up to third order in the temperature is used.

$$\begin{cases} a_E = 1.738 \\ b_E(C\text{-}Rate, Temperature) = b_{E_{10}} * C\text{-}Rate + \sum_{n=0}^{3} b_{E_{0n}} * Temperature^n \end{cases}$$

and

$$\begin{cases} a_t = 1.912 \\ b_t(C\text{-}Rate, Temperature) = \sum_{n=0}^{1} \sum_{m=0}^{3-n} b_{t_{nm}} * C\text{-}Rate^n * Temperature^m \end{cases}$$

The complete models for the energy throughput and the exposure time are:

$$\text{Energy throughput}(C\text{-}Rate, Temperature, DOD) = \frac{\ln\left(\frac{DOD}{a_E}\right)}{b_E(C\text{-}Rate, Temperature)}$$

$$\text{Exposure time}(C\text{-}Rate, Temperature, DOD) = \frac{\ln\left(\frac{DOD}{a_t}\right)}{b_t(C\text{-}Rate, Temperature)}$$

The following figure shows 3D curves for the energy throughput and the exposure time for a fixed DOD of 1. There are also other curves available in the appendix.

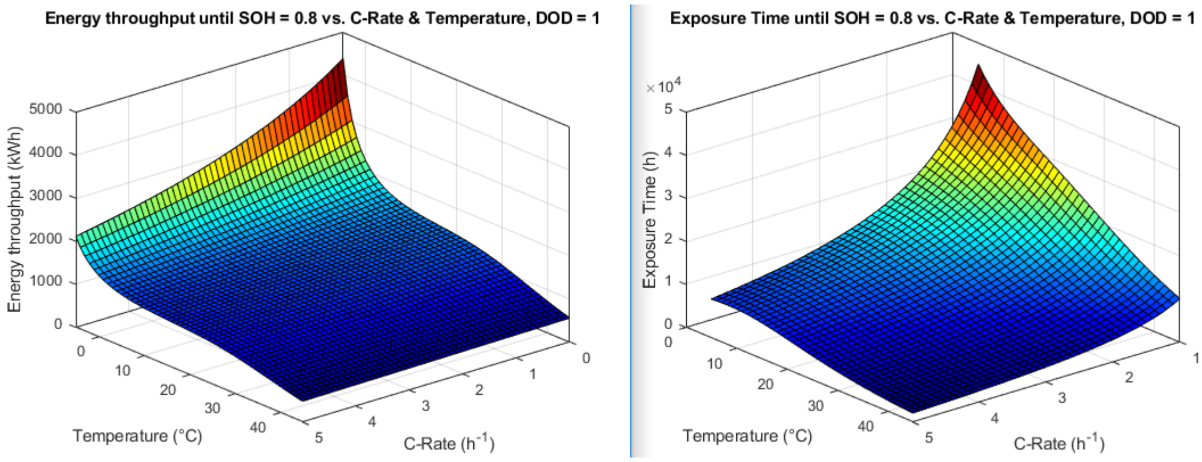

Figure 45. Final model for the energy throughput and the exposure time for given conditions

Further analysis of the cells’ behavior can be found in the attachment of this report.

3.1.2.4 Analysis of a given SOC profile from the bus

This chapter is about the analysis of a given SOC profile of the bus during operation on the lines of the VBZ grid. The SOC profile analysis is used to extract closed subcycles from a given SOC profile, where the DOD and the C-Rate of these subcycles are simultaneously calculated. The algorithm, which does this extraction is called the rainflow counting method or rainflow algorithm. This method was originally used in fatigue analysis for mechanical systems like steel beams, which are stressed with repetitive patterns. A rather complicated stress cycle can be split into several simple stress cycles, which result in the same total fatigue symptoms. Applied to our life model, the extracted subcycles are charge/discharge cycles with a given DOD and C-Rate. With the models from the previous chapter, for each extracted subcycle the contribution to the ageing of the battery and finally the total ageing effect of the given SOC profile can be computed.

The following simple example shall clarify the principle of the rainflow algorithm. Consider the following load profile depicted in the following figure. The x-axis is the time and the y-axis could be some force or pressure on a beam. The algorithm considers four consecutive points (labelled 1 to 4 in Figure 46). If the maximal value of the two inner points (points 2 and 3) is lower than the maximum of the outer points (points 1 and 4) and if at the same time the minimal value of the inner points is higher than the minimum of the outer points, the inner two points form a closed embedded subcycle (blue dashed line, which goes from point 2 to point 3 and back to the y-value of point 2). If there are no more (remaining) closed subcycles to extract, the remaining profile is approximated by half subcycles (green dashed lines).

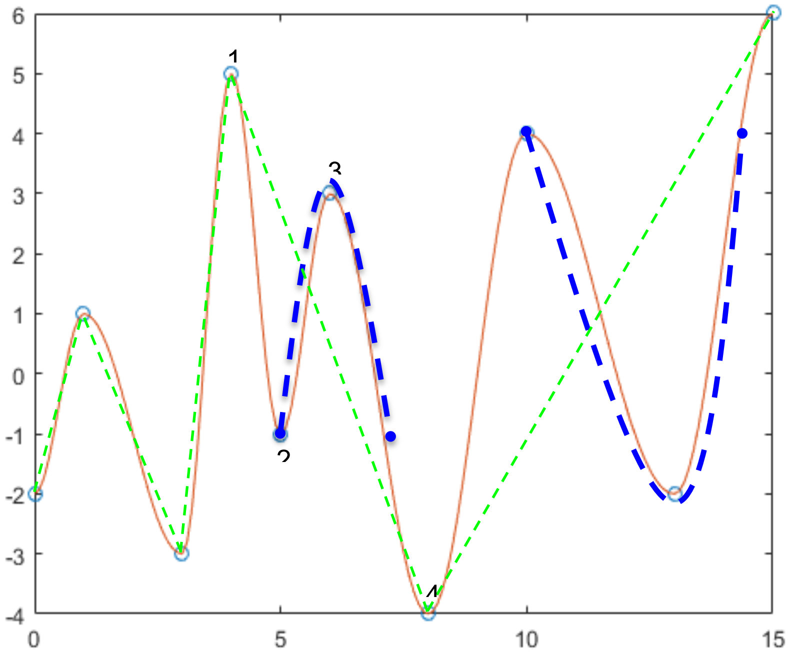

Figure 46. Idea of the rainflow algorithm

The number of achievable drive profiles can then be calculated as following:

$$\text{Number of drive profiles} = \frac{1}{\sum \frac{1}{\text{number of charge/discharge cycles for each exctracted subcycle}}}$$

The number of charge/discharge cycles for each extracted subcycle is calculated by the final formula of the last chapter:

$$\text{Cycles}(C\text{-}Rate, Temperature, DOD) = \frac{p(C\text{-}Rate, Temperature)}{DOD} - q(C\text{-}Rate, Temperature)$$

The reciprocal value of this number is the ageing contribution of one such subcycle. The ageing contributions of all subcycles are added up and again the reciprocal value is calculated, which then equals the number of drive profiles for the given SOC profile.

As a realistic example, Figure 47 shows the extracted subcycles for the VBZ route 46. The bus driving profile was converted in terms of battery SOC vs. time, dotted blue line in Figure 47. By applying the algorithm to this profile, several subcycles (at different SOC ranges and with different DoDs and Crates) are extracted and indicated by the colorful straight lines. The colors have no other meaning than to provide good visibility of the different overlapping subcycles.

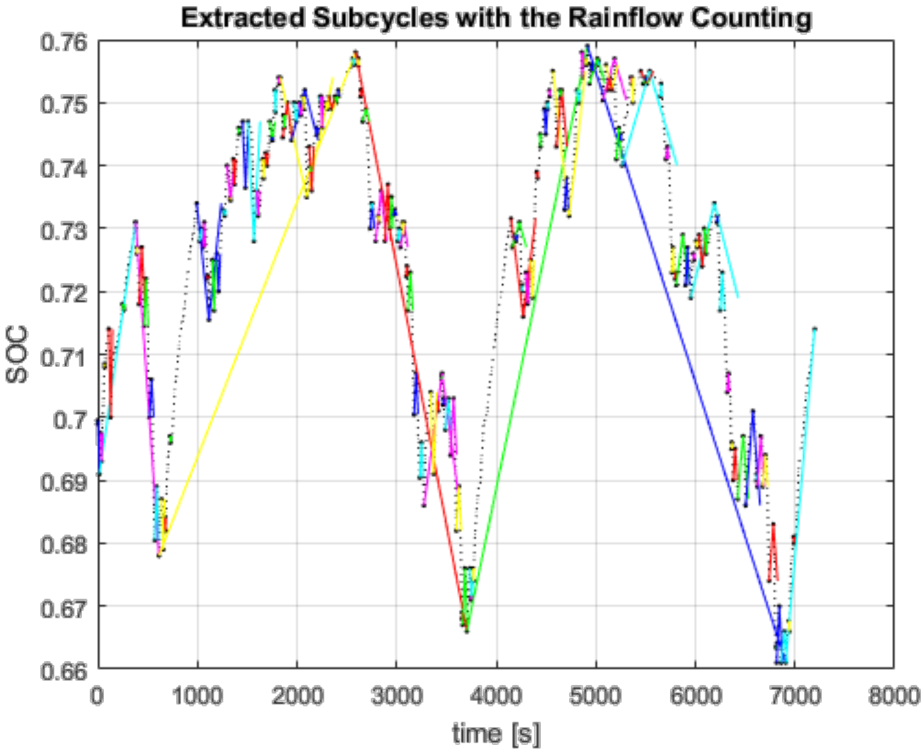

Figure 47. SOC profile for route 46 with extracted subcycles by the rainflow algorithm

3.2 Results and discussion

3.2.1 Voltage-Capacity-Temperature behaviour during cycling

3.2.1.1 Coulombic efficiency test results

Capacity loss in Li-ion batteries is the result of parasitic reactions which consume active components of the cell. CE analysis captures the rate of Li-ion i.e. charge loss per cycle and time unit during the charging and discharging phases.

CE values between 1.0000 and 0.9995 are perfectly normal. Therefore, the measurement equipment must be highly precise to capture any differences between them. When measured precisely, the time required for lifetime analysis is significantly reduced. As a rule of thumb, the closer the CE-values are to the ideal value of 1.0000, the longer the lifespan expectancy. Lifetime expectancy can be estimated with the use of a linear slope based on the assumption that the capacity degradation is linear until a specific SoH-level. We calculated the slopes of the capacity decay observed in Figure 48 for all three temperatures. The results are listed in Table 4.

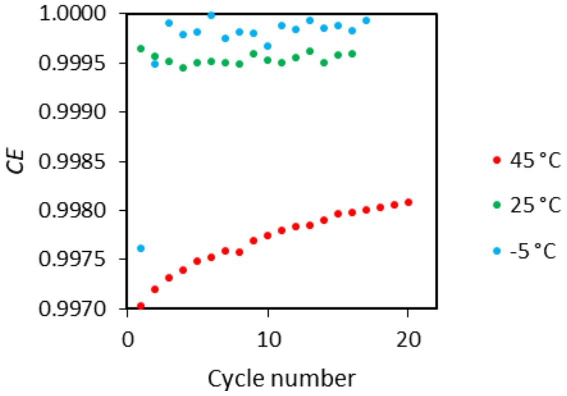

Figure 48. Coulombic efficiency results at three temperatures

Table 4. Analysis of the CE-results using a linear slope for Qc-decay

Temperature	- 5 °C	25 °C	45 °C
Qc-loss / cycle	0.011%	0.043%	0.15%
Number of 0.05 C cycles until SoH = 80%	1’946	520	149
Time until SoH = 80%	77’846 hours 3’243 days 8 years 10 months	20’805 hours 867 days 2 years 6 months	5’946 hours 248 days 9 months

Figure 48 suggests that the lifetime is maximized when the battery is cycled at low temperatures, including -5 °C. While it is well known that 25 °C is preferred over 45 °C for lifespan extension, the fact that -5 °C shall be better than 25 °C is contradictory to aging behavior found in conventional graphite-based lithium-ion batteries, where aging is promoted at low temperatures (especially temperatures lower than 10 °C). However, the cells subjected to the experiment are NMC/LTO and do not have graphite electrodes. The effect of temperature seems to be different on NMC/LTO cells.

The results from the CE-analysis demonstrate however that at very low C-rates lifespan expectancy increases with lower temperatures. Since the C-rate is very low, it is logical to assume that the same behavior is to be expected for calendric aging. Here, it is well known that low (storage) temperatures hinder parasitic reactions that lead to capacity degradation during storage, also in graphite-based lithium-ion batteries.

Figure 49 depicts a simplified model of the expected slope trend in the temperature region in question for Lithium-ion batteries containing graphite-based negative electrodes. Aging is expected to increase exponentially for higher and lower temperatures than 25 °C. Optimal temperature conditions are expected to be found between 15 °C and 25 °C and not in the low temperature regions. Therefore, our results might be a novel finding for cells containing LTO on the negative electrode. Only further cycling at -5 °C will reveal whether Figure 49 is also valid for our NMC/LTO cell.

According to our experience and through literature surveys, it would be a big surprise if any conventional graphite-based cell still had more than 90% of the initial capacity Q_n after being exposed to thousands of cycles under the experimental conditions in this experimental Phase 2. Usually, conventional cylindrical 18650 cells reach 80% of Q_n, i.e., the end of life of the battery, after only approximately 500 to 600 cycles when charging and discharging at approximately 1.0 C to 2.0 C.

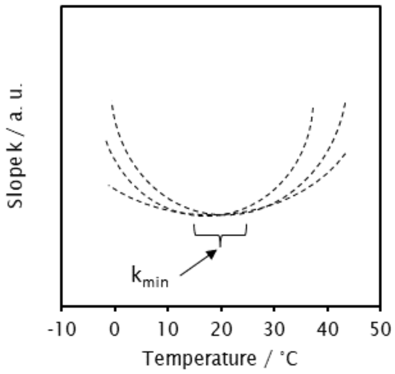

Figure 49: Simplified model of the expected slope behavior for graphite-based cells according to literature. The optimal usage parameter temperature is represented by the slope k_{min}.

3.2.1.2 Behavior during cycling for DoD = 100%

Figure 50 to Figure 57 show increasing temperatures on the surface of the samples with increasing cycle numbers. Exception to this trend is seen for the battery tested at 1.0 C at 45 °C only, probably resulting from a weak contact between the temperature sensor and the surface of the cell. The sudden temperature jumps for the tests at 10 °C may either be the result of a lose contact between temperature sensor and sample or an imperfect repositioning of the cells inside the chamber after EIS measurements.

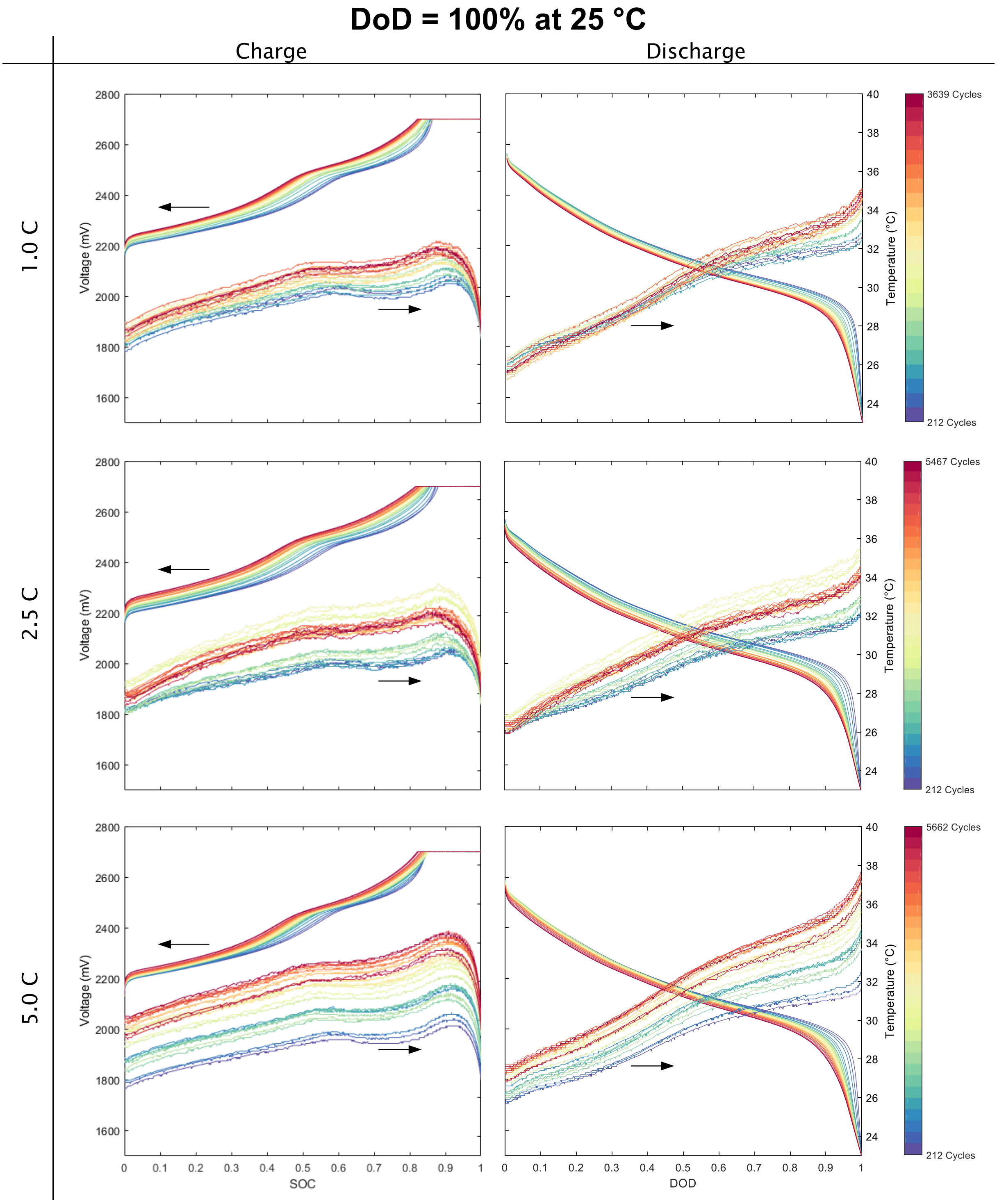

Figure 50: Voltage and temperature profile for tests performed at 25 °C and 1.0 C (top), 2.5 C (middle), and 5.0 C (bottom). The DoD for these experiments was 100%.

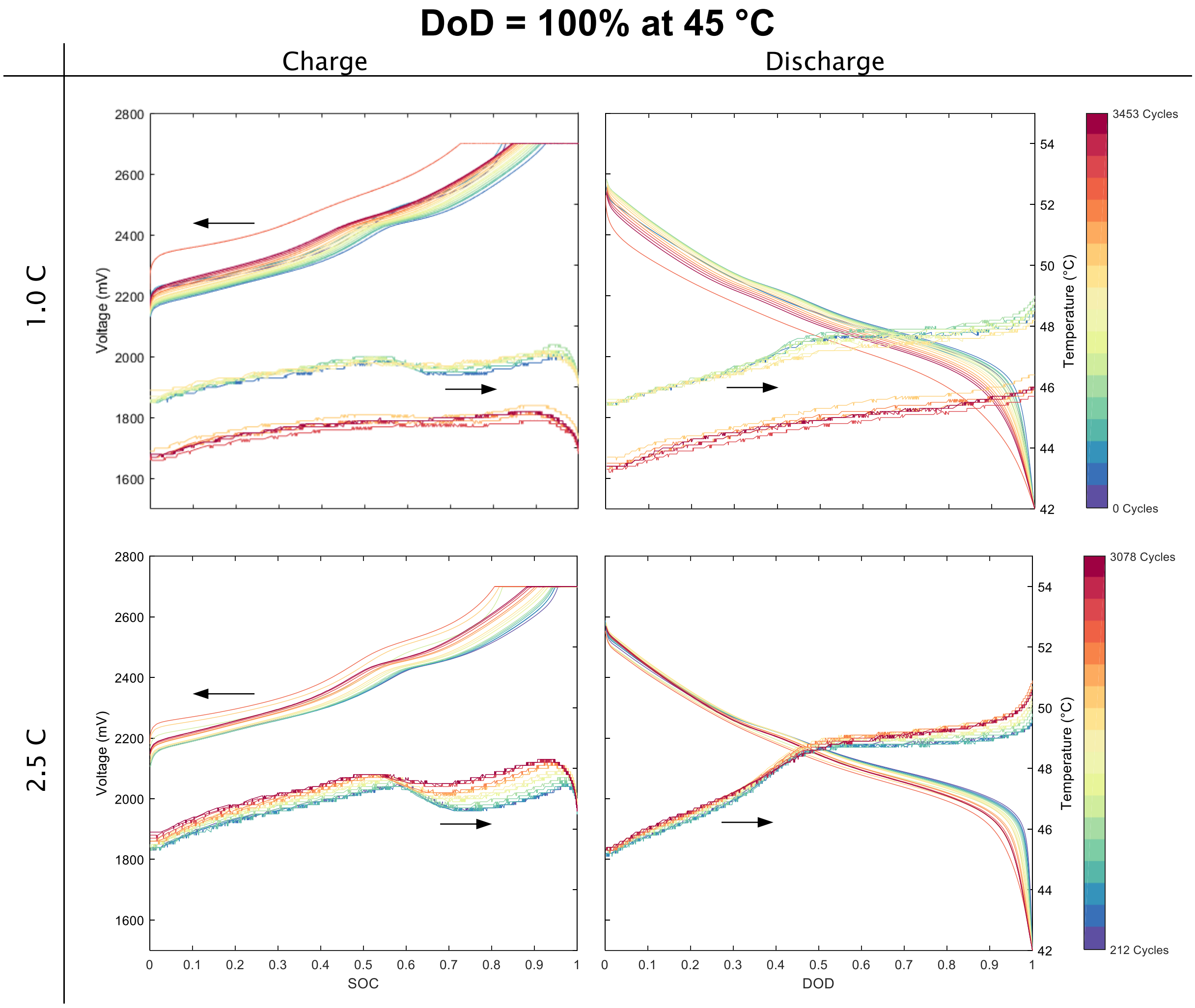

Figure 51: Voltage and temperature profile for tests performed at 25 °C and 1.0 C (top), 2.5 C (middle), and 5.0 C (bottom). The DoD for these experiments was 100%.

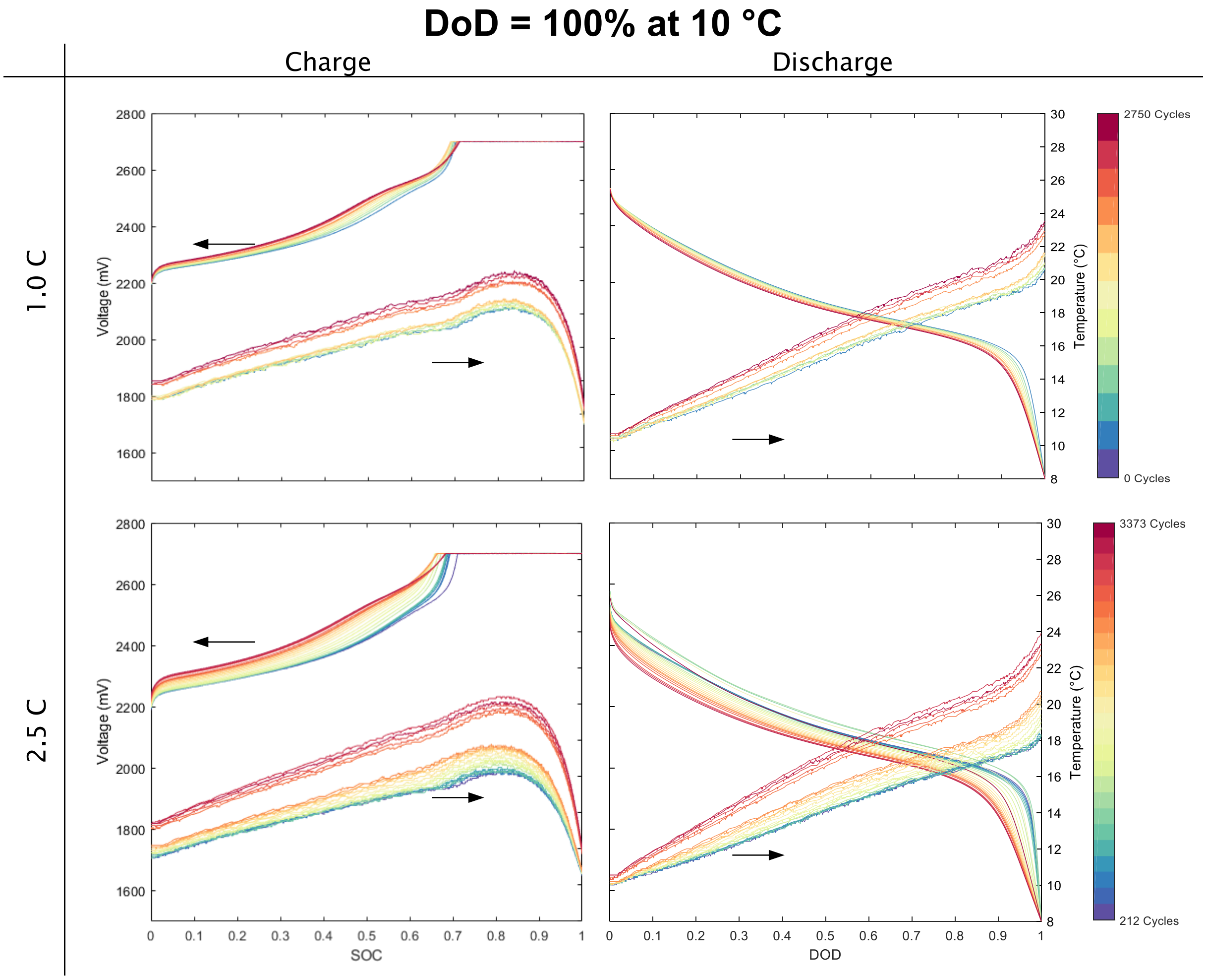

Figure 52: Voltage and temperature profile for tests performed at 25 °C and 1.0 C (top), 2.5 C (middle), and 5.0 C (bottom). The DoD for these experiments was 100%.

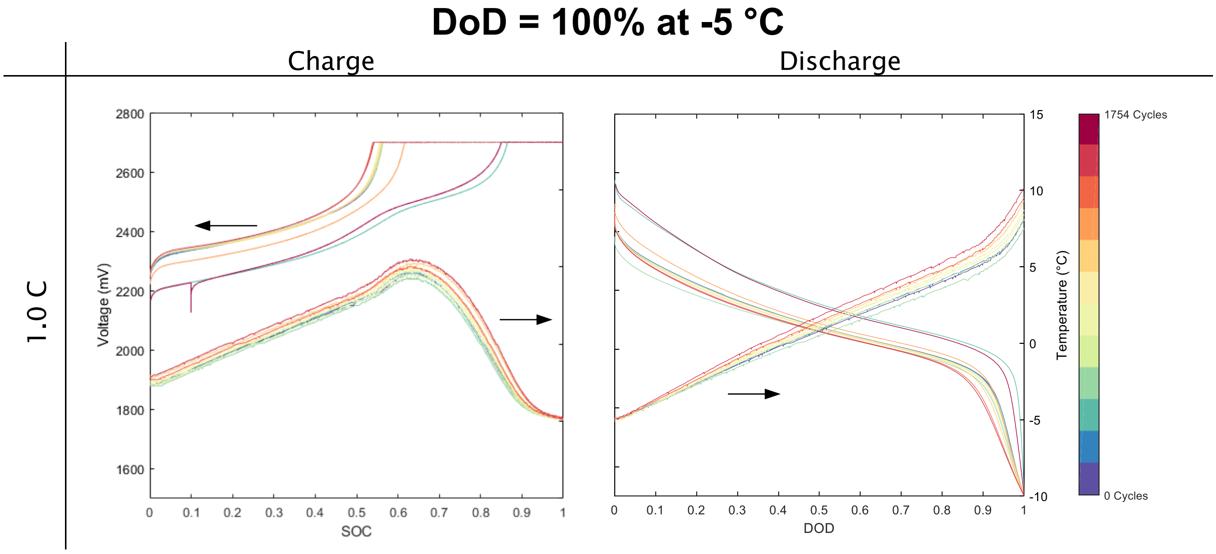

Figure 53: Voltage and temperature profile for tests performed at 25 °C and 1.0 C (top), 2.5 C (middle), and 5.0 C (bottom). The DoD for these experiments was 100%.

3.2.1.3 Behavior during cycling for DoD < 100%

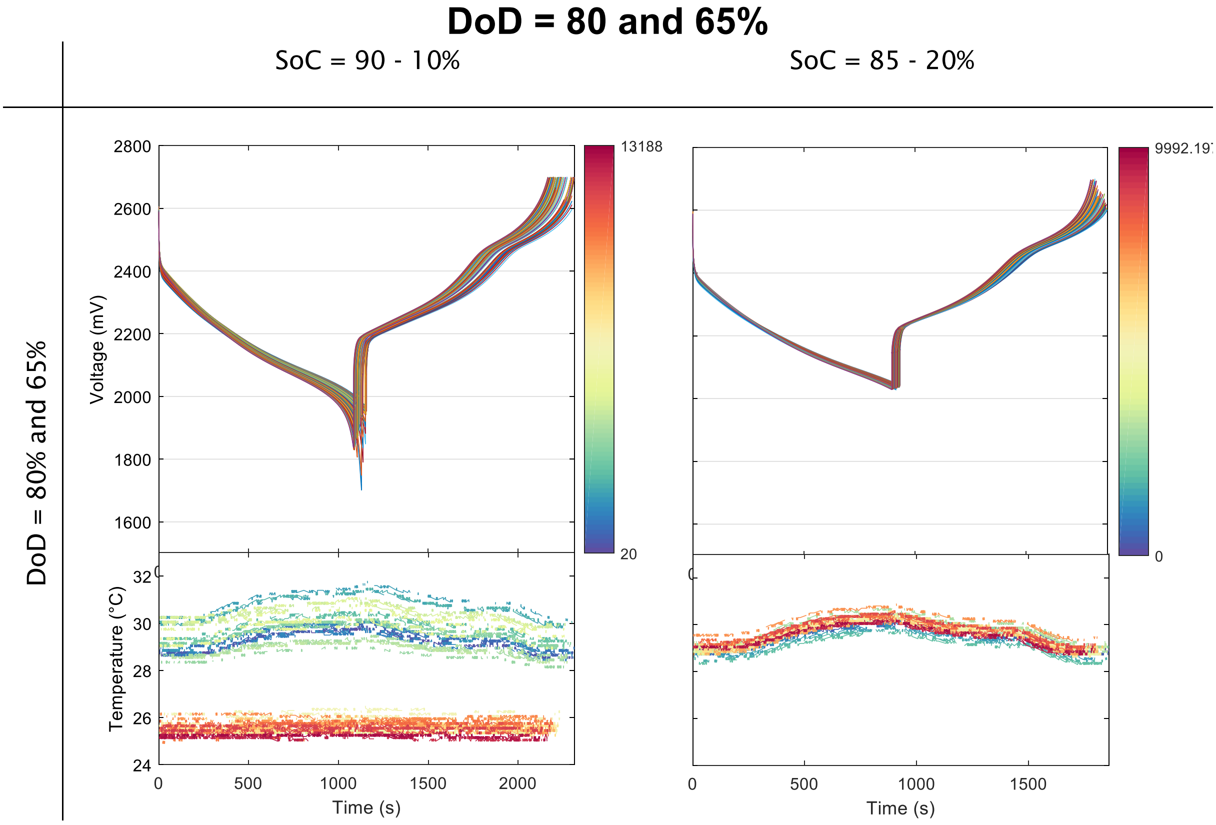

Figure 54: Evolution of voltage and temperature during cycling within a DoD of 80 and 65%. For DoD = 80%, overvoltages caused the upper voltage limit to be reached before SoC 90%. For DoD = 65%, the upper voltage limit was only reached for a smaller amount of cycles.

For both DoD 80% and DoD 65%, U_{max} = 2.7 V was reached in almost all and some of the cycles because of the presence of polarization resistance, respectively. This means, while the cell was discharged with a Q corresponding to DoD of 80% and 65%, respectively, they were no able to move the same amount of Q during the charge because the sub-cycle stopped once U_{max} was reached.

This effect was not seen for the other experiments with DoD < 100%.

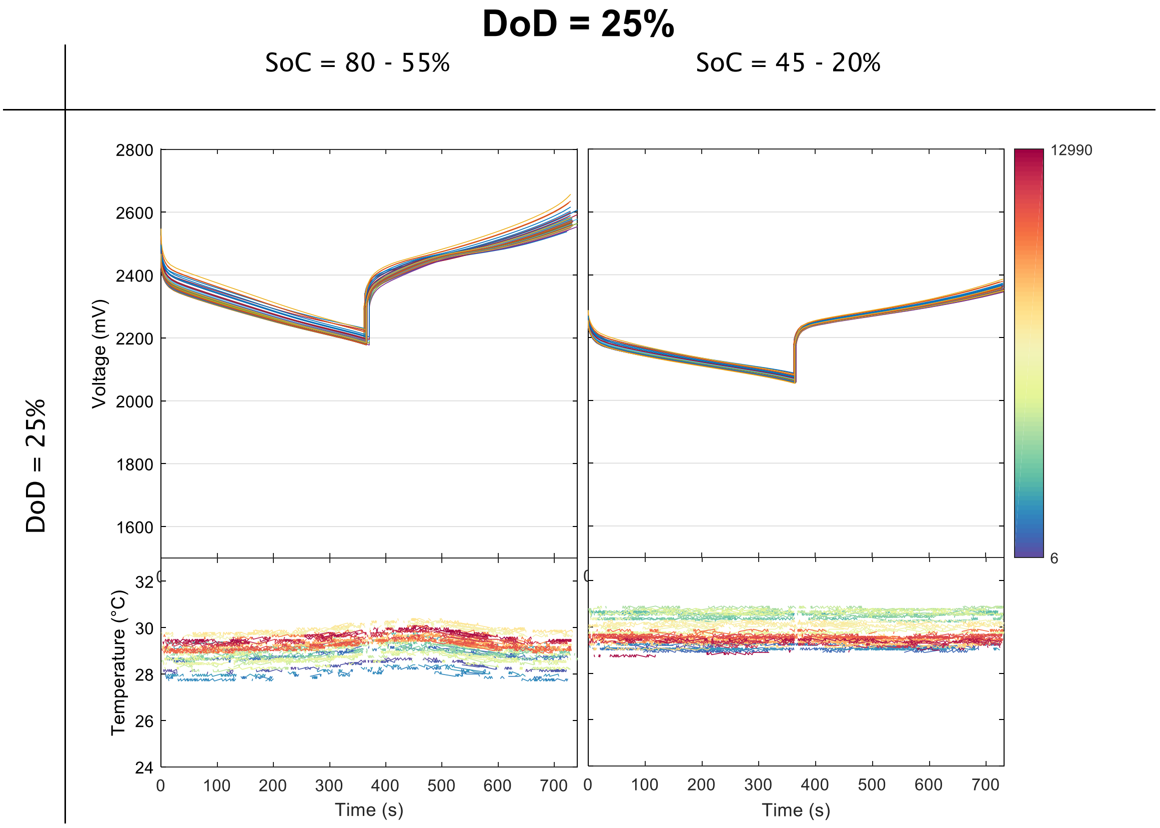

Figure 55: Evolution of voltage and temperature during cycling on two samples within a DoD of 25%

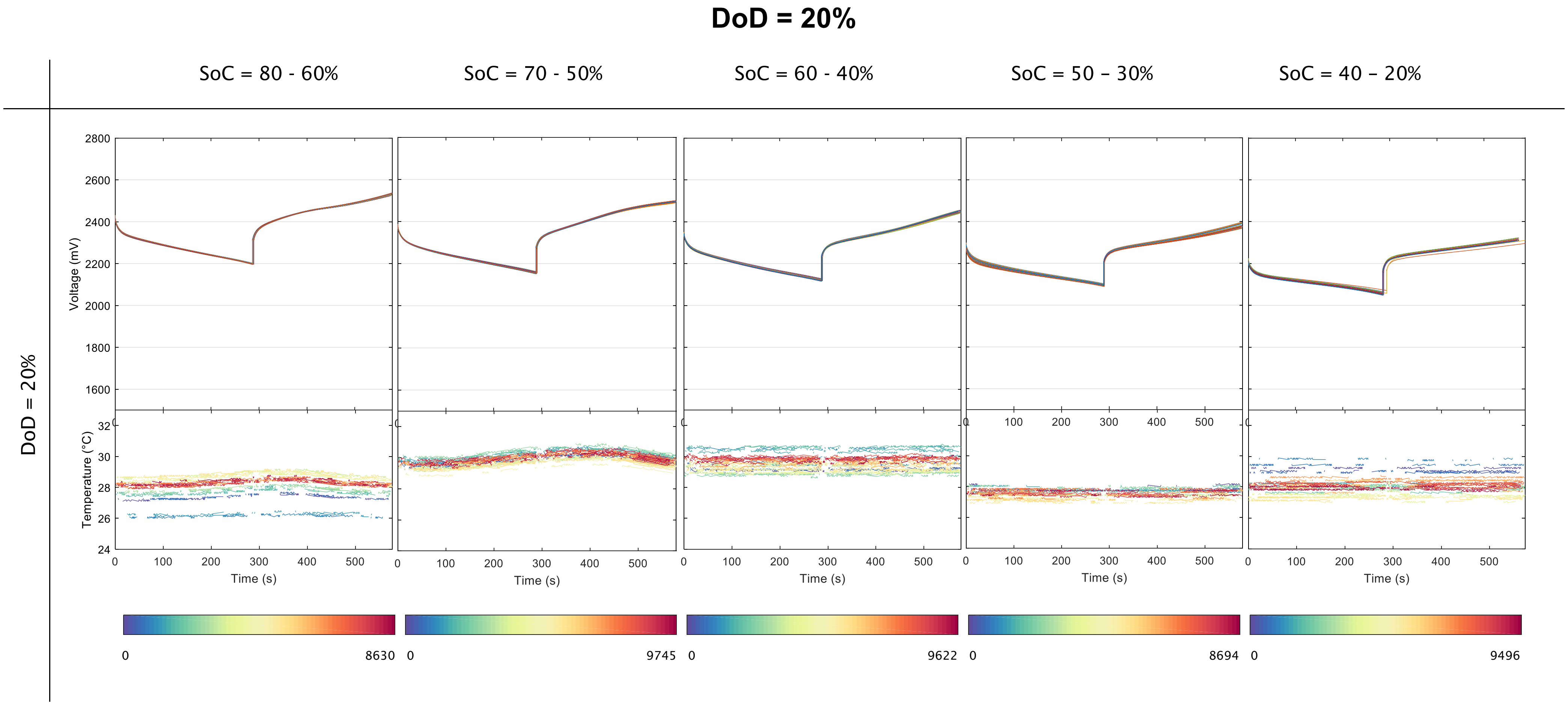

Figure 56: Evolution of voltage and temperature during cycling between different SoC equaling a DoD of 20%. The highest temperatures were reached when testing at middle SoC ranges.

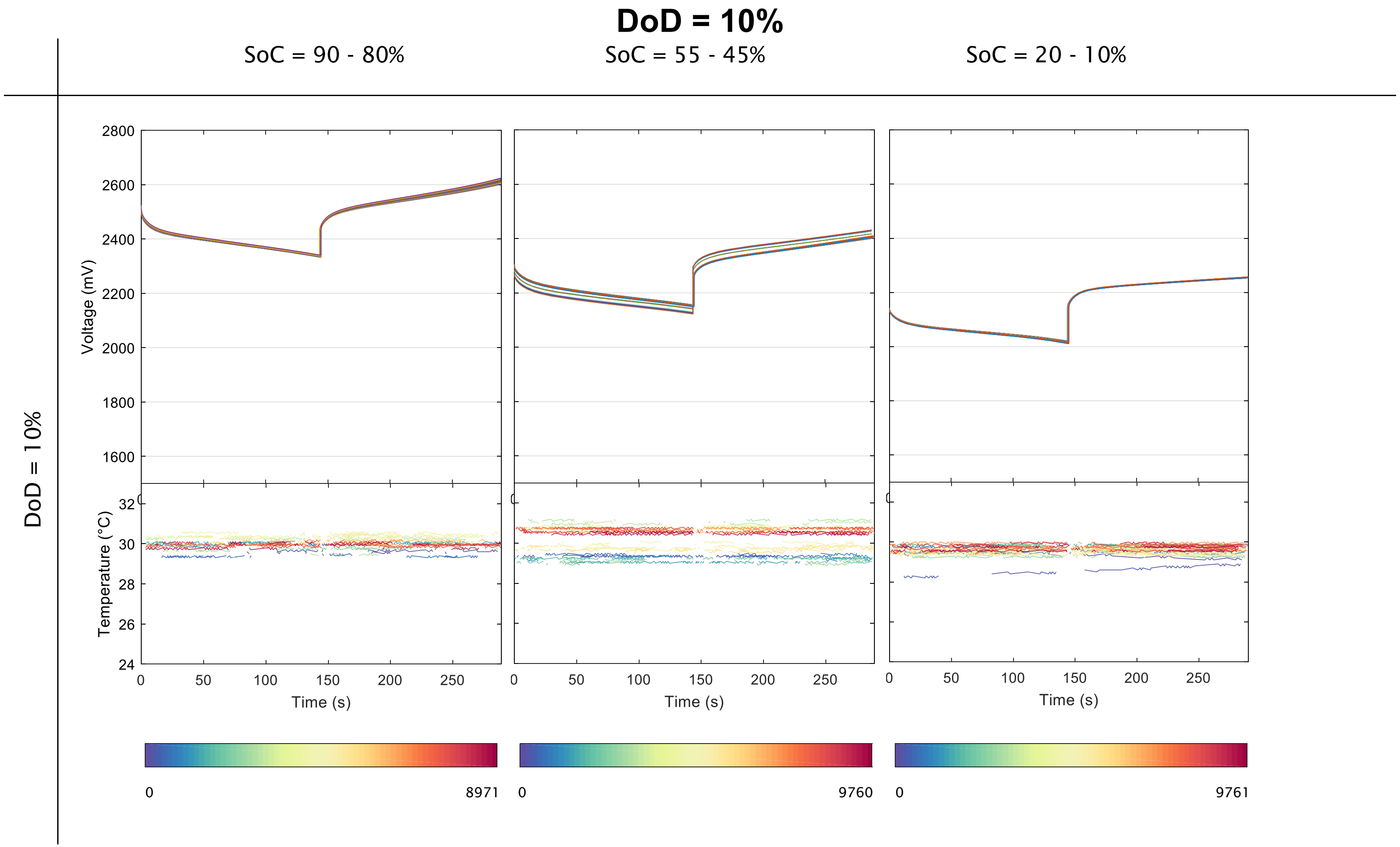

Figure 57: Evolution of voltage and temperature during cycling on three batteries between different SoC equaling a DoD of 10%

3.2.1.4 Knee point

The sudden capacity decay seen for the cells tested at 45 °C and the one at 25 °C (5.0 C) was already observed in [3]. In this study, three batteries with NMC as positive electrode and LTO as negative electrode materials were cycled with 3 C (charge, only CC), and 2 C (discharge, only CC) at 55 °C. One of these cells is the same cell that was tested in this study: the NMC/LTO cell from Toshiba[4]. The cell capacity fade results are depicted in Figure 58. In this study, after about 1000 cycles, the cell shows an obvious capacity fade. The capacity fade follows a two-stage piecewise linear model. A schematic of this two-stage capacity fade profile with cycle numbers is shown in Figure 58 (right side).

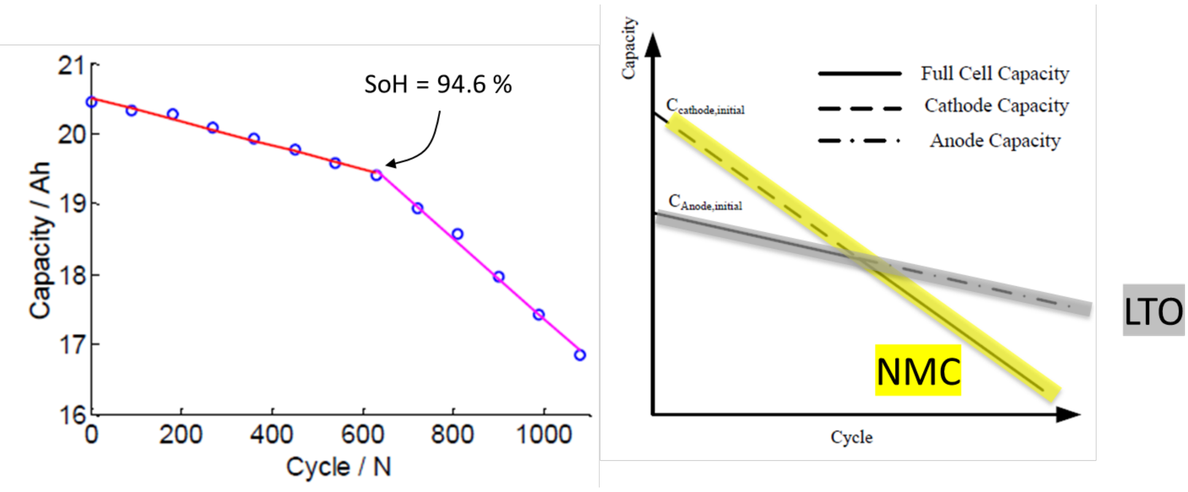

Figure 58: Knee point recorded in [5]. In this publication, cells were charged at 3 C (only CC), discharged at 2 C (only CC) at 55 °C.

The phenomenon shown in Figure 58 (left) denotes that the battery aging is not caused by a single mechanism. In different aging stages, the aging mechanism is different. The battery capacity depends on the minimum of the anode capacity and the cathode capacity. Usually, while manufacturing cells, the cathode material would be a little bit excessive. With the battery cycling, the capacity of both cathode and anode would fade, and the capacity loss rate is different. The cathode capacity decreases faster than the anode. Therefore, at the beginning, the battery capacity mainly depends on the anode and the battery capacity fade rate is nearly the capacity fade rate of the anode, and this fade rate is lower. After some cycles, because the cathode capacity decreases faster than the anode, the capacity of the cathode drops lower than the one of the anode, then the battery capacity mainly depends on the cathode and the overall capacity fade rate becomes higher.

The capacity fade mechanism is schematically shown in Figure 58 (right). In the first stage, or the stage prior to the knee point, the anode (*i.e.*, negative electrode) capacity is less than the cathode (*i.e.*, positive electrode) capacity. The battery capacity mainly depends on the anode capacity. The capacity fade mechanism in the stage two after the knee point mainly depends on the cathode.

---

[3] Han Xuebing et al., Energies (2014), 7, 4895-4909, https://www.mdpi.com/1996-1073/7/8/4895

[4] This information was provided to BFH by Toshiba. Also, the parameters listed in the publication (weight, capacity, chemistry, OCV, dQ/dU vs. U) match our experimental results quite well.

[5] Han Xuebing et al., Energies (2014), 7, 4895-4909, https://www.mdpi.com/1996-1073/7/8/4895

We plotted the SoH value at which the knee point became visible as a function of temperature. The results are shown in Figure 59.

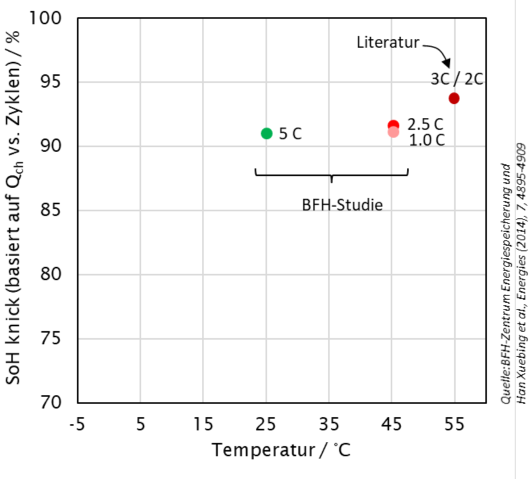

Figure 59: Knee point as a function of testing conditions. The “Literatur” data stems from [6].

While the knee-point in the publication was reached at SoH = 94.6%, it was not reached during our experiments until SoH = 92-93%. For 25 °C, DoD = 100% and 2.5 C, no knee point could be seen above SoH = 88.9%. This suggests that the knee point may depend on the cycling conditions such as temperature and C-rate.

3.3 Electrochemical impedance spectroscopy analysis

Our EIS analysis is focused on the extraction of R_0 (also called R_{el} - or R_B in Figure 60), which represents ohmic resistance, and R_1 (R_{CT} in Figure 60) which represents charge transfer resistance of the battery. R_0 and R_1 are dependent on the SoC of the battery and vary with increasing cycle number.

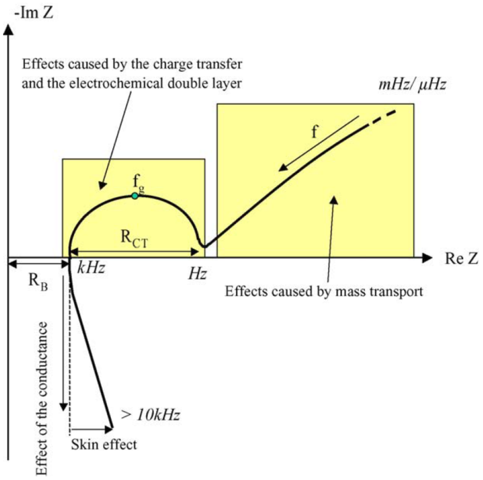

Figure 60: Nyquist plot with one semi-circle [7]. A second semi-circle is also common in lithium-ion batteries.

---

[6] Han Xuebing et al., Energies (2014), 7, 4895-4909, https://www.mdpi.com/1996-1073/7/8/4895

[7] Jossen, “Fundamentals of battery dynamics”, Journal of Power Sources 154 (2006) 530 – 538

3.3.1.1 EIS analysis for DoD = 100%

The EIS results on all cells are depicted in Figure 61 to **Error! Reference source not found.**.

The Nyquist plots, as for example Figure 61 relative to the cells tested at 25 °C, show a higher increase in charge transfer resistance than in ohmic resistance, regardless of the test condition. Highest increase in impedance is seen for the higher C-rates. The differences in impedance behavior is more visible for SoC 100% and 50%. SoC 0% shows no clear difference during the first thousands of cycles. According to these results, aging rate increases in the order 5.0 C > 2.5 C > 1.0 C.

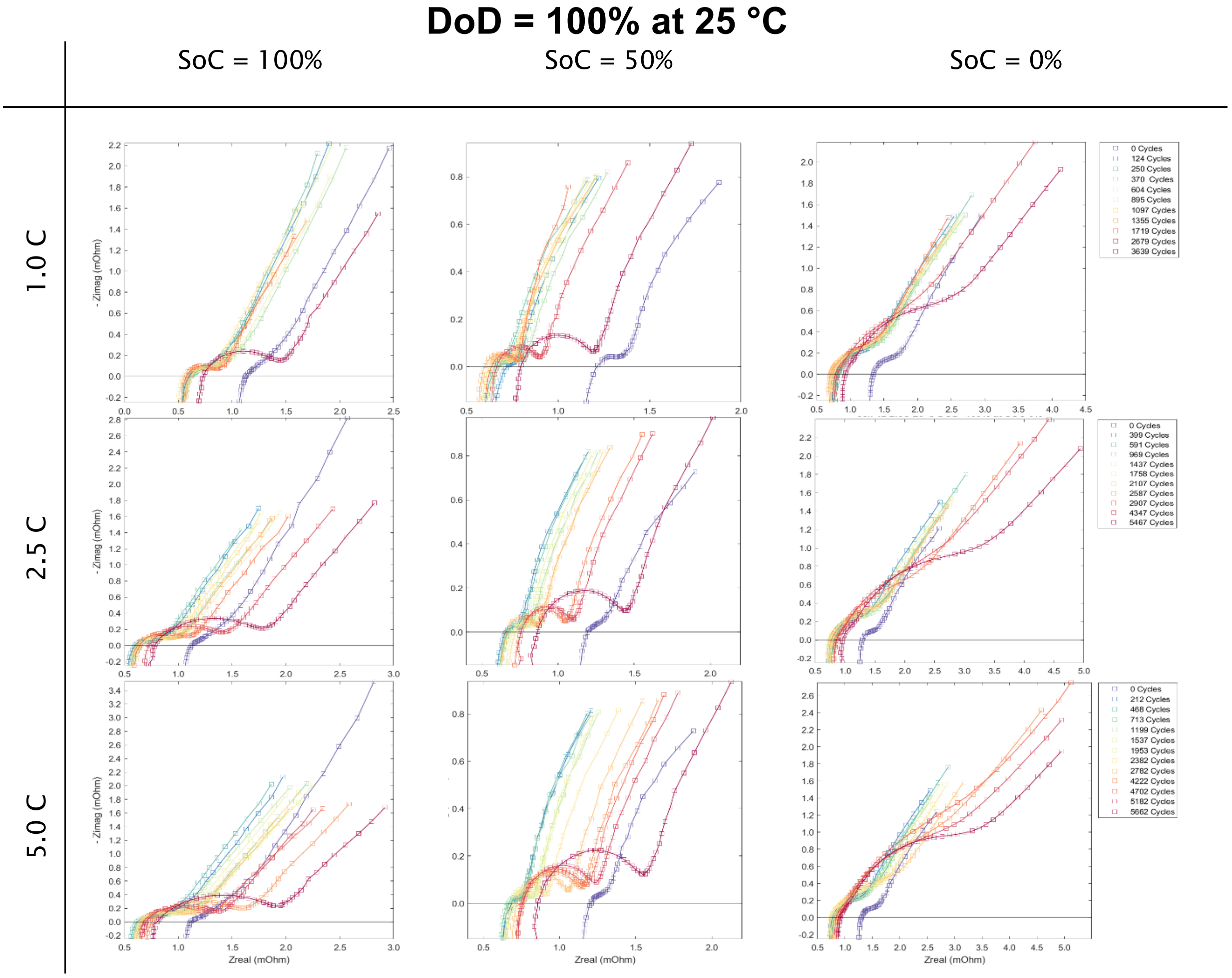

Figure 61: Nyquist plots from EIS-measurements performed at 100%, 50%, and 0% SoC on the batteries tested at DoD = 100% and 25 °C at three different C-rates

As seen in Figure 33, in terms of possible number of cycles until SoH 80%, aging at 45 °C was similar for the 1.0 C and 2.5 C testing conditions. The plots with the resistances, extrapolated from the Nyquist plots, shown in Figure 62 suggest a faster aging (on a cycle count basis) **for the 1.0 C cell** (pink dots): the increase of the ohmic and polarization resistances and thus the nominal **R_0 and R_1 values are higher** for this condition **than** for the **sample cycled at 2.5 C** (red dots). One explanation for this behavior could be the fact that the cell at 2.5 C was cycled much faster and had to spend less time at 45 °C until SoH 80%. When comparing the results using the same test time or exposure time at 45 °C, the condition of 2.5 C proves to be the best test condition for expanding lifespan. One can therefore deduct that **calendaric aging played a significant role at 45 °C** in terms of both capacity loss and impedance increase.
The impedance results of the cells testes at 10 °C (blue and turquoise dots) underpin the fact that cycling the batteries at higher C-rates induces a faster impedance increase and thus aging. For the cell tested at -5 °C (violet dots), only a small relative difference in impedance behavior is noted after ca. 1700 cycles. This goes in line with the capacity measurements for the same cycle number, where aging in terms of capacity loss was neglectable. The evolution of R_0 and R_1 values at SoC 100%, 50%, and 0% for the samples cycled between SoC 100% and 0% at different C-rates are summarized in Figure 62.

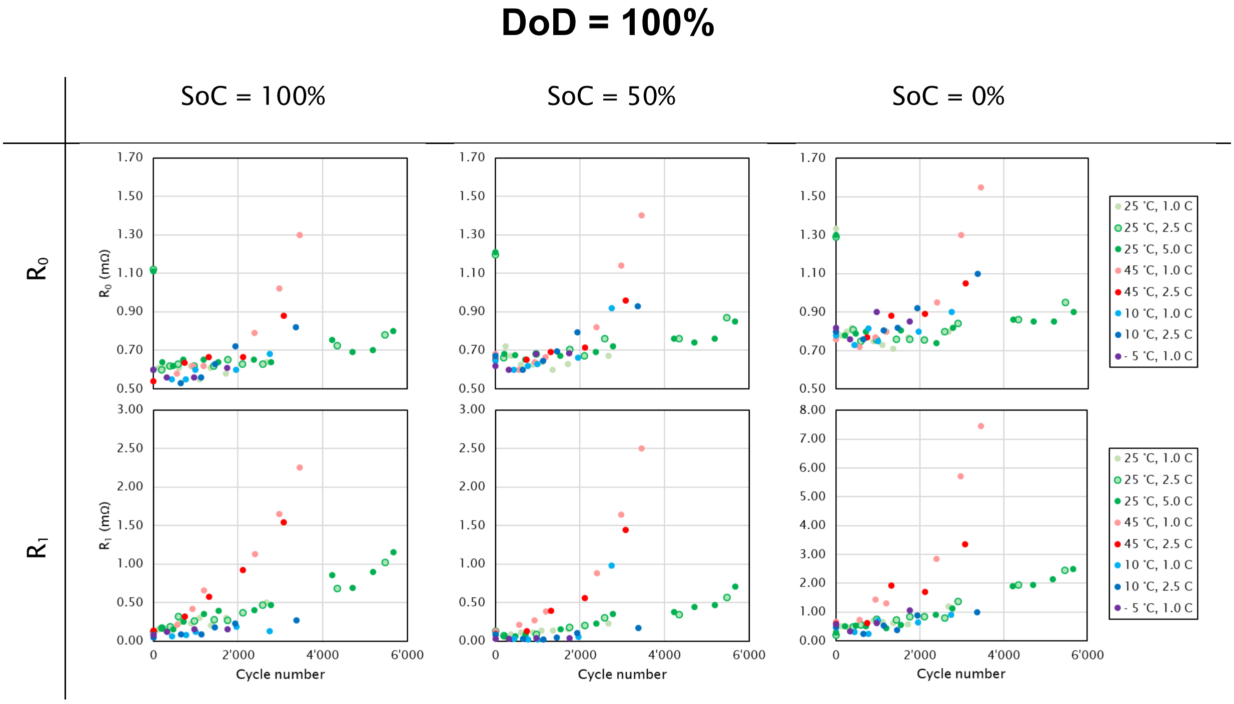

Figure 62: Evolution of R_0 and R_1 values as a function of cycle number for all tests at DoD = 100% at SoC = 100%, 50%, and 0%

3.3.1.2 EIS analysis for DoD < 100%

Figure 63 shows a stronger variation in the impedance development for both R_0 and R_1 values for the sample cycled between SoC 90% and 10% (DoD = 80%) than that cycled between SoC 85% and 20% (DoD = 65%). This observation is in accord with the aging behavior according to the capacity measurements.

For DoD = 25% (Figure 64) the lower SoC range shows a slightly higher increase in R_1 values at 50% SoC.

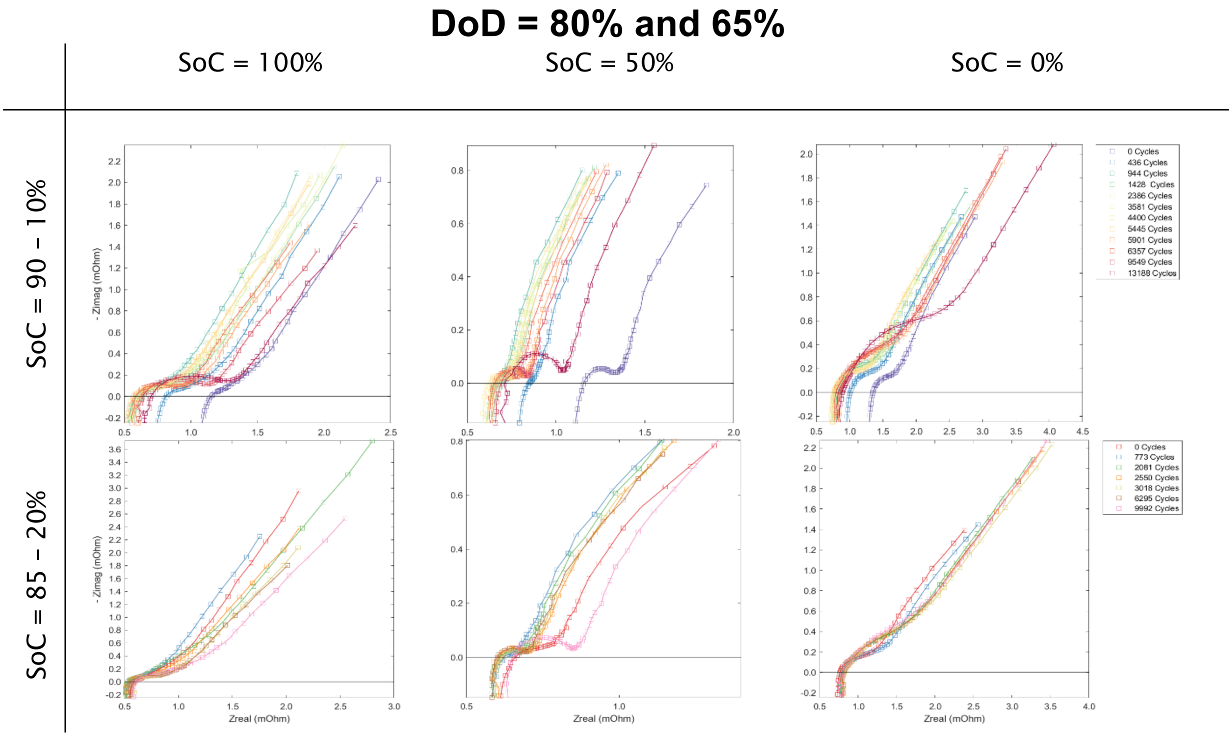

Figure 63: Nyquist plots from EIS-measurements at SoC 100%, 50%, and 0% batteries cycled within different SoC ranges (DoD = 80 and 65%) at 2.5 C, 25 °C

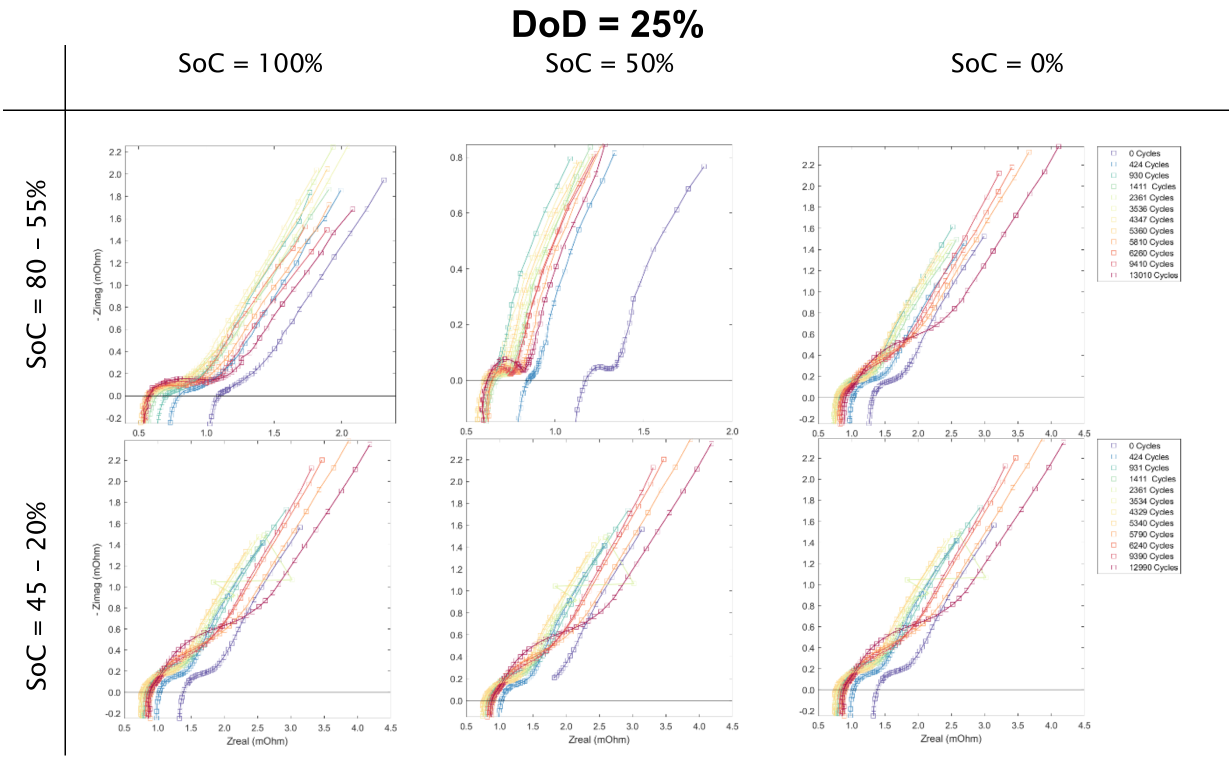

Figure 64: Nyquist plots from EIS-measurements at SoC 100%, 50%, and 0% batteries cycled within an SoC range of 25%

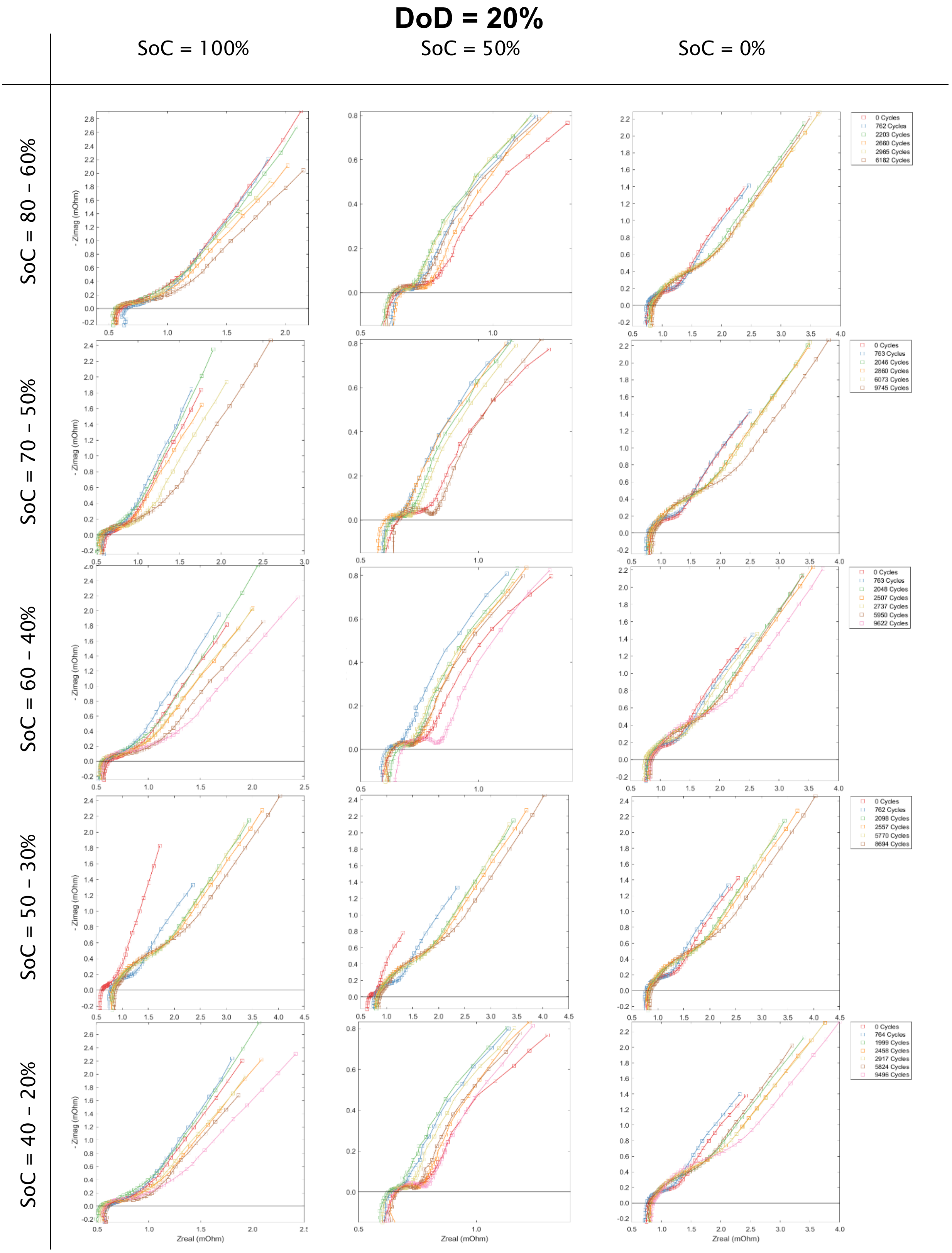

Figure 65: Nyquist plots from EIS-measurements at SoC 100%, 50%, and 0% from batteries cycled within different SoC ranges (DoD = 20%) at 2.5 C, 25 °C

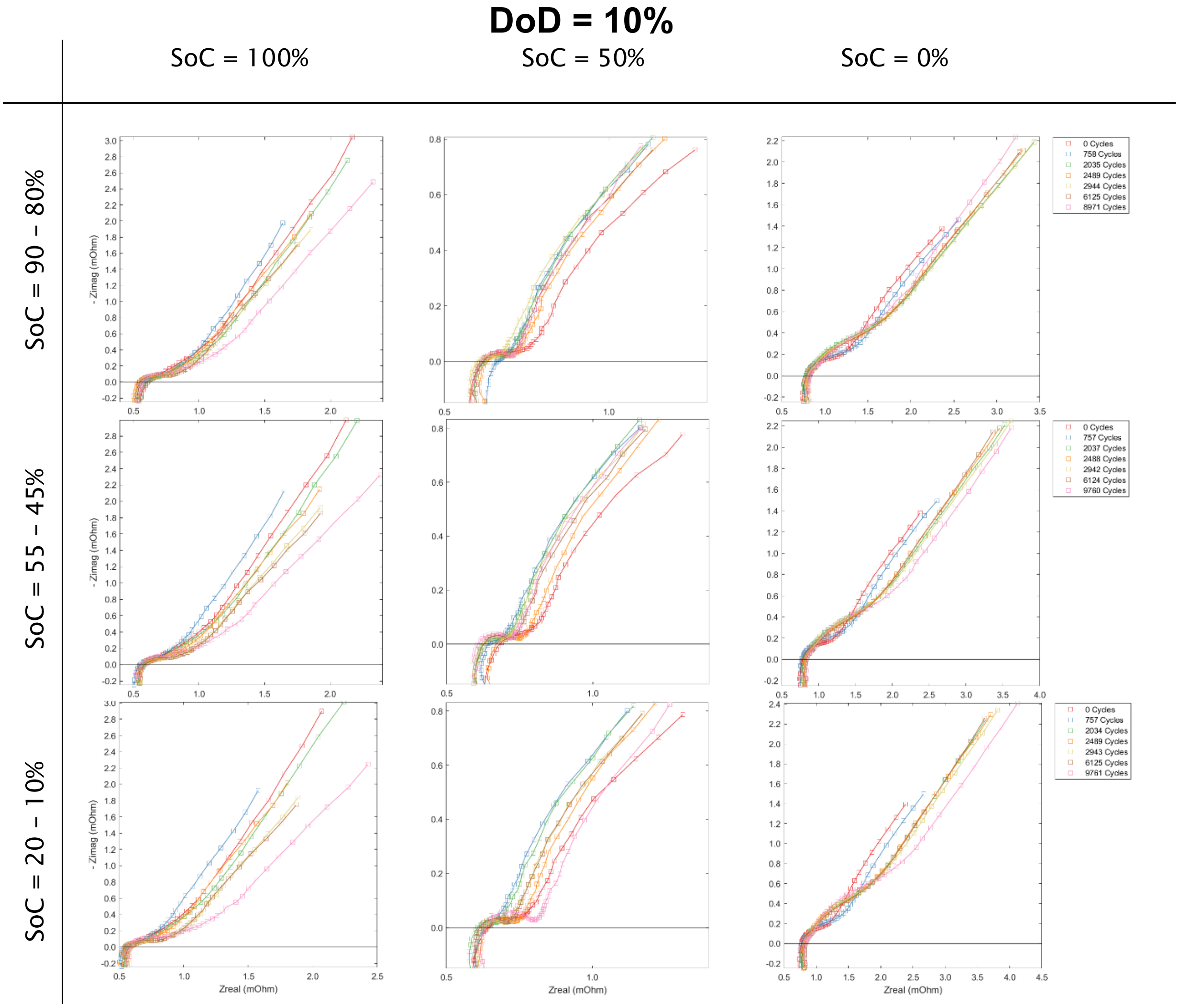

Figure 66: Nyquist plots from EIS-measurements at SoC 100%, 50%, and 0% from batteries cycled within different SoC ranges (DoD = 10%) at 2.5 C, 25 °C

As shown in Figure 65, all samples cycled at DoD 20% show very similar EIS results except for the one cycled between SoC 50% and 30%. For this cell, impedance effects caused by mass transport (linear section of the Nyquist plot at low frequencies) are visible at Z_{real} values of approximately 2.0 – 2.5 mOhm. We cannot conclude from these results whether this effect reflects lesser aging per cycle count compared to other DoD 20% tests.

In contrast to the IC curves shown before for DoD 10%, EIS results for cells tested at DoD 10% show very similar results (Figure 66).

3.3.2 Incremental capacity and incremental temperature analysis

The battery aging mechanism identification based on the incremental capacity (IC) analysis, is an *in-situ* method, and could be used in the real vehicle BMS to find the battery SOH. Usually the IC curves are derived from the OCV curves or constant current charge/discharge curves of very low charge/discharge rates. In this report, the IC curves are derived from the 2.5 C constant current charge and discharge curves during the diagnostic cycles at the corresponding temperature at which the cells were cycled. We chose 2.5 C instead of C/3 because it delivered clearer qualitative results.

IC curves provide information about material properties during charge and discharge. The IC graph portrays the degree at which charge is moved per unit of potential or voltage variation. The curve reflects the changes in the composition of the electrode materials. Analogously, the incremental temperature (IT) curve depicts the degree at which temperature increases or decreases per unit of voltage variation, portraying thermodynamic processes occurring inside the battery during usage.

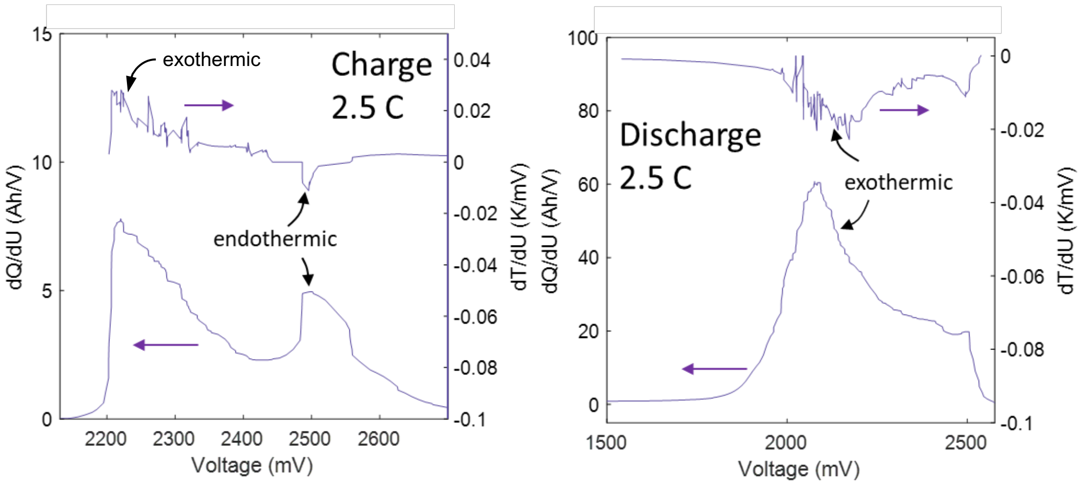

Figure 67: IC and IT curves derived out from the charge and discharge at 2.5 C

Therefore, IC and IT curves were plotted to qualify the change in chemical, physical and thermal properties of batteries tested under different conditions.

The purpose of the IC and IT analysis consists on finding changes in battery properties not captured by the charge and energy capacity measurements to define on a qualitative basis which conditions are best suitable for lifespan maximization.

Figure 68 depicts the variation of the IC and IT curves as a function of cycle number. When IC and IT data are generated from the discharge voltage values, a shift of dQ/dU vs. U to the left reflects an Increase of internal resistance, whereas a shift of dQ/dU vs. U to the downside reflects a change of material properties. The opposite is true when the IC and IT curves are derived from the voltage data during charge. As mentioned before, for both charge and discharge, heat exchange with the atmosphere occurs primarily during the phase transition region. As shown earlier, the discharge has an exothermic nature and is therefore accompanied by heat release, the charge is accompanied by both exothermic and endothermic processes (see 2.5 C measurements in Figure 68).

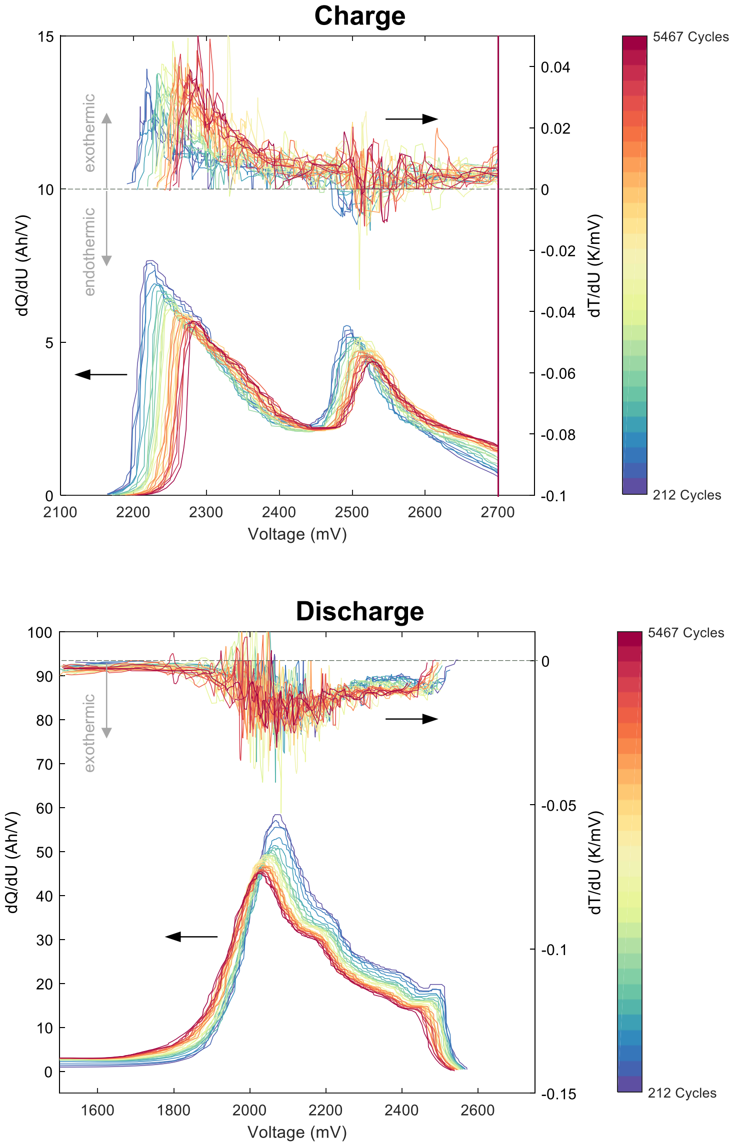

Figure 68: Incremental capacity (IC) and incremental temperature (IT) curves derived from the charge (top) and discharge (bottom) voltage profile recorded at 2.5 C for the cell tested at DoD = 100%, 2.5 C and 25 °C.

3.3.2.1 IC and IT analysis for DoD < 100%

IC and IT curves for DoD less than 100% are depicted from Figure 69 to Figure 72.

Figure 69 shows a stronger variation in the IC and IT curves for the sample cycled between SoC 90% and 10% (DoD = 80%) than that cycled between SoC 85% and 20% (DoD = 65%). This means that, as expected, lower DoD extend battery lifespan compared to higher DoD.

The results at DoD = 25% (Figure 70) show ambiguous results. For instance, the discharge IC curves in Figure 70 suggest that cycling within the lower SoC range (SoC = 45 - 20%) induced a larger change in material properties (shift downwards) compared to cycling in the upper half of the SoC range, which, on the other hand, showed a larger increase in internal resistance close to 2200 mV (shift to the left).

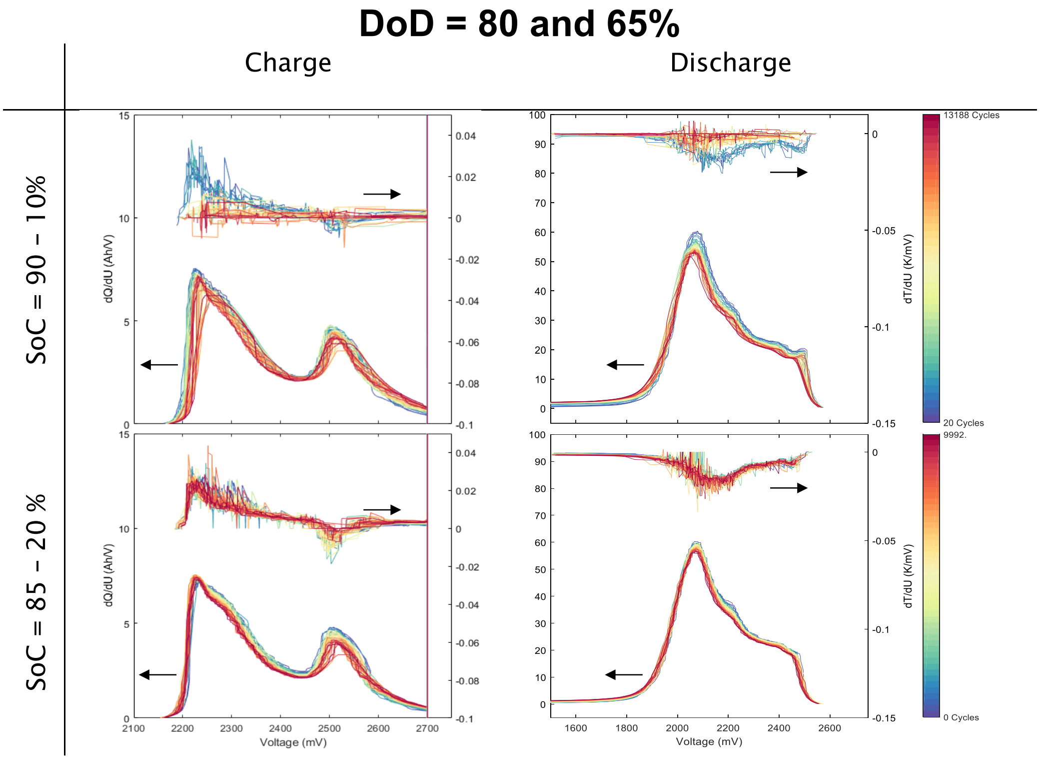

Figure 69: IC and IT curves for batteries cycled within different SoC ranges (DoD = 80 and 65%) at 2.5 C, 25 °C

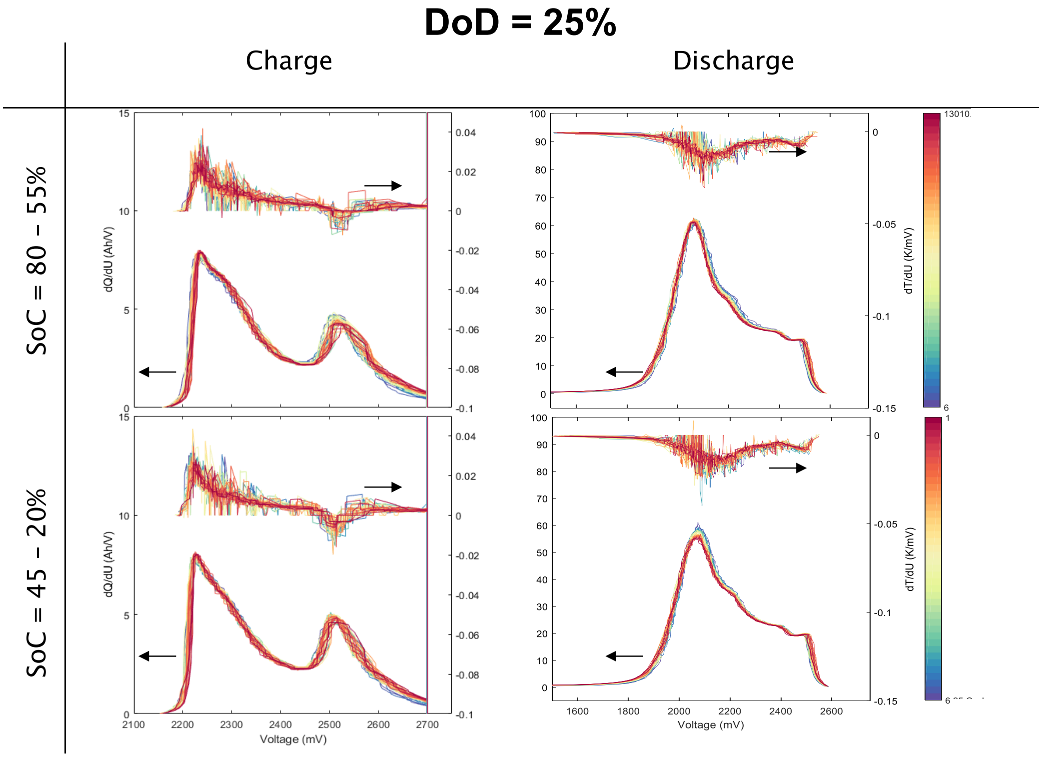

Figure 70: IC and IT curves for batteries cycled within different SoC ranges (DoD = 10%) at 2.5 C, 25 °C

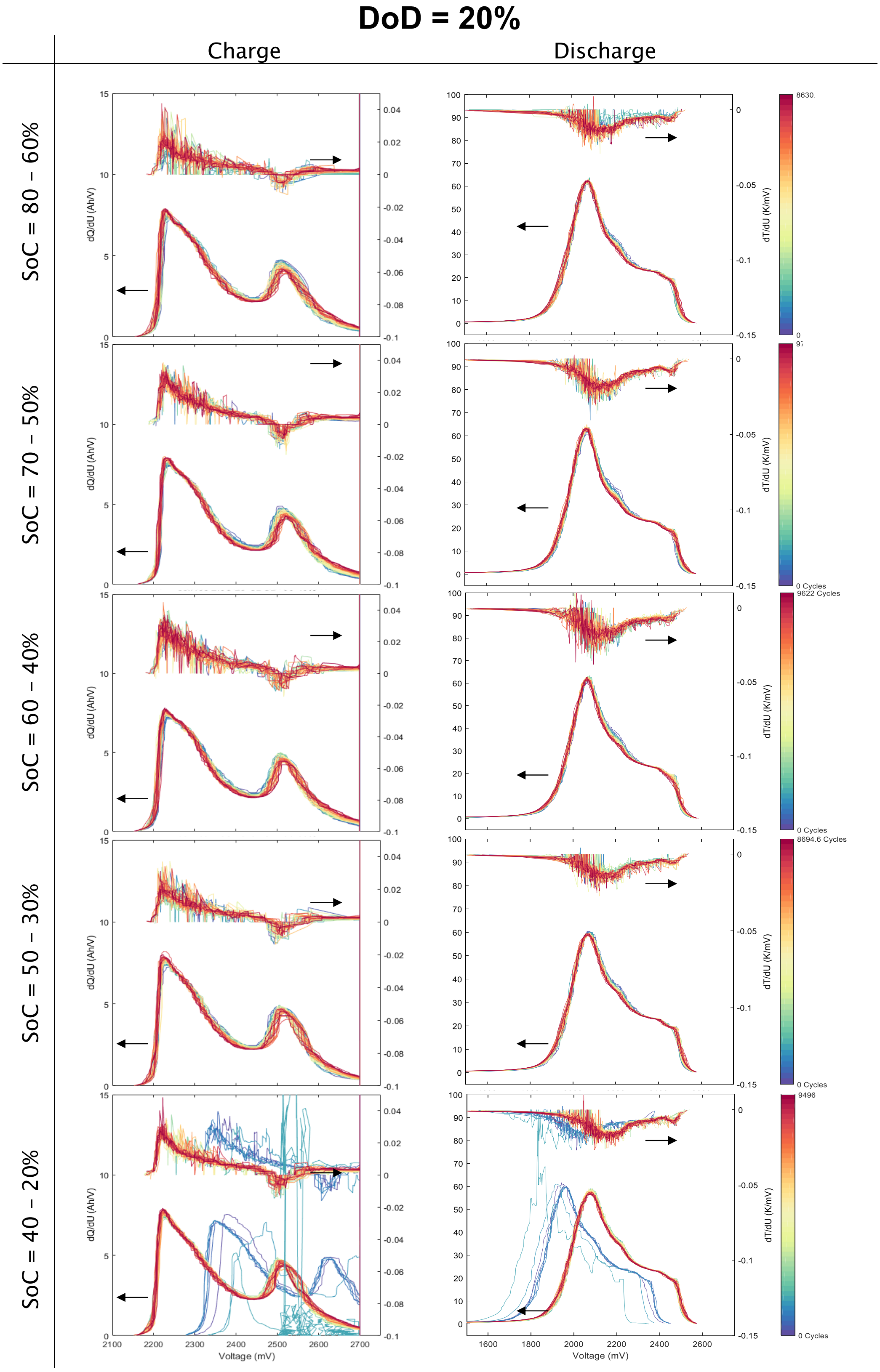

Figure 71: IC and IT curves for batteries cycled within different SoC ranges (DoD = 20%) at 2.5 C, 25 °C

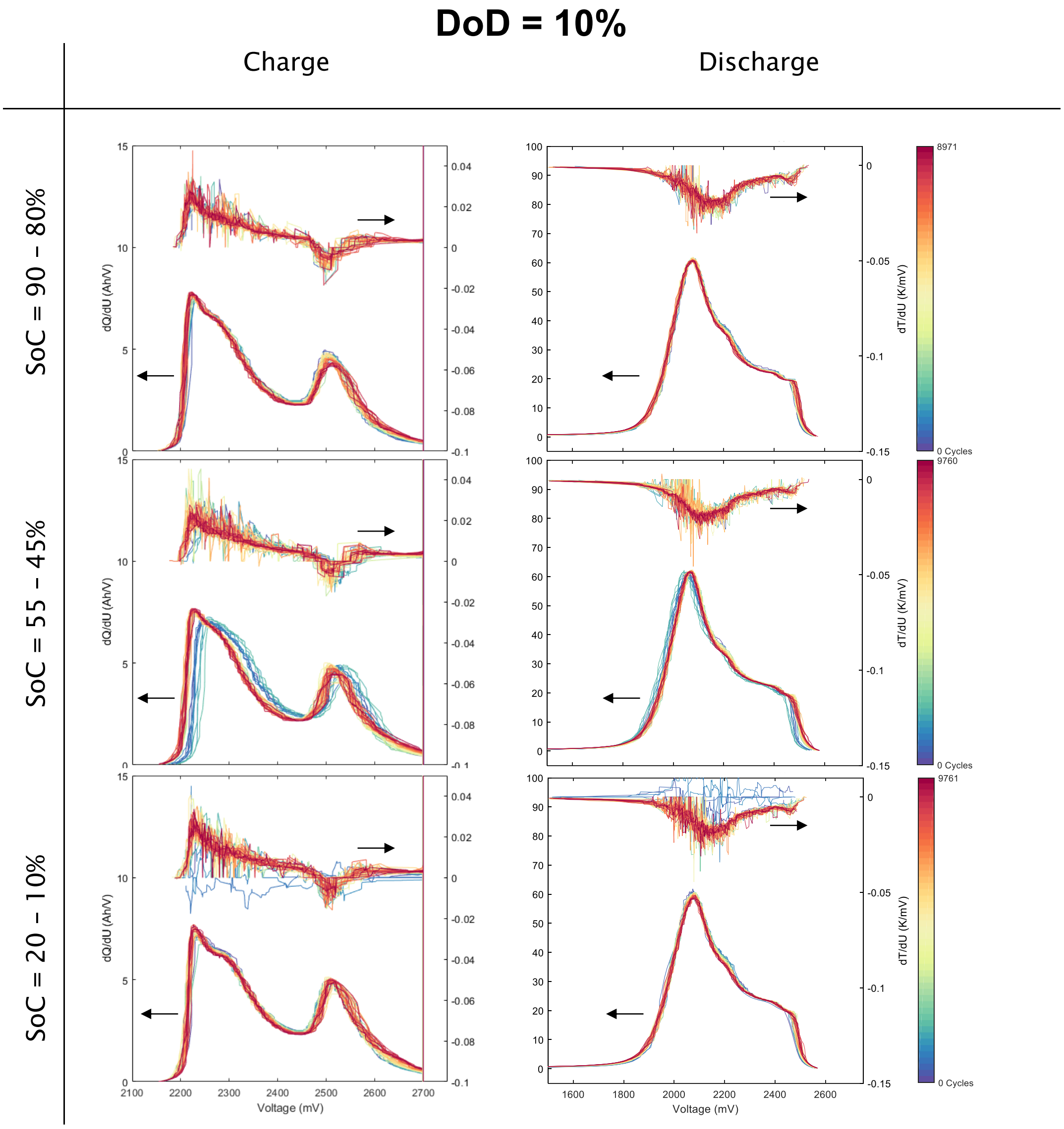

Figure 72: IC and IT curves for batteries cycled within different SoC ranges (DoD = 10%) at 2.5 C, 25 °C

For DoD = 20% (Figure 71), the largest temperature increase rate during discharge (IT curve) was obtained for the SoC range 60% - 40%, where the phase transition region appears. No clear differences can be seen on the IC curves, expect for the condition SoC 40% - 20%, which change could have been caused by the faster voltage drop found in the proximity of the lower voltage limit and not necessarily by capacity degradation or other aging phenomena.

According to results for tests conducted at DoD = 10% (Figure 72), most of the change in voltage response seen in the charge and discharge IC curves are visible for the sample tested between SoC 55% and 45%. Contrary to our expectations, the discharge IC curve shifts to the right and not to the left, whereas the charge IC curve shifts to the left and not the right. Such behavior suggests a decrease in internal resistance during cycling. The mere fact that IC curves shift the most for tests between SoC 55% and 45% and remain almost equal for the lower and upper SoC ranges may be indicative of unwanted processes altering the quality of materials and physical-chemical properties in the middle SoC ranges. Therefore, following these results, we assume that the aging rate is highest for middle SoC ranges.

3.3.3 Graphical User Interface (GUI) of the SOH model

All the results presented above have been used to create an offline graphical user interface (Figure 73). As it was shown in the paragraphs before (3.2), the battery system usable capacity decreases with the number of charging and discharging cycles. These ageing phenomena are C-rate dependent and, above all, temperature dependent. The results have shown that the number of achievable cycles, until the cell reaches its end of life, follows an inverse Gaussian distribution. This because the decrease in SOH per charge and discharge cycle is considered as a stochastic process with a certain mean and a certain variance. Thus, the exact number of achievable cycles cannot be calculated, but only an area, in which the number of achievable cycles is located, can be estimated.

The results show that there is a significant temperature dependence of the number of cycles. For example, the cell achieves an average of around 12,000 full cycles at 10°C ambient temperature, around 10,000 full cycles at 25°C and around 4,200 full cycles at 45°C. If the cell is loaded with partial cycles, the number of cycles increases significantly. At a discharge depth of 80% (charge and discharge between 90% SOC and 10% SOC), the cells reach around 65,000 cycles. With a discharge depth of 10% (between 55% SOC and 45% SOC), the cells even reach around 1.5 million cycles. The relationship between the discharge depth and the number of cycles is described by an exponential decrease of the DOD as a function of the number of cycles.

The combination of the stochastic model, the exponential model and the so-called Rainflow algorithm makes it possible to calculate the number of driving cycles for a real driving profile. For example, for a specific case, the Rainflow algorithm was able to extract 150 subcycles from a two-hour trip on a scheduled route. By using these input parameters (DoD and Crate of the subcycles) in the SOH model GUI, it was estimated that the bus can travel this route about 68,000 times until the battery reaches the end of its life. If the bus makes about 20 trips a day, this results in a service life of over nine years. For other routes that are not used as frequently, or for which the DoD and Crate are even lower, (example in Figure 73) around 30 years is possible.

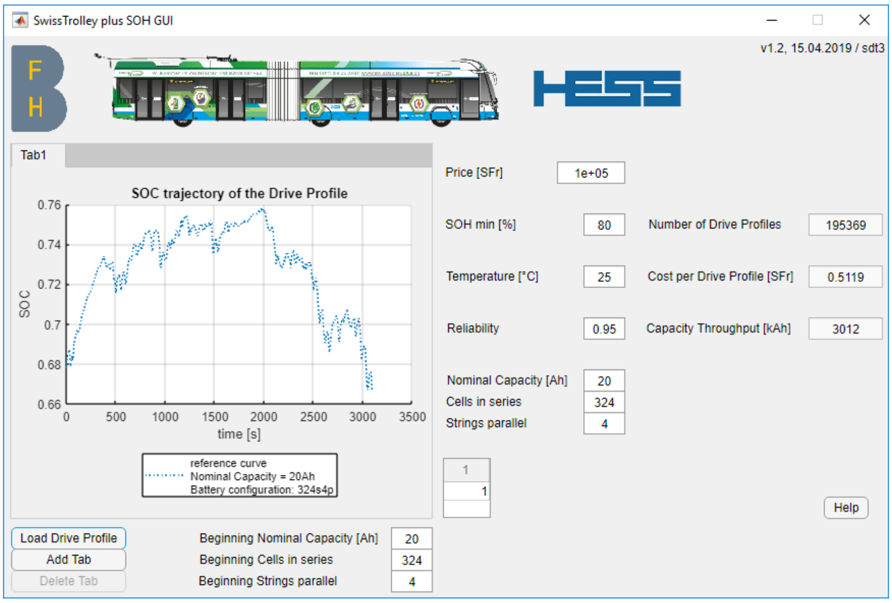

Price [SFr] 1e+05

SOH min [%] 80

Number of Drive Profiles 195369

Temperature [°C] 25

Cost per Drive Profile [SFr] 0.5119

Reliability 0.95

Capacity Throughput [kAh] 3012

Nominal Capacity [Ah] 20

Cells in series 324

Strings parallel 4

1
1

Beginning Nominal Capacity [Ah] 20

Beginning Cells in series 324

Beginning Strings parallel 4

Figure 73.Graphical User interface of the SOH model.

4 Conclusions

During the project «SwissTrolley plus» an energy management system (EMS) was developed and implemented on the prototype vehicle. The chosen approach consists of an additional onboard computer that communicates with the vehicle control unit (VCU) and offers suggestions on how to split the power demand of the traction system and the auxiliary devices between the battery and the over-head wires. The computer runs a custom modularized software which follows a robust and extendable design.

The resulting EMS allows to reduce the grid losses and avoid arc flashes at wire switches. A further energy saving potential is demonstrated in software-in-the-loop simulations based on model predictive control (MPC). Each of these aspects are discussed in more detail below.

Key features of the implemented software and the corresponding development workflows are as follows.

- The parallel execution of independent tasks in separate threads (so-called modules) allows not only to develop new parts of the software independently, but also allows to revise existing parts and replace them easily. Such a flexible solution is especially important when research is conducted on a prototype that is in regular operation. This approach has already been described in the annual report of 2017 and is not further elaborated here.
- Software logs and data recordings are automatically transferred to a secured cloud storage to which engineers of both Carrosserie AG and ETH Zurich are granted access. In order to make the data easily accessible, a tool has been developed to automatically convert the raw data to various more convenient formats, and extract meta data such as the driven distance, consumed energy, etc. Moreover, the process maintains a database which allows to quickly gain an overview on the system’s performance.
- In order to inspect and monitor the running system, we implemented secure remote access via a virtual private network (VPN). This access also allows to deploy new software releases easily. The system is thereby not crucially affected, as the EMS automatically switches to the backup implementation provided by the VCU.
- In addition to these passive approaches, an alert system has been implemented. This notification service enables the software to take action itself when something unexpected happens. Thereby, the software creates so-called GitLab issues on the GitLab server that hosts the code of the software. Such issues are typically used by the developers in order to organize the software development. In order to receive automatic notifications, users of GitLab can subscribe to specific labels and receive an e-mail whenever a new issue is created.
- Maintainability of the software code is ensured via the combined practices of continuous integration and continuous delivery (CI/CD) in which well-defined processes ensure that the software can be developed in several paths in parallel while keeping a clean common mainline [16], [17], [18], [19], and [20]. In CI/CD, every snapshot—in Git terms referred to as “commit”—is automatically tested for its integrity. That means the code must compile and all tests must pass successfully. This process is thereby defined in terms of so-called pipelines that are executed by the GitLab server in a well-defined setting.

At the time of writing this report, the following EMS approaches have been implemented and tested on the prototype vehicle in real operation.

- An online EMS strategy based on optimal control theory, i.e., adaptive equivalent consumption minimization strategy (ECMS), was implemented. The strategy distributes the instantaneous power demand between the battery and the overhead grid based on only very few parameters. The most important one is the target SOE which allows to define the desired long-term goal of the battery state. In contrast to the heuristic strategy present in the backup system, the adaptive ECMS aims for reducing the consumed energy at the grid feed points. As a result, the grid losses and the power peeks are inherently respected and reduced.
- An additional control algorithm, referred to as line break controller, is able to anticipate line breaks caused for instance by wire switches and thereby avoid arc flashes. The pursued approach involves to so-called self-learning road map (SLRM) which enables the vehicle to learn its environment in real-time. The successful implementation of line break controller is thus seen as validation for the proper working of the road map.

The simulation studies conducted within this project demonstrate a further energy saving potential and grid load reduction when using MPC.

- Based on a demanding but feasible route scenario, the simulation study reveals that an EMS using predictive information performs superior to the current strategies. MPC is able to keep the additional energy consumption compared to the best possible strategy at the same level of around 4%, whereas the other strategies have increased energy consumptions of up to 11% when the battery size is halved.
- Moreover, MPC allows to include additional operation limits of any physical component and additional quality criteria in an intuitive way into the internal optimization problem.

Although heating, ventilation and air-conditioning (HVAC) systems typically consume as much energy as the traction system, we unfortunately did not have the time to develop an energy management strategy that includes HVAC equipment. With various studies, however, the foundations for understanding and modeling the complex interrelationships have been elaborated, which can now be used in successive works. Moreover, the developed MPC framework can easily be extended with additional measurement signals and control inputs once the models of the thermodynamic systems and the interfaces to the HVAC devices are established.

Regarding the characterization of the battery lifetime, it can be concluded that to evaluate a new battery technology a large volume of tests is needed. In general, mapping the performances at different operating conditions is necessary if the battery systems need to be optimized for a ‘real’ use in which different ambient temperatures and high C-rate are expected as in mobility applications. By exploring the operating range so deeply, suggestions for when and how charging/discharging the battery pack can be made. All the different testing techniques and data analysis serve to prove with high reliability and accuracy findings that, given the novelty of the technology, might be surprising at a first look. Moreover, as pointed out in the result analysis part, the evaluation process does not depend only from energy or capacity parameter, for example internal resistance, impedance measurements as well as thermal behavior analysis are complementary and necessary information that are needed to optimize the operation of the complete system. These findings are needed to support the EMS operating strategy with time, always trying to keep the degradation rate as low as possible still satisfying the energy/power requirements of the application. The findings of the work highlighted also that the higher investment costs of the LTO cells compared to NMC (as well as slightly lower energy density of these cell) is economic valuable if there is need of a long-lasting system (20 years) that is operated in a systematic way (recursive path of public transportation) in cold environment as Switzerland.

In summary, the following claims can be made based on the experimental findings presented in this text.

- Cycling at low temperatures (for example - 5 °C) is beneficial for lifespan maximization.

- For the same environmental temperature, higher C-rates degrade the cells faster
- Compared to other cell chemistries, the charge and discharge capacity degradation obtained was very low for NMC/LTO cells.
- Charging is accompanied by an endothermic process taking place at the phase transition region. This behavior is opposite to conventional graphite-based cells.
- Discharging is accompanied by an exothermic process taking place at the phase transition region. This behavior is opposite to conventional graphite-based cells.
- Discharge is more detrimental for battery lifespan than charging. This stands in contradiction to the behavior of conventional graphite-based cells (see annual report from 31.01.2017, Section 2.2.1).
- Aging is a two-stage process, where capacity decay in the first and second stage is limited by aging caused by the LTO and NMC electrode, respectively.
- No clear capacity degradation was noticed for cells cycled at DoD = 20%. Extrapolation of data for aging quantification was challenging and many assumptions were made.
- No capacity degradation was noticed for cells cycled at DoD = 10%. Extrapolation of data for aging quantification was challenging and many assumptions were made.
- Methods such as EIS, IC, IT, and R_{DC}, did not provide clear capacity loss or internal resistance increase signs for all tests at DoD = 20% and DoD = 10% (internal resistance appears to decrease for the cycling condition SoC 55–45%, however, more cycling would be necessary to conclude on whether middle SoC ranges are more detrimental to battery lifespan).

5 Outlook and next steps

The main achievement of this research project is the design and implementation of control algorithms at a technology readiness level (TRL) 6. The developed software comes along with well-structured workflows and an extensive documentation of the entire project. Based on these products, engineers at Carrosserie HESS AG have a good foundation for successive adaptations and developments for their bus fleet. Moreover, by using the software with the line break controller, arc flashes at wire switches are avoided and the abrasion of the corresponding grid elements is reduced. An expansion of the proposed strategy to an entire bus fleet may reduce the grid maintenance costs considerably at the benefit of the public transport provider, e.g., Verkehrsbetriebe Zürich (VBZ).

The proposed control strategies can also be considered as general ideas, where the specific implementation is of secondary importance. The prototype vehicle «SwissTrolley plus» serves thereby as a demonstrator which motivates the deployment of electric mobility in public transportation. Hopefully, the illustrated benefits of using battery-assisted trolley buses influence other vehicle manufacturers and transportation service providers to pursue into similar directions.

Unfortunately, a previously implemented EMS approach—the trip-wise adaptive ECMS—did not prove itself to be reliable enough for real-world operation. It was presented and described in the annual project report of 2017. As the variances between several trips on the same bus route are too different, the trip-wise adaptive ECMS was not able to learn the route-specific equivalence factors properly. Various ideas to extend the approach were considered, but none of them was promising enough. The concept of using the SLRM for predicting the upcoming driving scenario and using this data in a model predictive control (MPC) fashion was more likely to lead to success and, offered a more flexible framework.

Moreover, this MPC approach is much easier applicable to other types of vehicle. Although a certain repetitive driving behavior must be present, the SLRM can cover much more general situations then those that exist in public transportation. In principle, the presented approach can be used for any type of vehicle which drives the same routes once in a while. However, a few adaptions might be useful to both the construction algorithm of the SLRM and EMS strategy which uses the predictions from the SLRM. First, the current version inserts nodes uniformly spaced with five meters. If we consider for example trucks running long distances on highways, this distance is probably to short and may cause unnecessary amount of data. Second, in applications where the vehicles do not have dedicated lanes as it is often the case for buses in public transportation, the velocity might be very sensitive to the time of the day. Therefore, this information could be considered while storing and predicting the up-coming driving scenario. Finally, the use of the prediction in the MPC highly depends on the specific optimization target. In the approach presented here, we calculate the expected traction power profile based on the predicted velocity and altitude profile, the grid availability, and on estimations of the vehicle mass and the auxiliary power. The optimization then calculates the optimal strategy for using the power from the battery and the overhead grid. For a different type of vehicle, e.g. a hybrid truck with a combustion engine, the predicted data will be used for a different optimization criterion. Of course, this change of the target vehicle implies some adaptions of the optimization problem formulation. However, the general idea of the presented approach remains the same.

The goal of the upcoming months is to push the MPC approach from the simulation stage to the deployment stage, where it will finally run on the vehicle in real-time. With this strategy we will finally have the possibility to combine all aspects that have been investigated during this project.

Furthermore, based on the battery health model of BFH-TI presented in this report, we aim for integrating the battery degradation as a criterion into the energy management strategy. The proposed approach relies on a so-called severity map, which encodes how harmful certain operations are with respect to the battery health. The underlying theory is adopted from the Palmgren-Miner fatigue model used for mechanical components [52]. A corresponding strategy to include the battery health in the control strategy might be similar to [53].

Such a control strategy will, however, not be able to guarantee a specific battery life without another feedback loop. As the lithium titanate oxide (LTO) battery used in the «SwissTrolley plus» configuration is remarkably durable, the aging effects are extremely slow. An instantaneous controller is thus not able to account for these dynamics and needs further supervisory guidance. The proposed approach consists of regularly carrying out measurements to obtain the current health of the battery and use this data to adjust the instantaneous controller. This adjustment may be formulated as a tuning parameter which penalizes the usage of the battery. Decision guidance for this adjustment can be derived from the software tool of BFH-TI that estimates the life time of a battery based on its operation. If the predicted end-of-life based on capacity and resistance measurements happens too soon, the battery usage should be penalized more, and vice versa.

6 National and international cooperation

The project «SwissTrolley plus» is a cooperation between the industrial partners Carrosserie HESS AG and Verkehrsbetriebe Zürich (VBZ) and the academic institutions ETH Zurich and BFH-TI. It is separated into a research part and a product demonstration part. Accordingly, two applications for funding have been established, where both are granted by the Swiss Federal Office of Energy (SFOE). These are

- a P+D+L project (https://www.aramis.admin.ch/Texte/?ProjectID=36721), and
- a F+E project (https://www.aramis.admin.ch/Texte/?ProjectID=37064).

The first project is conducted by Carrosserie HESS AG and VBZ and thus summarized and concluded in their final report. The main achievement is the design and implementation of a new concept for the traction system. Compared to regular trolley buses, the new prototype vehicle is mostly a battery electric vehicle that is extended with trolley bus components only where necessary, i.e., at the connection to the overhead grid. The onboard electrical system is thereby galvanically isolated from the overhead grid, which allows to use more efficient electrical components. As a result, the «SwissTrolley plus» prototype achieves a 15% reduction of the overall energy consumption compared to trolley buses of the previous generation. This value was both theoretically calculated and measured in a field test. Furthermore, the onboard traction battery allows to drive in battery mode for up to 20% of the distance of regular bus routes. This flexibility enables the public transportation provider to extend existing bus route and to remove the overhead grid in sections of the route where it causes particularly high infrastructure costs.

The second project is covered in this report. It consists of two parts which describe the activities and results achieved by the two research institutes, respectively, i.e.,

- the Institute for Dynamic Systems and Control (IDSC) of ETH Zurich and
- the Department Engineering and Information Technology (BFH-TI) of the Bern University of Applied Sciences.

Both institutes collaborated with Carrosserie HESS AG within the F+E project and thus established a close connection to the P+D+L project. Moreover, the findings of BFH-TI regarding the ideal operation of the battery offer additional possibilities to improve the EMS developed by ETH Zurich. These collaborations and the corresponding references to the final report of the P+D+L project are depicted in the following sections.

6.1 Collaboration Between Carrosserie HESS AG and ETH Zurich

The first part of this report mainly discusses the development and current state of the supervisory energy management system (EMS), which offers suggestions on how to operate the battery of the hybrid propulsion system ideally. The chosen approach to integrate this supervisory controller into the vehicle control unit has thereby been developed in close collaboration with the engineers of Carrosserie HESS AG. In fact, within the P+D+L project, the engineers of Carrosserie HESS AG have developed a backup EMS which is able to operate all traction components including the battery. As a result, the bus is fully operational without the supervisory control as the suggestions provided by the supervisory control are not a necessity for the system, but only a supplementary data input to further reduce the energy consumption.

As a result of this design, the interface between the developments of Carrosserie HESS AG within the P+D+L project and ETH Zurich within the F+E project is well defined and reduced to the communication interface that connects the two onboard computers. Accordingly, this final report integrates into the P+D+L report where it discusses the research part and the EMS. On the other hand, this report revisits the P+D+L report, i.e., section 2.2.3 briefly addresses the field campaign conducted by Carrosserie HESS AG and VBZ and discusses the achieved results.

6.2 Collaboration Between Carrosserie HESS AG and BFH-TI

The second part of this report addresses the lithium titanate oxide (LTO) battery technology. During the F+E project BFH-TI thoroughly investigated the aging of the battery under various operating conditions. The influence of temperature, Crate and Depth of Discharge (DoD) was extensively mapped in terms of capacity fade and internal resistance increase among other indicators. The results were used to derive a state of health (SOH) model for the battery which enables Carrosserie HESS AG to estimate the lifespan of their battery system. The model requires as input the battery initial capacity, its architecture, the operating temperature and the driving profile. By means of a rainflow algorithm, Crates and DoDs are extracted from the given trolley-bus driving profile. Based on the experimentally measured trends (capacity decrease/internal resistance increase with respect to operating conditions), the lifetime can be estimated. Accordingly, the P+D+L project report addresses the usage of the developed life model. In particular, engineers of Carrosserie HESS AG plan to use the graphical user interface (GUI) to adjust the battery size of new battery-assisted trolley buses and electric buses for the respective customer demands.

6.3 Collaboration Between ETH Zurich and BFH-TI

The life model developed by BFH-TI will also be used to adjust the EMS once it includes the battery utilization explicitly. As described in section 5 of this report, future versions of the supervisory control will respect the harmfulness of certain battery operations on the battery's lifespan. Based on a severity maps derived from BFH-TI's findings depicted in Figure 33 and Figure 40 the usage of electric energy from the battery is penalized in order to reduce the stress on the chemistry and thus to prolong the battery lifetime. However, in order to ensure the proper operation of this control scheme, the battery's condition must be measured and validated periodically. A corresponding measurement routine was developed by BFH-TI and is described in appendix 10. If the measurements diverge from the expected aging process, the control has to be tuned accordingly.

7 Communication

The project «SwissTrolley plus» was presented to the media on January 17, 2017. As part of the media conference and the representation of the project on its website, www.swisstrolleyplus.ch, a short movie was created in which the teams of researchers at ETH Zürich and BFH-TI are involved.

Members of the scientific community as well as the general public were also informed about BFH-TI’s ongoing cooperation with Carrosserie HESS AG, VBZ, ETH Zürich and BFE via the BFH’s magazine “Spirit Biel/Bienne” on its June-release of 2017, www.spirit.bfh.ch/de/archiv.html.

Additionally, a poster was presented at the 4th SCCER Mobility Annual Conference at ETH Zurich on September 15, 2017.

8 Publications

On December 2016, BFH-TI submitted a paper with the title “Aging in NMC/LTO cell by Impedance Model Parametrization” to the 19th Conference on Power Electronics and Applications, EPE’17 ECCE Europe, which took place in Warsaw, Poland, from September 11 to 14, 2017. The paper was accepted in early 2017. The authors of the publication were Dr. Neeta Khare, Prof. Andrea Vezzini and Mr. Christoph Giger. Prof. Vezzini presented the project via a poster session during the conference. The paper described impedance modeling of the NMC/LTO Li-ion cells after cycling at different operating conditions.

The self-learning road map as described in section 2.1.2 and in previous annual reports has been applied for a patent [21] on behalf of Carrosserie HESS AG on January 13, 2017.

As part of this project a large number of student projects have been carried out. The following categorized lists depict the conducted studies on mechatronics, Bachelor’s theses, semester projects, and Master’s theses at ETH.

- Energy Management:
  - Semester project by Jen Wei Niam [21], Jun. 2017:
    The contribution entitled “Online Energy Management of a Battery-Assisted Trolley Bus” presents an online ECMS controller that uses optimal control theory to minimize the energy consumption of a battery-assisted trolley bus.
  - Master’s thesis by Benedikt Sutter [23], Jan. 2017:
    The contribution entitled “Simultaneous Optimization of Vehicle Design and Driving Speed Profile” investigates the energy consumption of a battery-assisted trolley bus with respect to the combined optimization of the energy management and an the vehicle design.
  - Master’s thesis by Grigoriy Khazaridi [24], Feb. 2017:
    The contribution entitled “Energy Saving Potential of a Bus Fleet with Battery-Assisted Trolley Buses” analyzes the energy saving potential of a bus fleet including battery-assisted trolley buses.
  - Master’s thesis by Fabio Widmer [3], May 2017:
    The contribution entitled “Trip-Wise Adaptive ECMS for HEVs in Public Transportation” describes the derivation and implementation of the first energy management—the adaptive ECMS and the trip-wise ECMS—for the «SwissTrolley plus» prototype.
  - Master’s thesis by Cary Müller [7], Jun. 2019:
    The contribution entitled “Predictive Energy Management in Public Transportation based on Model Predictive Control” contains the development of a predictive energy management system for a battery-assisted trolley bus based on MPC.
- Modeling and Estimation:
  - Bachelor’s thesis by Reto Michael [25], Jun. 2015:
    The contribution entitled “Optimal GPS Position Estimation via Vehicle Odometry” addresses the improvement of the GPS position estimate of a vehicle with a Kalman filter.
  - Semester project by Nicolai Stucki [26], Feb. 2016:
    The contribution entitled “Dynamic Model of a Trolley Bus Grid” provides the mathematical background for modeling the overhead grid and presents simulation results on realistic examples.

  - Master’s thesis by Micha Güdel [27], Apr. 2016:
    The contribution entitled “Dead Reckoning for Road Vehicles via a Kinematics Model” presents a new kinematics model of the vehicle that takes additional odometric sensory data into account in order to improve the accuracy of raw GPS position estimates.
  - Bachelor’s thesis by Basil Vetterli [28], Jun. 2017:
    The contribution entitled “Online Mass Estimation Using Kalman Filtering” presents the development of a mass estimator using a Kalman filter.
  - Semester project by Amir Mikail [29], Jun. 2017:
    The contribution entitled “Map-Based Grid Resistance Estimation for «SwissTrolley plus» ” derives an offline method to provide information about the grid resistance as a function of the current location of a trolley bus.
  - Bachelor’s thesis by Nathanaël Bourgeois [30], Jun. 2018:
    The contribution entitled “Offline Estimation of Vehicle and Passengers Mass” derives the first approach to estimate the vehicle parameters and vehicle mass using a quadratic program.
  - Master’s thesis by Reto Michael [31], Sep. 2018:
    The contribution entitled “Supervised and Unsupervised Estimation of Spatial Signals in Vehicular Applications” presents an estimation technique for the altitude based on hidden Markov models and an algorithm for the detection of bus routes based on unsupervised ma- chine learning.
  - Bachelor’s thesis by Michael Schmid [32], Jul. 2019:
    The contribution entitled “Improving the Kinematics Model” analyzes systematic improvements of the kinematics model which is used in the pose estimation algorithm.

- HVAC Systems:

  - Semester project by Micha Güdel [33], Jul. 2015:
    The contribution entitled “Investigation of HVAC Systems of Trolley Buses in Public Transportation” presents a more advanced thermodynamic model that accounts for thermal com- fort and is coupled with simulations of the drive train.
  - Bachelor’s thesis by Rafael Boduryan [34], Jun. 2017:
    The contribution entitled “Investigation of HVAC Systems of Trolley Buses in Public Transportation” extends the HVAC model such that it accounts for radiative heat transfer.
  - Studies on mechatronics by Philipp Bänninger [35], Jun. 2017:
    The contribution entitled “HVAC System Identification” compares the measurement data of the climate chamber experiments to the data that was recorded by the supervisory software of the «SwissTrolley plus» prototype, and draws first conclusions on the thermodynamic behavior during door openings.
  - Bachelor’s thesis by Philipp Bänninger [36], Aug. 2018:
    The contribution entitled “HVAC System Modeling” assesses the energy consumption and thermal comfort levels for radiant heating systems in trolley buses by deriving a three-dimensional model that is able to reproduce the relevant thermodynamic processes that occur due to outside disturbances.
  - Semester project by Felix Kieser [37], Jun. 2019:
    The contribution entitled “HVAC System Modeling” derives analytical models based on physical principles to describe the air exchange and heat losses during door openings.

- Offline Simulation and Data Processing:

  - Semester project by Benedikt Sutter [38], Nov. 2015:
    The contribution entitled “Automated Generation of Travel Routes” presents the development and implementation of a route creator to generate velocity profiles of arbitrarily chosen bus routes.
  - Bachelor’s thesis by Georg Lins [39], Jun. 2017:
    The contribution entitled “Simulation of a Trolley Bus Network” addresses the dynamic behavior of the electric overhead wires.
  - Studies on mechatronics by Pol Eyschen [40], Dec. 2018:
    The contribution entitled “Signal Post Processing from Different Sources” presents a data reconstruction and consolidation technique which allows merging data recordings from various sources.
  - Bachelor’s thesis by Pol Eyschen [41], May. 2019:
    The contribution entitled “Software in the Loop Tests” describes parameter identification approaches for the models of the electrical components of the vehicle and presents the improvements of the simulation framework that were achieved during the project.

- Route Planning, Mapping, and Prediction:
  - Semester project by Andyn Omanovic and Dejan Milojevic [42], Jun. 2017:
    The contribution entitled “Optimal Route Planning” presents a route planning application which calculates and visualizes an optimal route between two points based on open street map (OSM) data.
  - Master’s thesis by Jen Wei Niam [5], Dec. 2017:
    The contribution entitled “Implementation of a Self-Learning Road Map for Driving Prediction” presents improvements of the self-learning road map and its implementation on the «SwissTrolley plus» prototype.
  - Semester project by Tanja Norina Koch [43], Jan. 2018:
    The contribution entitled “Route Estimation” presents a concept to detect bus routes in an efficient and unsupervised way using bus stop sequences.
  - Studies on mechatronics by David Gerber [44], Apr. 2019:
    The contribution entitled “Cleaning the Self-Learning Road Map” categorizes artifacts present in the road map and presents a literature review of techniques to address them.
  - Studies on mechatronics by Michael Schmid [45], May. 2019:
    The contribution entitled “Literature Survey on Map-Matching” is a literature review of different existing map-matching algorithms.
  - Bachelor’s thesis by David Gerber [46], Jul. 2019:
    The contribution entitled “Autonomous Depot Recognition” derives a support vector machine (SVM) classification for autonomous recognition of bus depots.
  - Semester project by Guanzhong Quan [47], Jun. 2019:
    The contribution entitled “Velocity Predictions in Public Transportation Using a Self-Learning Road Map” derives a distance-to-time conversion algorithm based on a dwell-time parameter and analyzes the daytime dependency of the latter.

The project «SwissTrolley plus» was present in the media for several times where ETH Zurich was involved.

- In autumn 2016, a video about the entire project was recorded where the project members of ETH Zurich participated. The video is available on the project website [48].

- In January 2017, an interview with Oliver Obergfell from VBZ was recorded and released on the blog vbzonline [49].

- On October 4, 2017 ETH Industry Relations releases a video on their blog ETH News for Industry, in which the importance of the project as collaboration between industry and research is highlighted [50].
- In March 2018, the ETH magazine ETH Globe published an article about the relationship between research and industry [51].

9 References

[1] A. Ritter, P. Elbert, and C. Onder, “Energy Saving Potential of a Battery-Assisted Fleet of Trolley Buses,” presented at the 8th IFAC Symposium on Advances in Automotive Control AAC 2016, Norrköping, 2016, vol. 49, no. 11, pp. 377–384.

[2] Boltyanskii, V. G.; Gamkrelidze, R. V.; Pontryagin, L. S. (1956). К теории оптимальных процессов [Towards a Theory of Optimal Processes]. Dokl. Akad. Nauk SSSR (in Russian). 110 (1): 7–10. MR 0084444.

[3] F. Widmer, “Trip-wise adaptive ECMS for HEVs in public transportation”, Master’s Thesis, Swiss Federal Institute of Technology (ETH) Zurich, 2017.

[4] A. Ritter, “Prediction of future driving conditions based on self-learning road maps,” Master’s Thesis, ETH Zurich, Institute for Dynamic Systems and Control, Zurich, Switzerland, 2014.

[5] J. W. Niam, “Implementation of a self-learning road map for driving prediction” , Master’s Thesis, Swiss Federal Institute of Technology (ETH) Zurich, 2017.

[6] A. Ritter, F. Widmer, J. Wei Niam, P. Elbert, and C. H. Onder, "Probabilistic Predictions of Spatio-Temporal Data in Vehicular Applications," submitted for publication.

[7] C. Müller, “Predictive Energy Management in Public Transportation based on Model Predictive Control,” Master’s Thesis, ETH Zurich, Institute for Dynamic Systems and Control, Zurich, Switzerland, 2019.

[8] D. Simon, Optimal State Estimation: Kalman, H Infinity, and Nonlinear Approaches. John Wiley & Sons, Jun. 2006.

[9] Wei-Wen Kao, “Integration of GPS and dead-reckoning navigation systems,” in Vehicle Navigation and Information Systems Conference, 1991, vol. 2, Oct. 1991, pp. 635–643.

[10] P. Bonnifait, P. Bouron, P. Crubille, and D. Meizel, “Data fusion of four ABS sensors and GPS for an enhanced localization of car-like vehicles,” in Proceedings 2001 ICRA. IEEE International Conference on Robotics and Automation (Cat. No.01CH37164), vol. 2, May 2001, pp. 1597–1602 vol.2.

[11] D. J. Kim, M. K. Kim, K. S. Lee, H. G. Park, and M. H. Lee, "Localization system of autonomous vehicle via Kalman filtering," in 2011 11th International Conference on Control, Automation and Systems, Oct. 2011, pp. 934-937.

[12] M. Spangenberg, V. Calmettes, and J. Tourneref, “Fusion of GPS, INS and odometric data for automotive navigation,” in 2007 15th European Signal Processing Conference, Sep. 2007, pp. 886–890.

[13] A. Ndjeng Ndjeng, A. Lambert, D. Gruyer, and S. Glaser, “Experimental comparison of Kalman filters for vehicle localization,” in 2009 IEEE Intelligent Vehicles Symposium, Jun. 2009, pp. 441–446.

[14] R. Michael, “Optimal GPS position estimation via vehicle odometry,” Bachelor’s thesis, ETH Zurich, Institute for Dynamic Systems and Control, Zurich, Switzerland, Jun. 2015.

[15] M. Güdel, “Dead reckoning for road vehicles via a kinematics model,” Master’s thesis, ETH Zurich, Institute for Dynamic Systems and Control, Zurich, Switzerland, Apr. 2016.

[16] CI/CD. Wikipedia. Accessed: 2019-01-04. [Online]. Available: https://en.wikipedia.org/wiki/CI/CD

[17] Continuous integration. Wikipedia. Accessed: 2019-01-04. [Online]. Available: https://en.wikipedia.org/wiki/Continuous_integration

[18] Continuous delivery. Wikipedia. Accessed: 2019-01-04. [Online]. Available: https://en.wikipedia.org/wiki/Continuous_delivery

[19] GitLab continuous integration & delivery. GitLab. Accessed: 2019-01-04. [Online]. Available: https://about.gitlab.com/product/continuous-integration/

[20] GitLab Docs: GitLab continuous integration (GitLab CI/CD). GitLab. Accessed: 2019-01-04. [Online]. Available: https://docs.gitlab.com/ee/ci/

[21] A. H. Ritter, P. V. Elbert, C. H. Onder, A. Naef, M. Widmer, H.-J. Gisler: “Verfahren zur Vorhersage zukünftiger Fahrbedingungen für ein Fahrzeug“, EP-Patent Europa, Anmelde-Nr.: 17 151 441.7.

[22] J. W. Niam, “Online energy management of a battery-assisted trolley bus,” Semester project, ETH Zurich, Institute for Dynamic Systems and Control, Zurich, Switzerland, Jun. 2016.

[23] S. Benedikt, “Simultaneous optimization of vehicle design and driving speed profile,” Master’s thesis, ETH Zurich, Institute for Dynamic Systems and Control, Zurich, Switzerland, Jan. 2017.

[24] G. Khazaridi, "Energy saving potential of a bus fleet with battery-assisted trolley buses," Master's thesis, ETH Zurich, Institute for Dynamic Systems and Control, Zurich, Switzerland, Feb. 2017.

[25] R. Michael, “Optimal GPS position estimation via vehicle odometry,” Bachelor’s thesis, ETH Zurich, Institute for Dynamic Systems and Control, Zurich, Switzerland, Jun. 2015.

[26] S. Nicolai, “Dynamic model of a trolley bus grid,” Semester project, ETH Zurich, Institute for Dynamic Systems and Control, Zurich, Switzerland, Feb. 2016.

[27] M. Güdel, “Dead reckoning for road vehicles via a kinematics model,” Master’s thesis, ETH Zurich, Institute for Dynamic Systems and Control, Zurich, Switzerland, Apr. 2016.

[28] B. Vetterli, “Online mass estimation using Kalman filtering,” Bachelor’s thesis, ETH Zurich, Institute for Dynamic Systems and Control, Zurich, Switzerland, Jun. 2017.

[29] A. Mikail, “Map-based grid resistance estimation for swisstrolley plus,” Semester project, ETH Zurich, Institute for Dynamic Systems and Control, Zurich, Switzerland, Jun. 2017.

[30] N. Bourgeois, “Offline estimation of vehicle parameters and passengers mass,” Bachelor’s thesis, ETH Zurich, Institute for Dynamic Systems and Control, Zurich, Switzerland, Jun. 2018.

[31] R. Michael, “Supervised and unsupervised estimation of spatial signals in vehicular applications: From data analysis to implementation,” Master’s thesis, ETH Zurich, Institute for Dynamic Systems and Control, Zurich, Switzerland, Sep. 2018.

[32] M. Schmid, “Improving the kinematics model: Extending the pose estimation model with additional measurement signals,” Bachelor’s thesis, ETH Zurich, Institute for Dynamic Systems and Control, Zurich, Switzerland, Jul. 2019.

[33] M. Güdel, “Investigation of HVAC systems of trolley buses in public transportation,” Semester project, ETH Zurich, Institute for Dynamic Systems and Control, Zurich, Switzerland, Jul. 2015.

[34] R. Boduryan, “Investigation of hvac systems of trolley buses in public transportation,” Bachelor’s thesis, ETH Zurich, Institute for Dynamic Systems and Control, Zurich, Switzerland, Jun. 2017.

[35] P. Bänninger, “HVAC system identification: Effects of door openings on temperature distributions in the passenger compartment,” Studies on mechatronics, ETH Zurich, Institute for Dynamic Systems and Control, Zurich, Switzerland, Apr. 2018.

[36] P. Bänninger, “HVAC system modeling: Assessment of energy consumption and thermal comfort levels for radiant heating systems in trolley buses,” Bachelor’s thesis, ETH Zurich, Insti- tute for Dynamic Systems and Control, Zurich, Switzerland, Aug. 2018.

[37] F. Kieser, “HVAC system modeling,” Semester project, ETH Zurich, Institute for Dynamic Systems and Control, Zurich, Switzerland, Jun. 2019.

[38] B. Sutter, “Automated generation of travel routes,” Semester project, ETH Zurich, Institute for Dynamic Systems and Control, Zurich, Switzerland, Nov. 2015

[39] G. Lins, “Simulation of a trolley bus network,” Bachelor’s thesis, ETH Zurich, Institute for Dynamic Systems and Control, Zurich, Switzerland, Jun. 2017.

[40] P. Eyschen, “Signal post processing from different sources,” Studies on mechatronics, ETH Zurich, Institute for Dynamic Systems and Control, Zurich, Switzerland, Dec. 2018.

[41] P. Eyschen, “Software in the loop tests,” Bachelor’s thesis, ETH Zurich, Institute for Dynamic Systems and Control, Zurich, Switzerland, May 2019.

[42] A. Omanovic and D. Milojevic, “Optimal route planning,” Semester project, ETH Zurich, Institute for Dynamic Systems and Control, Zurich, Switzerland, Jun. 2017.

[43] T. N. Koch, “Route estimation: An algorithm for swisstrolley plus that detects bus routes,” Semester project, ETH Zurich, Institute for Dynamic Systems and Control, Zurich, Switzerland, Jan. 2018.

[44] D. Gerber, “Cleaning the self-learning road map: Survey of algorithms for detecting and eliminating road map artifacts,” Studies on mechatronics, ETH Zurich, Institute for Dynamic Systems and Control, Zurich, Switzerland, Apr. 2019.

[45] M. Schmid, “Literature survey on map-matching,” Studies on mechatronics, ETH Zurich, Institute for Dynamic Systems and Control, Zurich, Switzerland, May 2019

[46] D. Gerber, “Autonomous depot recognition,” Bachelor’s thesis, ETH Zurich, Institute for Dynamic Systems and Control, Zurich, Switzerland, Jul. 2019.

[47] G. Quan, “Velocity predictions in public transportation using a self-learning road map,” Semester project, ETH Zurich, Institute for Dynamic Systems and Control, Zurich, Switzerland, Jun. 2019.

[48] SwissTrolley plus project website, Accessed: 2019-06-20. [Online]. Available: https://www.swisstrolleyplus.ch/en/

[49] O. Obergfell, “Hier Fährt Die Zukunft", vbzonline, January 17, 2017. [Online]. Available: https://vbzonline.ch/hier-fahrt-die-zukunft/

[50] T. Kirstein, “The learning bus”, ETH Zürich, Industry Relations, ETH News for Industry, October 4, 2017. [Online]. Available: https://www.industrynews.ethz.ch/index.php/2017/10/04/the-learning-bus/

[51] A. Eberhard, “Dank Forschung fahren Busse intelligent”, ETH Globe, March 9, 2018. [Online]. Available: https://ethz.ch/de/news-und-veranstaltungen/eth-news/news/2018/09/intelligenter-bus.html

[52] L. Serrao, S. Onori, G. Rizzoni, and Y. Guezennec, “A Novel Model-Based Algorithm for Battery Prognosis,” in *7th IFAC Symposium on Fault Detection, Supervision and Safety of Technical Processes*, 2009, pp. 923–928.

[53] L. Serrao, S. Onori, and A. S. P. o. the, “Optimal energy management of hybrid electric vehicles including battery aging,” *Proceedings of the American Control Conference*, pp. 2125–2130, Aug. 2011.

10 Appendices

Measured temperature profile in 2018 and 2019.

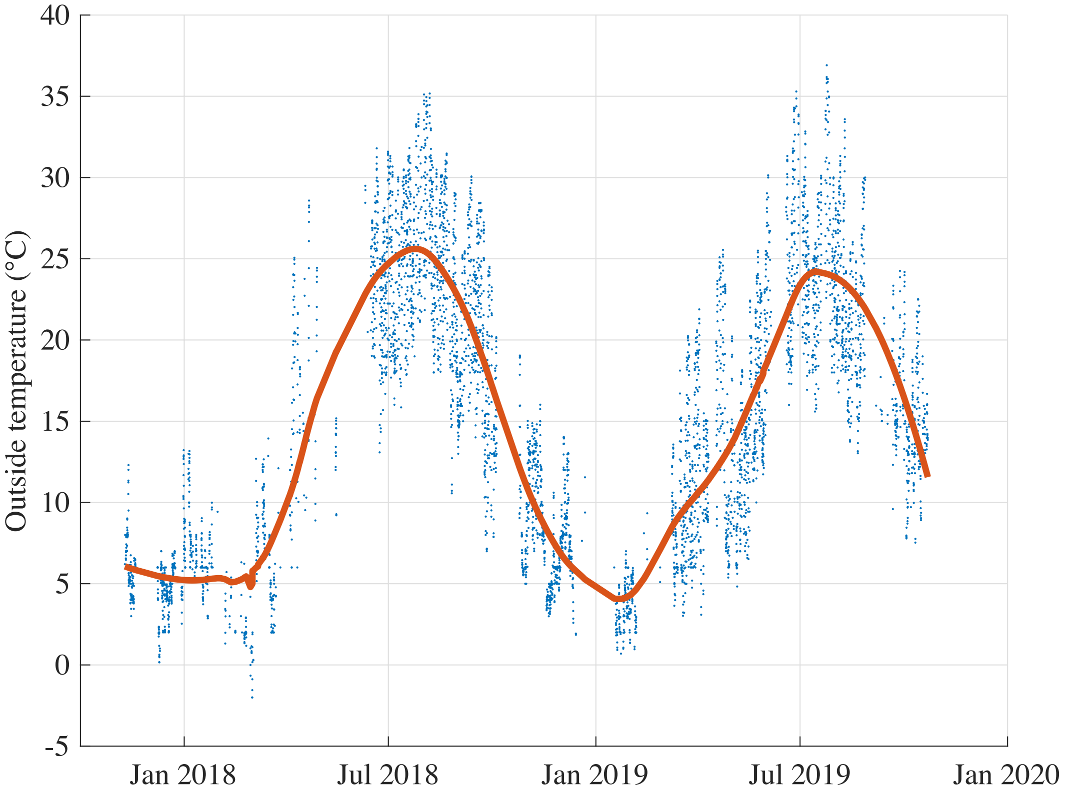

Figure 74. Temperature profile over two years

Test regime for tests with DoD < 100%

Start of experiments		**C/3**	T = 25 °C	25h		
	3x	C/3 Entladung +30min Warten				
		C/3 Ladung +30min Warten				
		2.5C				
	3x	2.5C Entladung +30min Warten				
		2.5C Ladung +30min Warten				
	1x	2.5C Entladung auf xx% SOC				
Aging cycles		**Cycling**		151h	2x Wiederholen (insgesamt 450 FEC)	Wiederholung
	150x FEC	2.5C Entladung auf xx% SOC				
		2.5C Ladung auf xx% SOC				
Diagnostic cycles I		**2.5C**		41h		
	2x	2.5C Entladung +30min Warten				
		2.5C Ladung +30min Warten				
		C/3				
	2x	C/3 Entladung +30min Warten				
		C/3 Ladung +30min Warten				
		Rdc 100%-80%-60%-50%-40%-20%				
		C/3				
	1x	C/3 Entladung +30min Warten				
		C/3 Ladung +30min Warten				
		2.5C				
	2x	2.5C Entladung +30min Warten				
		2.5C Ladung +30min Warten				
Diagnostic cycles II		**C/3**		120h		
	1x	C/3 Entladung +30min Warten				
		C/3 Ladung +30min Warten				
		100-50-0% EIS				
		EIS Pause				
	1x	C/3 50% Entladen + 30min Warten				
		EIS Pause				
	1x	C/3 50% Entladen + 30min Warten				
		EIS Pause				
		2.5C				
	2x	2.5C Entladung +30min Warten				
		2.5C Ladung +30min Warten				

Figure 75. Detailed schematic of the test regime for the cells tested at a DoD < 100%

Test regime for tests with DoD = 100%

Start of experiments		**C/3**	T = 25 °C	~63h		
	3x	C/3 Entladung +30min Warten				
		C/3 Ladung +30min Warten				
		Rdc 100%-80%-60%-50%-40%-20%				
		C/3				
	1x	C/3 Entladung +30min Warten				
		C/3 Ladung +30min Warten				
		100-50-0% EIS				
		EIS Pause (100%)				
	1x	C/3 50% Entladen + 30min Warten				
		EIS Pause (50%)				
	1x	C/3 50% Entladen + 30min Warten				
		EIS Pause (0%)				
		C/3				
	3x	C/3 Entladung +30min Warten				
		C/3 Ladung +30min Warten				
		2.5C				
	3x	2.5C Entladung +30min Warten				
		2.5C Ladung +30min Warten				
		xxC = 1, 2.5 or 5C				
	2x	xxC Entladung +30min Warten				
		xxC Ladung +30min Warten				
Aging cycles	150 x	**Cycling**	T = -5, 10, 25 or 45 °C	375h	2x Wiederholen (insgesamt 450 FEC)	Wiederholen
		xxC Entladung +30min Warten				
		xxC Ladung +30min Warten				
Diagnostic cycles I		**xxC = 1, 2.5 or 5C**		52h		
	3x	xxC Entladung +30min Warten				
		xxC Ladung +30min Warten				
		2.5C				
	3x	2.5C Entladung +30min Warten				
		2.5C Ladung +30min Warten				
		C/3				
	3x	C/3 Entladung +30min Warten				
		C/3 Ladung +30min Warten				
		Rdc 100%-80%-60%-50%-40%-20%				
		C/3				
	1x	C/3 Entladung +30min Warten				
		C/3 Ladung +30min Warten				
		xxC = 1, 2.5 or 5C				
	2x	xxC Entladung +30min Warten				
		xxC Ladung +30min Warten				
Diagnostic cycles II		**C/3**	T = 25 °C	216h		
	1x	C/3 Entladung +30min Warten				
		C/3 Ladung +30min Warten				
		Rdc 100%-80%-60%-50%-40%-20%				
		C/3				
	1x	C/3 Entladung +30min Warten				
		C/3 Ladung +30min Warten				
		100-50-0% EIS				
		EIS Pause				
	1x	C/3 50% Entladen + 30min Warten				
		EIS Pause				
	1x	C/3 50% Entladen + 30min Warten				
		EIS Pause				
		C/3				
	3x	C/3 Entladung +30min Warten				
		C/3 Ladung +30min Warten				
		2.5C				
	3x	2.5C Entladung +30min Warten				
		2.5C Ladung +30min Warten				
		xxC = 1, 2.5 or 5C				
	3x	xxC Entladung +30min Warten				
		xxC Ladung +30min Warten				

Figure 76. Detailed schematic of the test regime for the cells tested at a DoD = 100%

DC-resistance measurements for all cells

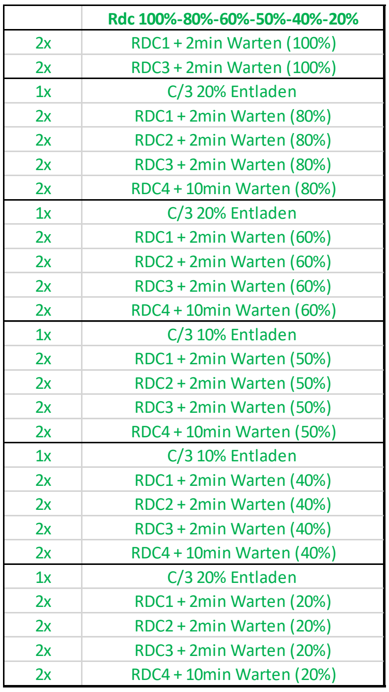

	Rdc 100%-80%-60%-50%-40%-20%
2x	RDC1 + 2min Warten (100%)
2x	RDC3 + 2min Warten (100%)
1x	C/3 20% Entladen
2x	RDC1 + 2min Warten (80%)
2x	RDC2 + 2min Warten (80%)
2x	RDC3 + 2min Warten (80%)
2x	RDC4 + 10min Warten (80%)
1x	C/3 20% Entladen
2x	RDC1 + 2min Warten (60%)
2x	RDC2 + 2min Warten (60%)
2x	RDC3 + 2min Warten (60%)
2x	RDC4 + 10min Warten (60%)
1x	C/3 10% Entladen
2x	RDC1 + 2min Warten (50%)
2x	RDC2 + 2min Warten (50%)
2x	RDC3 + 2min Warten (50%)
2x	RDC4 + 10min Warten (50%)
1x	C/3 10% Entladen
2x	RDC1 + 2min Warten (40%)
2x	RDC2 + 2min Warten (40%)
2x	RDC3 + 2min Warten (40%)
2x	RDC4 + 10min Warten (40%)
1x	C/3 20% Entladen
2x	RDC1 + 2min Warten (20%)
2x	RDC2 + 2min Warten (20%)
2x	RDC3 + 2min Warten (20%)
2x	RDC4 + 10min Warten (20%)

Figure 77. Detailed schematic of the test regime for the cells tested at a DoD = 100%